Ice nucleation activity of large particles and its dependence on mineralogical composition and size in the immersion freezing mode

Zur Erlangung des akademischen Grades eines
DOKTORS DER NATURWISSENSCHAFTEN
von der KIT-Fakultät für Physik des
Karlsruher Instituts für Technologie (KIT)

genehmigte

DISSERTATION

von

Sebastian Vergara Palacio
aus Medellin, Colombia

Tag der mündlichen Prüfung:	21.11.2025
Referentin:	TT-Prof. Dr. Martina Klose-Albinger
Korreferentin:	Prof. Dr. Corinna Hoose

Abstract

Mineral dust is one of the most abundant aerosol types in the atmosphere and an important climate constituent. Once lifted into the atmosphere, mineral dust particles can travel thousands of kilometers and persist for several days, with particle size distributions (PSD) extending up to hundreds of micrometers in diameter. During transport, mineral dust interacts with atmospheric components, among which clouds are particularly relevant due to their effects on the radiative balance, hydrological cycle, and energy budget. Of special importance are mixed-phase clouds (MPCs), in which liquid and solid phases coexist and which exert strong climatic influence through their global cover and long lifetime.

Mineral dust promotes the formation of ice particles in MPCs through ice nucleation, thereby altering cloud properties. Among the different mechanisms, immersion freezing is most relevant for MPCs. The efficiency of mineral dust as ice-nucleating particle in immersion freezing mode depends on particle properties such as surface characteristics, mineralogy, and size. While extensive research has characterized the ice nucleation activity (INA) of dust from low- and mid-latitude sources, high-latitude dust sources remain poorly studied. Furthermore, the role of particles larger than 10 µm and the influence of mineralogy on INA are still insufficiently understood.

This thesis addresses these gaps by investigating the INA of mineral dust in immersion freezing mode from both low- and high-latitude sources. Moroccan (low-latitude) and Icelandic (high-latitude) dust samples were systematically collected during field campaigns, characterized for their mineralogy, and size-separated in PSDs that span different size ranges and extend over three orders of magnitude (10^{-1} to 10^{2} µm). The INA was determined using the ice nucleation active site (INAS, n_s) density framework, in which nucleation occurs at specific surface sites and depends only on temperature. As part of the MICOS campaign and with the participation of multiple researchers, including the author, more than 300 ice-nucleation experiments were conducted in the AIDA cloud chamber, the AIDA mini-chamber (AIDAm), and the Ice Nucleation Spectrometer (INSEKT) at the Karlsruhe Institute of Technology (KIT). Parameterizations developed from these measurements were implemented in the ICON-ART atmospheric model and tested for the summer of 2021 for the northern hemisphere, using a global resolution of 20 km with a nested domain of 10 km over Iceland. A newly implemented source-tagging technique enabled the separation of Icelandic dust from global emissions.

Based on the laboratory data obtained in this study, the INAS density parameterizations developed for both sources showed an exponential dependence on temperature. Moroccan dust showed INAS density values comparable to feldspar. No size dependence was observed for Moroccan samples. In contrast, Icelandic samples displayed a size dependence. When comparing the developed Icelandic parameter-

ization to previous studies, the largest discrepancies occurred at warmer temperatures, particularly in INSEKT measurements. Overall, Icelandic dust was found to be less ice active than Moroccan dust. To better capture mineralogical and size effects, a new metric was introduced—the "effective surface area"—which modifies n_s based on the contribution of mineralogical fractions.

The results indicate that the commonly used assumption of size-independent $n_s(T)$ is not universally valid, particularly for polydisperse samples including particles larger than 10 µm. As is the case for smaller particles, larger particles can undergo long-range transport and substantially affect cloud microphysics. Given their size, they likely exhibit different mineralogical compositions than smaller particles. This highlights the need to explore the dependence of INA with mineralogical composition and size effects in future parameterizations. The ICON-ART simulations with the newly implemented source-tagging technique and parameterizations showed that Icelandic dust was located mainly within the planetary boundary layer and was deposited predominantly over Iceland and the adjacent ocean. Test cases considering the default parameterization in ICON and the newly developed parameterizations indicated that Icelandic dust made only a weak contribution (lower than 5%) to the total INP in immersion freezing mode. Despite small differences in MPC properties among the test cases, significant differences in the cloud radiative effects were found, with the new parameterizations improving the agreement with satellite observations. In conclusion, this work expands our understanding of mineral dust as an ice-nucleating particle by systematically contrasting high- and low-latitude sources and extending particle size distributions beyond the commonly studied micrometer range. The findings emphasize the importance of considering source variability, mineralogy, and particle size when characterizing INA and when representing dust–cloud interactions in climate models. This approach, combining field campaigns, laboratory experiments, and atmospheric modeling, provides new insights into the role of dust in immersion freezing mode and its broader climatic implications.

Preface

The doctoral candidate confirms that the research presented in this thesis includes significant original scientific contributions made by him. This thesis reuses material from the following publication:

Vergara-Palacio, S., Kiselev, A., Vogel, F., González-Romero, A., Fösig, R., Querol, X., Hoose, C., Silas Umo, N., Möhler, O., Kandler, K., Pérez García-Pando, C., & Klose, M. (2026). Ice nucleation activity of mineral dust from Morocco and Iceland in immersion freezing mode and its relationship with mineralogy and particle size. Atmospheric Chemistry and Physics, 26(12), 9113–9147. https://doi.org/10.5194/acp-26-9113-2026

The research leading to the results presented in Vergara-Palacio et al. (2026), as well as in this thesis, was carried out within the Helmholtz Young Investigator Group "A big unknown in the climate impact of atmospheric aerosol: Mineral soil dust" (grant no. VH-NG-1533).

The doctoral candidate led the research presented in Vergara-Palacio et al. (2026). Sample collection in Morocco and Iceland was carried out by co-authors of the study during field campaigns in Morocco and Iceland. The Morocco campaign was organised by the European Research Council project entitled FRontiers in dust minerAloGical coMposition and its Effects upoN climaTe (FRAGMENT, grant no. 773051) and the Iceland campaign co-organized between FRAGMENT and the German Research Foundation project Iceland as a model for high-latitude dust sources – a combined experimental and modeling approach for characterization of dust emission and transport processes (HiLDA, grant no. 417012665).

The ice-nucleation experiments were performed by the doctoral candidate and several project collaborators in the framework of the MICOS campaign, which is part of a project that is supported by the European Commission under the Horizon 2020 – Research and Innovation Framework Program, H2020-INFRAIA-2020-1, Grant Agreement number: 101008004.

The data post-processing, including the complete development of the algorithms for extraction, cleaning, validation, and model performance evaluation, was done by the doctoral candidate. The writing of Vergara-Palacio et al. (2026) was led by the doctoral candidate with input from co-authors. Similarly, all ICON-ART simulations, the associated data post-processing, algorithm development, and analysis of results were carried out by the doctoral candidate.

The candidate confirms that appropriate credit has been given within the thesis wherever reference has been made to the work of others. This copy has been supplied on the understanding that it is copyright material and that no quotation from the thesis may be published without proper acknowledgment.

ChatGPT and Claude were used as generative AI (GenAI) tools to assist with improving post-processing scripts and refining the stylistic quality of the thesis text.

Tennyson said that if we could understand a single flower we would know who we are and what the world is. Perhaps he meant that there is no deed, however so humble, which does not implicate universal history and the infinite concatenation of causes and effects.

—Jorge Luis Borges, *The Zahir*

Contents

Abstract i

Preface iii

Acronyms vii

List of Symbols ix

1 Introduction 1

2 Objectives 7

3 Theory 9

3.1 Mineral dust aerosol . . . 9

3.2 Cloud condensation nuclei . . . 12

3.3 Ice nucleation microphysics . . . 13

3.3.1 Classical nucleation theory . . . 14

3.3.2 Active Surface Site Approach . . . 19

3.4 Cloud Ice Microphysics . . . 22

4 Methods and Data 25

4.1 Laboratory ice nucleation experiments . . . 25

4.1.1 Collection and preparation of natural dust samples from Morocco and Iceland . . . 25

4.1.2 MICOS campaign . . . 27

4.1.3 Surface area estimation . . . 31

4.1.4 Dust aerosol particle size distributions in AIDA and AIDAm . . . 32

4.2 The ICON-ART Modeling Framework . . . 34

4.2.1 ICON . . . 34

4.2.2 ART . . . 35

4.2.3 Dust emission representation in ART . . . 36

4.2.4 Two-moment cloud microphysics parameterization for mixed-phase clouds 37

4.2.5 Nucleation of cloud ice . . . 39

4.2.6 Cloud radiative effect . . . 39
4.2.7 Phase partitioning and occurrence of mixed-phase clouds . . . 40
4.2.8 Modifications to ICON-ART . . . 41
4.2.9 Simulation setup . . . 44
4.3 Deriving Dust Optical Depth (DOD) from AERONET for model evaluation . . . 45

5 Results **51**
5.1 Results from Laboratory Experiments . . . 51
5.1.1 Influence of nonlinear terms on n_s . . . 51
5.1.2 Ice nucleation activity . . . 53
5.1.3 AIDAm . . . 57
5.2 Modeling results . . . 58
5.2.1 Model evaluation . . . 59
5.2.2 Characterization of atmospheric Icelandic dust . . . 62
5.2.3 Sensitivity study including newly developed INAS density parameterizations 63
5.2.4 Effect on mixed-phase cloud properties . . . 66
5.2.5 Cloud radiative effect . . . 68

6 Discussion **77**
6.1 Discussion of the experimental results . . . 77
6.1.1 Mineralogy of Moroccan samples . . . 77
6.1.2 Mineralogy of Icelandic samples . . . 78
6.1.3 Size dependence . . . 80
6.1.4 Effective surface area . . . 84
6.2 Discussion of the modeling results . . . 86

7 Summary **93**

8 Outlook **97**

9 Acknowledgments **99**

A ICON-ART Modifications for Dust Source Tagging **101**

B Additional Modifications to ART Subroutines for New Tracers **109**

C J-WADI field campaign **111**

Acronyms

AR Aspect ratio

ARE Absolute relative error

ART Aerosols and Reactive Trace gases extension

CCN Cloud condensation nuclei

CERES Clouds Earth's Radiant Energy System

CN Condensation nuclei

CNT Classical nucleation theory

CRE Cloud radiative effect

ECS Equilibrium climate sensitivity

HLD High-latitude dust

HWR Height-to-width ratio

ICON The ICOsahedral Nonhydrostatic model

INA Ice nucleation activity

INAS Ice nucleation active site

INPs Ice nucleating particles

LLD Low-latitude dust

LW Longwave radiation

MLD Mid-latitude dust

MPCs Mixed-phase clouds

PSDs Particle size distributions

SW Shortwave radiation

TOA Top-of-atmosphere

List of Symbols

A_p Projected area of the particle

D_V Volume-equivalent diameter

D_a Aerodynamic-equivalent diameter

$D_{\mathbf{PA}}$ Projected area-equivalent diameter

$D_{\mathbf{opt}}$ Optical-equivalent diameter

D_{crit} Critical diameter at supersaturation s

D dry mineral dust diameter

J Homogeneous freezing steady-state rate of nucleation

K_B Boltzmann constant

K_h Turbulent diffusivity of heat

M_c^0 Partial moment number concentration for cloud droplets

M_c^1 Partial moment mass concentration for cloud droplets

M_r^0 Partial moment number concentration for rain drops

M_r^1 Partial moment mass concentration for rain drops

N_0 Initial number of unfrozen droplets

N Total number of particles per volume

R_c Critical radius of the cluster

$S_{\mathbf{area}}$ Surface area of the particle

S Total surface area of particles per volume of air

V_p Particle volume

V Total aerosol volume per volume of air

ΔF_{diff} Difussion activation energy of a water molecule to cross the water/ice embryo interface

ΔG Free energy change

$\Delta \mu$ Difference in the chemical potential between molecules in the initial and new phase

$\bar{D}_{pg}$ Median diameter of lognormal distribution

χ Dynamic shape factor

ρ_0 Water density

ρ_p Particle density

σ_p Geometric standard deviation of lognormal distribution

σ_{xy} Interfacial tensions between the different phases

σ Interfacial free energy

τ_{inact} Relaxation time

f_s Fraction of particles of specific diameter that are activated at supersaturation s

h Planck's constant

$k(T)$ Differential nucleus concentration of active sites per surface area and temperature

n_N Number of particles per diameter per volume

$n_s(T)$ Cumulative nucleus concentration, also called ice nucleation active site (INAS) density

n_s Aerosol surface area distribution

n_v Aerosol volume distribution

n_{dep} INP number concentration due to deposition nucleation

n_{imm} INP number concentration due to immersion freezing

n_{inact} Number of activated INP

n Number density of water molecules at the ice nucleus/water interface

s Supersaturation with respect to water

u_{*t} Friction velocity threshold

x_c Mean cloud droplet mass

1. Introduction

Dust is found to be one of the most abundant aerosol types in terms of mass in the atmosphere and a key atmospheric constituent given its climate effects (Pan et al., 2023; Kim et al., 2024; Wang et al., 2024). The impacts of dust include changing the Earth radiation budget (Ackerman and Chung, 1992; Ashrafi et al., 2017; Tian et al., 2021; Kok et al., 2023), interacting with clouds and changing their properties, e.g. precipitation, light absorption and scattering, lifetime (Yin et al., 2002; Atkinson et al., 2013; Jones et al., 2022; Li et al., 2022), damaging human health such as chronic lung disease, and fibrosis (Derbyshire, 2007; Georgakopoulou et al., 2024), impacting social activities, for example, reducing visibility and affecting traffic (Idso, 1976; Zhao et al., 2022; Middleton and Al-Hemoud, 2024), in economic activities as in the energy sector reducing the efficiency of solar photovoltaic systems (Mejia et al., 2014; Prasad et al., 2022), and fertilizing maritime and continental ecosystems (Meskhidze et al., 2005; Koren et al., 2006; Bristow et al., 2010; Swart et al., 2014).

The average global dust emission flux and atmospheric dust load for dust-particle diameters up to 20 μm were estimated to be in the range of about 2700 - 5200 Tg yr^{-1} and 28 - 35 Tg, respectively (Klose et al., 2021). Once the particles are lifted into the troposphere, they can travel for thousands of kilometers and have lifespans of several days. The last years of atmospheric mineral dust research have changed a believed fact in which large mineral dust particles do not travel far from their source. For instance, some recent studies have found dust particle sizes in the atmosphere ranging from 0.1 μm up to 450 μm thousands of kilometers far away from their sources (Mahowald et al., 2014; Van Der Does et al., 2018; Ryder et al., 2018). Therefore, it is clear that the current understanding and calculations of dust deposition are failing.

A size classification for mineral dust particles, based on their diameter D, is introduced in Sect. 3.1.

The question of how dust is able to travel long distances remains open. Although little is known about the underlying mechanisms, some explanations have been suggested, such as strong turbulence enhancing vertical mixing (Denjean et al., 2016) and triboelectrification (Van Der Does et al., 2018). Further research is therefore needed.

As dust travels, it interacts with different atmospheric constituents. Among these, the interaction with water vapor is particularly important for dust's radiative and climatic effects, as it allows dust to influence cloud formation and properties. Clouds affect the radiative balance of the Earth. For instance, low, thick clouds (such as stratus and stratocumulus) reflect a fraction of the incoming solar radiation leading to cooling of Earth's surface. On the other hand, clouds also absorb outgoing long-wave radiation from the Earth's surface and atmosphere, re-emitting it partly downward creating a greenhouse-like warming

effect. The net radiative effect, either warming or cooling, depends on the cloud phase and microphysical properties (e.g., whether the cloud consists of liquid droplets, ice crystals, or a mixture, as well as particle size and concentration) (Taylor, 2012). Furthermore, clouds play a central role in both the hydrological and energy cycles. In the hydrological cycle, water evaporates from the surface, condenses in the atmosphere, and forms rain, snow, and other hydrometeors, which after a series of processes return to the surface. In the energy cycle, clouds regulate the transfer of energy through the release of latent heat during phase changes and through the absorption, reflection, and emission of radiation (Taylor, 2012). Additionally, clouds carry heat, moisture, and momentum from the surface to upper levels, influencing large-scale atmospheric circulation (Larson et al., 1999; Fajber et al., 2023). Observational constraints suggest that cloud responses to warming tend to amplify global temperature rise, with a positive feedback roughly $+0.43 \pm 0.35$ W/m^2/K (Ceppi and Nowack, 2021). All of these effects depend on cloud properties such as phase, distribution, altitude, and thickness. According to these properties, clouds can be categorized into warm clouds: all liquid droplets above 0°C (e.g., stratus, cumulus), ice clouds: composed of ice crystals, generally for temperatures below -38°C (e.g., cirrus), and mixed-phase clouds (MPCs) where super cooled liquid and ice coexist for temperatures between -38°C and 0°C. MPCs are of special interest in climate research as they cover $\approx$ 34% of the Earth's surface, especially in mid- to high latitudes where they are the dominant cloud type and exert a strong influence on both the surface energy budget and precipitation processes (Shi and Liu, 2019). Additionally, MPCs persist longer than pure ice or warm clouds due to the balance between ice growth and liquid supply (Wegener–Bergeron–Findeisen process; discussed in more depth in Sect. 3.4), suppressing rain and affecting albedo (Coopman and Tan, 2023). Therefore, given its broad global cover and prolonged lifetime, MPCs dominate the cloud-phase feedback, a major source of uncertainty in the equilibrium climate sensitivity (ECS) (Tan et al., 2016; Hofer et al., 2024). Constraining their behavior and hence ruling out unrealistically strong negative cloud-phase feedbacks (i.e., with warming, MPCs become more liquid-dominated, which increases their shortwave reflectance) can increase ECS by up to 1.3°C, shifting models from $\approx$4°C to $\approx$5°C in response to doubled CO_2 (Tan et al., 2016).

Mineral dust interacts with and modifies clouds through cloud condensation nucleation and ice nucleation. Mineral dust is one of the most relevant particle types in the primary formation of ice crystals in MPCs and influences cloud phase, liquid and ice water path, radiative forcing, and cloud lifetime (Atkinson et al., 2013). The extent and nature of these modifications depend on the effectiveness of mineral dust in promoting cloud condensation and ice nucleation. Cloud condensation nucleation occurs under supersaturation conditions (relative humidity higher than 100%) where dust aerosols promote the activation of water vapor into cloud droplets. The efficiency to act as a cloud condensation nucleus (CCN) at a given supersaturation is determined by the particle diameter, chemical composition, and mixing state (Bhattu and Tripathi, 2015; Ren et al., 2018). Different theories have been developed to describe water adsorption under both sub- and supersaturated conditions, most of them are based on thermodynamic principles and rely on parameters such as contact angle (θ) between mineral dust surface and water

molecules, pressure (expressed through relative humidity), and empirical constants (see Section 3.3.1). On the other hand, pure water droplets can exist in a clean atmosphere well below 0°C (Hoose and Möhler, 2012), and they will eventually freeze if the temperature decreases sufficiently. Under supersaturated conditions, this typically occurs at temperatures below -38°C, through a process known as homogeneous freezing (Pruppacher et al., 1998). Conversely, ice crystals form at warmer temperatures if water or water vapor molecules come into contact with particles that can nucleate ice. This phenomenon is called heterogeneous freezing and the particles that interact with water molecules are known as ice nucleating particles (INPs). There are several mechanisms by which particles can act as INP, these are (Hoose and Möhler, 2012; Murray et al., 2012): deposition nucleation, condensation freezing, immersion freezing, and contact freezing. Each mechanism is characterized by a temperature and supersaturation range (see Section 3.3). In order to describe mathematically the liquid water phase or water vapor phase change to ice in both homogeneous and heterogeneous freezing, the so-called classical nucleation theory (CNT) is used. This theory is based on thermodynamic and energetic principles and although it has several assumptions, it has proven to be able to explain general trends for some particles under specific conditions. However, CNT has several drawbacks and is unable to accurately predict heterogeneous freezing for most cases. As a consequence, to better predict heterogeneous freezing, parameterizations are used. In a broad sense, INP parameterizations can be divided into empirical and CNT-based parameterizations. Although parameterizations developed for particles from similar sources and under comparable temperatures and supersaturations generally agree within a certain range (Atkinson et al., 2013; Harrison et al., 2022), significant uncertainty remains regarding the factors that cause the spread in predicted values. One drawback of CNT-based parameterizations is that they have not been shown to be applicable across the entire temperature range (Ullrich et al., 2017). On the other hand, empirical parameterizations are based on laboratory and field observations, but they often neglect the influence of aerosol composition on ice nucleation activity because it is difficult to measure. In addition to that, empirical parameterizations are not able to cover the whole atmospherically relevant temperature and humidity range (Ullrich et al., 2017), they do not explicitly represent physical processes and are not easy to modify to include additional conditions or parameters from which they were obtained. For instance, curvature effect, contact angle of water droplets with particle surface, surface properties (cracks, surface area), and particle composition have an effect on the nucleation rate, which are neglected or simplified in most parameterizations. Therefore, parameterizations derived for one size range may not represent ice nucleation in another size range if relevant properties differ (Chen et al., 2008). However, most of the ice nucleation studies focused their attention on developing parameterizations for particle size distributions (PSDs) with maximum diameter of a few µm ($\lesssim$ 10 µm) because these PSDs were considered to be the most relevant in atmospheric processes (Murray et al., 2011; Atkinson et al., 2013; Ullrich et al., 2017; Schiebel, 2017; Harrison et al., 2022).

It is also important to mention that a substantial and extensive literature is available for mineral dust INP efficiency from mid-latitude dust (MLD) and low-latitude dust (LLD) sources (Phillips et al., 2008; Nie-

mand et al., 2012; Atkinson et al., 2013; DeMott et al., 2015; Ullrich et al., 2017; Harrison et al., 2022; Gao et al., 2024). Following Ginoux et al. (2012), Bullard et al. (2016), and Barr et al. (2023), LLD sources are located in tropical and sub-tropical regions and are dominated by deserts, mostly between 0° and 35° N (e.g. the Sahara and Arabian deserts); MLD sources are located in temperate regions and can be linked to steppe areas (e.g. Central and East Asia); and high-latitude dust (HLD) sources are located in polar and cold-desert regions, primarily from glacier outwash and volcanic activity, and are defined as those poleward of 50° N and 40° S (Bullard et al., 2016). However, less is known about the INP efficiency from HLD sources. MLD and LLD sources are the major contributors to the global dust total emission, with $\approx 52\%$ from North Africa and $\approx 38\%$ from Asia, HLD sources only contribute to $\approx 2-5\%$ (above 50° N) (Bullard et al., 2016; Shi et al., 2022). Hence, the relevance of MLD and LLD as INP can be expected to be larger in global context. However, studies have shown that HLD is relevant in the regional context. For instance, Groot Zwaaftink et al. (2016) showed that HLD contributes 27% of the total dust burden in the Arctic. Specifically, Iceland is a relevant HLD source contributing between $3-25\%$ to the total HLD burden (Arnalds et al., 2014; Bullard et al., 2016; Groot Zwaaftink et al., 2017). However, little is known about Icelandic dust efficiency as INP and its effects on MPCs. A few studies have focused their attention on this relevant source, and have developed parameterizations that account for Icelandic dust as INP (Steinke et al., 2011; Paramonov et al., 2018; Sanchez-Marroquin et al., 2020). Nonetheless, they have limited the PSDs to maximum diameters of only a few micrometers. Furthermore, few studies have considered HLD as emission sources in numerical models that explicitly track aerosol dust emitted from these sources, and their contribution to INP and effects (Shi et al., 2022). An important complementary dimension is the mineralogical heterogeneity of dust sources: dust from different regions or parent soils can differ in clay content, feldspar content (especially potassium-feldspar), quartz, iron oxides, and coating of secondary minerals and organics. These compositional differences influence ice nucleation activity, because minerals such as K-feldspar are especially active as ice-nucleating substrates under mixed-phase conditions (Atkinson et al., 2013; Hoose and Möhler, 2012; Burrows et al., 2022). For example, mineral dust containing higher fractions of K-feldspar can nucleate ice at warmer temperatures (e.g. > -15 °C), whereas dust dominated by quartz or less active minerals tends to require colder conditions (Burrows et al., 2022; Kawai and Matsui, 2025).

To conclude, substantial progress has been made in characterizing mineral dust as an INP, yet significant uncertainties persist in how dust–cloud interactions are represented and quantified. Furthermore, gaps remain, such as the inclusion of broader PSDs in experimental testing, the mineralogical characterization of the samples being tested, and the inclusion of HLD sources in both parameterizations and modeling studies, and their effects on clouds and climate.

Motivated by the relevance of these unsolved questions, this thesis aims to study mineral dust as INP in immersion freezing mode from LLD (Morocco) and HLD (Iceland) sources, covering nearly three orders of magnitude in particle size (from 10^{-1} µm to 10^{2} µm), with mineralogical characterization resolved by particle size. Furthermore, our results are implemented in the state-of-the-art numerical

model ICON-ART to study their effects on MPCs, using explicit emission and tracking of Icelandic dust sources. For this, a multi-method approach is taken, combining a field campaign to collect samples, sample preparation for experiments, laboratory ice-nucleation experiments in the immersion-freezing mode using multiple techniques, theory to derive new parameterizations, and modeling to test newly developed source-specific dust ice nucleation activity parameterizations, assessing their impact on MPCs relative to default schemes (Fig. 1.1).

This thesis is structured as follows: objectives are presented in Chapter 2; Chapter 3 introduces the theoretical background on mineral dust aerosols, ice nucleation, and cloud microphysics relevant to this thesis; Chapter 4 describes the numerical model, how key processes are represented, and the modifications made to the model, and it also details sample collection and the instruments and setups used to prepare and perform ice-nucleation experiments. Chapter 5 presents results from immersion-freezing experiments, develops new parameterizations, evaluates tests of these parameterizations against the default case implemented in ICON-ART. Chapter 6 discusses the implications of the experimental results, including their dependence on particle size and mineralogical composition, and the comparison of the different test simulations. Finally, Chapter 7 summarizes the work, and Chapter 8 outlines future perspectives.

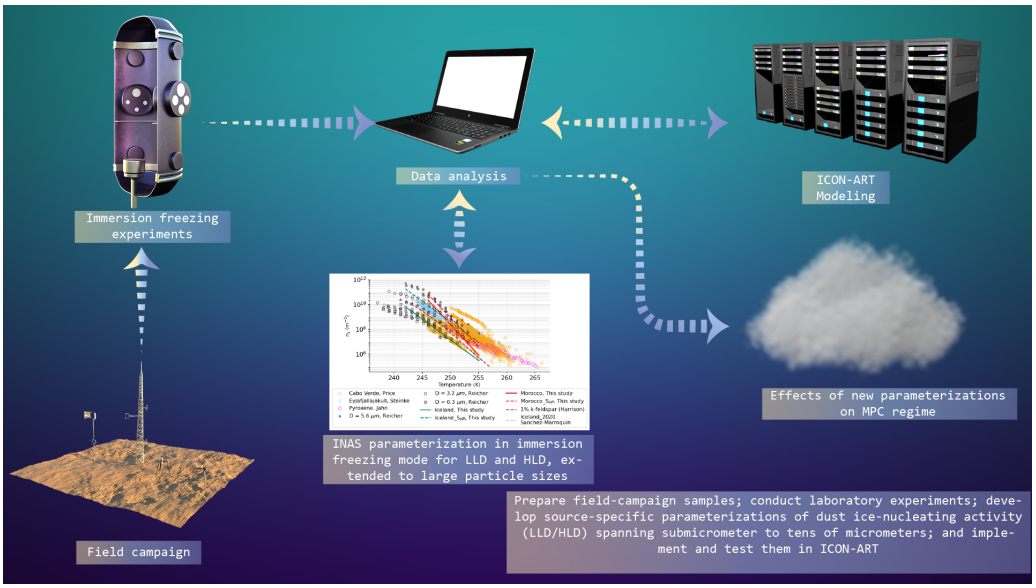


Figure 1.1.: Illustration of the approach used in this thesis: a field campaign provides samples for immersion-freezing experiments; the resulting data are analyzed to derive new source-specific INAS parameterizations, which are then implemented in ICON-ART modeling to assess their effects on mixed-phase clouds. I thank Julian Vergara Palacio for contributing to the creation of the illustration.

2. Objectives

The goal of this research is twofold: first, to quantitatively evaluate the ice-nucleating activity of mineral dust in immersion freezing mode, including particle sizes ranging from the submicrometer scale to several tens of micrometers, from both low- and high-latitude sources; and second, to assess the differences in the impact of low- and high-latitude dust acting as ice-nucleating particles on cloud properties.
In order to achieve these goals, the following objectives will be addressed.

1. Prepare dust samples from previous campaigns for laboratory experiments.

2. Conduct laboratory experiments to relate mineral dust characteristics (size and mineralogical composition) to their ice-nucleating activity.

3. Assess the effects of large particles on ice-nucleating activity in immersion freezing mode with data obtained from the laboratory experiments, and develop new parameterizations that cover the submicrometer scale to several tens of micrometers.

4. Implement the revised parameterizations in ICON-ART, test their performance, and evaluate how source-specific parameterizations for low- and high-latitude dust influence cloud properties, with emphasis on high latitudes.

3. Theory

This chapter provides the theoretical background on which the subsequent analyses are built. Section 3.1 introduces the definition and size classification of mineral dust aerosols and describes their particle-size distributions (PSDs). Section 3.2 reviews cloud-droplet activation, outlining the conditions under which mineral dust can act as cloud-condensation nuclei (CCN). Section 3.3 summarizes homogeneous and heterogeneous ice nucleation with a focus on immersion freezing, introducing common approaches such as the classical nucleation theory (CNT) and the ice nucleation active-site (INAS, $n_s(T)$) density. Finally, Section 3.4 outlines the key mixed-phase cloud microphysical processes (e.g., diffusional growth, aggregation, the Wegener–Bergeron–Findeisen process, riming) that govern phase transitions among vapor, liquid, and ice and lead to distinct hydrometeor categories. Together, these sections establish the physical and mathematical basis used later to interpret experimental results and model simulations.

3.1. Mineral dust aerosol

Mineral dust aerosols are solid particles of mineral origin that are emitted from arid and semi-arid surfaces and subsequently transported in the atmosphere. They consist primarily of inorganic minerals derived from soil, with possible contributions from other natural and anthropogenic materials (Knippertz and Stuut, 2014). Dust particles can be defined according to their diameter into fine mode ($D < 2.5$ µm), coarse mode ($2.5 \leq D < 10$ µm), super-coarse mode ($10 \leq D < 62.5$ µm), and giant mode (62.5 µm $\leq D$) (Adebiyi et al., 2023). However, dust particles have irregular shapes (Huang et al., 2020) and several different definitions of effective/equivalent diameter are used based on a physical property. The most commonly used effective diameters are:

- volume-equivalent diameter: diameter of a sphere that has the same volume as an irregularly shaped dust particle.
- aerodynamic diameter: diameter of a sphere with the same density as water and with the same terminal velocity as an irregularly shaped dust particle.
- optical diameter: diameter of a calibration particle, generally a polystyrene latex sphere, that produces the same scattered light intensity as the dust particle.
- projected area-equivalent diameter: diameter of a circle having the same area as the dust particle projected on a two-dimensional image.

Table 3.1.: Summary of aerosol effective/equivalent diameters using different particle properties. V_p is particle volume, D_V is the volume-equivalent diameter, ρ_p is the particle density, ρ_0=1000 kg m^{-3} is the reference density, χ is the dynamic shape factor, a dimensionless parameter that quantifies the increased drag on a non-spherical particle relative to a volume-equivalent sphere, and A_p is the projected area of the particle.

Name	**Symbol**	**Formula**	**Depends on**	**Reference**
Volume-equivalent	D_V	$\left(\frac{6V_p}{\pi}\right)^{1/3}$	Particle volume	Hinds and Zhu (2022)
Aerodynamic	D_a	$D_V\sqrt{\frac{\rho_p\chi}{\rho_0}}$	Density, shape	Kulkarni et al. (2011)
Optical	D_{opt}	Mie or T-matrix inversion to match scattering cross section	Refractive index, wavelength, shape	Bohren and Huffman (2008)
Projected area-equivalent	D_{PA}	$\sqrt{\frac{4A_p}{\pi}}$	Projected area	Okada et al. (2001)

Table 3.1 summarizes the different effective diameters.

We define the total number of particles integrated over the full size range as

$$N = \int_0^\infty n_N(D_P)dD_p \tag{3.1}$$

Where N is the total number of particles per volume (m^{-3}), $n_N(D_p)$ is the number of particles per diameter per volume (units of m^{-1} m^{-3}), D_p is the diameter of the particle, and dD_p is the differential in diameter. Analogous to the definition in Eq. 3.1, and assuming a spherical shape for the particles, the total surface area of particles per volume of air, S (m^2 m^{-3}), can be computed and linked to the number concentration as

$$S = \int_0^\infty n_s(D_p)dD_p = \pi\int_0^\infty D_p^2 n_N(D_p)dD_p \tag{3.2}$$

with $n_s(D_p)$ denoting the aerosol surface area distribution. In a similar way, the total aerosol volume per volume of air, V (m^3 m^{-3}), is defined as

$$V = \int_0^\infty n_v(D_p)dD_p = \frac{\pi}{6}\int_0^\infty D_p^3 n_N(D_p)dD_p \tag{3.3}$$

with $n_v(D_p)$ denoting the aerosol volume distribution.

The calculation of Eqs. 3.1, 3.2, and 3.3 requires knowledge of the particle number size distribution ($n_N(D_p)$). In modeling applications, a semi-empirical function is often chosen to represent n_N. Among the various mathematical functions, the lognormal distribution is commonly used as it provides a good fit with observational data (Mahowald et al., 2014; Meng et al., 2022; Zhu and Wang, 2024), although n_N need not necessarily take this form. Equation 3.4 presents the lognormal distribution for the particle number concentration where N is the total number of particles per volume of air, $\bar{D}_{pg}$ is the median diameter (diameter for which exactly one-half of the particles are smaller and one-half are larger), σ_p is the geometric standard deviation (84.1% of the particles are smaller than the product $\bar{D}_{pg}\sigma_p$).

$$n_N(D_p) = \frac{dN}{dD_p} = \frac{N}{(2\pi)^{1/2} D_p ln\sigma_p} exp(-\frac{(lnD_p - ln\bar{D}_{pg})^2}{2ln^2\sigma_p}) \tag{3.4}$$

The lognormal particle-number distribution has several relevant properties. Some of them are:

- If $n_N(D_p)$ is lognormal, the surface area distribution $n_s(D_p)$ is also lognormal with the same geometric standard deviation σ_p and with the surface median diameter given by

$$ln\bar{D}_{pgS} = ln\bar{D}_{pg} + 2ln^2\sigma_p \tag{3.5}$$

- If $n_N(D_p)$ is lognormal, the volume distribution $n_v(D_p)$ is also lognormal with the same standard deviation σ_p and with volume median diameter given by

$$ln\bar{D}_{pgV} = ln\bar{D}_{pg} + 3ln^2\sigma_p \tag{3.6}$$

For a complete derivation and discussion of the lognormal distribution, as well as its application to number, surface area, and volume concentrations, see Seinfeld and Pandis (2016).
Measurements show that dust aerosols deviate from spherical shapes and that ellipsoids are more realistic approximations of dust aerosol shape (Huang et al., 2021). In this context, the relevant distinction is the number of independent axes used to describe the particle: a spheroid is a special case of an ellipsoid with only two independent axes (one axis of revolution and one equatorial radius), whereas a general ellipsoid has three independent axes. Two main descriptors can be used to quantify dust asphericity, these are the aspect ratio (AR: ratio of particle's length to its width) and the height-to-width ratio (HWR). Studies have shown that if the particle width is taken as the minor axis of an ellipse that has the same area as the projected area of the particle and has the length as its major axis, then the AR follows a modified lognormal density distribution (Eq 3.7), while the HWR follows a lognormal density distribution (Eq 3.8) (Huang et al., 2020):

$$f(\mathrm{AR}) = \frac{1}{\sqrt{2\pi}\cdot(\mathrm{AR}-1)\cdot\sigma_a} \exp\left[-\frac{1}{2}\left(\frac{\ln(\mathrm{AR}-1)-\ln(\bar{\varepsilon}_a-1)}{\sigma_a}\right)^2\right], \tag{3.7}$$

Where σ_a is the geometric standard deviation of AR-1 and $\bar{\varepsilon}_a$ is the median of AR.

$$f(\mathrm{HWR}) = \frac{1}{\sqrt{2\pi}\cdot\mathrm{HWR}\cdot\sigma_h} \exp\left[-\frac{1}{2}\left(\frac{\ln(\mathrm{HWR})-\ln(\bar{\varepsilon}_h)}{\sigma_h}\right)^2\right], \tag{3.8}$$

Where σ_h is the geometric standard deviation of HWR and $\bar{\varepsilon}_h$ is the median of HWR.

3.2. Cloud condensation nuclei

The formation of water droplets in particle-free air requires a supersaturation of several hundred percent, which is difficult to achieve under atmospheric conditions. This highlights the essential role of aerosol particles in cloud formation by reducing the required supersaturation. The ability of a particle to serve as a nucleus for droplet formation depends on its size, chemical composition, and the local supersaturation. Particles that can act as nuclei for cloud droplet formation at a given supersaturation are known as cloud condensation nuclei (CCN). Conversely, condensation nuclei (CN) are typically defined as particles capable of forming droplets at supersaturations of $\geq 400\%$ and therefore CN includes all available particles (Seinfeld and Pandis, 2016). Therefore, it is reasonable to assume that the CN concentration is equal to the total aerosol number concentration. It is important to emphasize that the CCN concentration always refers to a specific supersaturation, for example CCN(1%) is the CCN concentration at 1% supersaturation with respect to water.

In the framework of Köhler theory (Köhler, 1936), a dry particle of radius r_d takes up water and becomes a solution droplet of wet radius r. Thermodynamic balance with the surrounding water vapour is achieved at the equilibrium saturation ratio $S_{eq}(r)$, given by (Petters and Kreidenweis, 2007)

$$S_{eq} = a_w(r) \exp(\frac{A}{r}) \tag{3.9}$$

where $a_w(r)$ is the activity of water in the solution and $A = \frac{2\sigma M_w}{\rho_w RT}$, with σ the surface tension of the solution–air interface, M_w the molecular weight of water, ρ_w the density of water, R the universal gas constant, and T the temperature.

Equation (3.9) expresses two competing effects. The factor $a_w(r)$ is related to the Raoult (solute) effect: dissolved solute lowers the equilibrium vapor pressure and favors growth. The exponential factor $\exp(\frac{A}{r})$ embodies the Kelvin (curvature) effect: strong curvature at small r raises the equilibrium vapor pressure and inhibits growth. Consequently, for otherwise identical composition, larger particles (larger r_d) tend to activate more easily because the curvature penalty is smaller.

Additionally, Eq. 3.9 exhibits a maximum (the Köhler maximum). The corresponding critical saturation ratio S_{crit} and critical radius r_{crit} are defined by this maximum (the corresponding critical diameter is $D_{crit} = 2r_{crit}$). If the ambient saturation ratio S exceeds S_{crit}, the droplet grows past r_{crit} and undergoes sustained condensational growth (activation). Since S_{crit} decreases with increasing dry size r_d (for fixed composition), larger particles require lower supersaturation (defined as $s = S - 1$) to activate and form cloud droplets.

In the case of an aerosol population that has uniform size-independent composition, the CCN concentration at a given supersaturation s is given by:

$$CCN(s) = \int_{D_{crit}}^{\infty} n_N(D_p) dD_p \tag{3.10}$$

where D_{crit} is the critical diameter at supersaturation s (physically, D_{crit} represents the aerosol diameter threshold above which particles activate into cloud droplets, while those smaller than D_{crit} remain unactivated), and $n_N(D_p)$ is the aerosol number size distribution, here represented by its common lognormal parameterization (Eq. 3.4), although $n_N(D_p)$ is not necessarily lognormal in general. For the case of aerosol populations in which the chemical composition is size-dependent, the CCN function takes the form

$$CCN(s) = \int_0^\infty f_s(D_p) n_N(D_p) dD_p \tag{3.11}$$

where $f_s(D_p)$ is the fraction of particles of diameter D_p that are activated at supersaturation s.
Given the difficulty of determining the aerosol size–composition distribution, a number of empirical parameterizations have been proposed based on atmospheric measurements. Among them, one of the most widely used is the Twomey power-law relation (Eq. 3.12), particularly suitable for polluted continental aerosols but less representative for marine or dust-dominated environments.

$$CCN(s) = cs^k \tag{3.12}$$

where CCN is in number of particles cm^{-3}, s is the supersaturation with respect to water expressed as percentage, c is a constant that corresponds to CCN(1%), and k is an empirical parameter. For most of the cases, in which ambient supersaturation does not exceed 1%, CCN concentrations are typically 100 to 1000 cm^{-3} over continents and from 10 to 200 cm^{-3} over oceans (Seinfeld and Pandis, 2016).

3.3. Ice nucleation microphysics

The phase transition from water vapor or liquid water to ice in the atmosphere can occur by different mechanisms. The main two categories are homogeneous ice nucleation and heterogeneous ice nucleation. In homogeneous ice nucleation, supercooled liquid droplets in an aerosol-free atmosphere can persist well below 0°C (273.15 K), remaining in the liquid state until temperatures reach approximately −38°C (235.15 K) where water droplets will freeze. In the presence of aerosols, heterogeneous ice nucleation takes place, in which aerosols initiate the phase transition to ice at warmer temperatures than in homogeneous ice nucleation, acting as seeds for the ice crystal formation and termed as ice nucleating particle (INP).
The main pathways for heterogenous ice nucleation are (Hoose and Möhler, 2012) (Fig 3.1):

- deposition nucleation: It occurs below water saturation in which supersaturated water vapor directly deposits on the INP surface changing its state from vapor to ice.

- immersion freezing: Supercooled water droplets form around the particle in a supersaturated water environment and upon further cooling they nucleate to ice.

- contact freezing: supercooled water droplets above water saturation collide with an aerosol particle triggering ice nucleation.

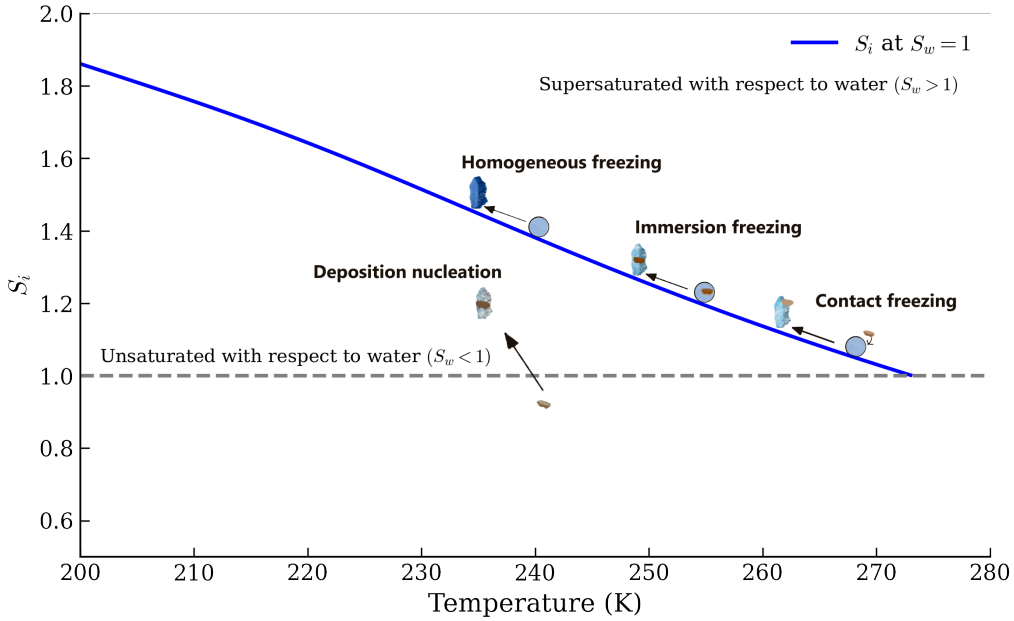


Figure 3.1.: Supersaturation with respect to ice (S_i) as a function of temperature. Solid blue line shows S_i for the case of water saturation ($S_w = 1$), above blue line supersaturated environment, below blue line unsaturated environment. Additionally, the deposition nucleation, immersion freezing, contact freezing, and homogeneous freezing nucleation modes are shown. Blue sphere: water droplet, brown shape: aerosol particle, and blue elongated shape: water droplet nucleated to ice.

In addition to the pathways mentioned above, there is one additional pathway named condensation freezing. Condensation freezing is the pathway where water vapor first condenses as a liquid film or droplet on the surface of a particle, and then this freshly condensed liquid freezes almost immediately. However, condensation freezing and immersion freezing are mechanistically similar and often indistinguishable in atmospheric conditions or laboratory experiments (Kanji et al., 2017). For the purposes of the following discussion, immersion freezing and condensation freezing are grouped together and treated as a single process, as is commonly done in experimental studies. Nevertheless, some studies distinguish between the two and define them as separate mechanisms (Hoose and Möhler, 2012).

3.3.1. Classical nucleation theory

In this section, the formation of a cluster of the new phase of ice or water and its subsequent growth using the classical nucleation theory (CNT) is discussed. Before that, it is important to mention the main assumptions used and the limitations of the theory. The major assumption in CNT is the consideration that clusters of a small number of molecules exhibit the same surface tension as the bulk liquid (capillarity approximation) (Beneduce et al., 2025). Additionally, it is assumed that parameters such as interfacial energy, density, and saturation ratios are independent of size. Another relevant assumption is

regarding the surface of an aerosol particle as uniform and that the whole surface and its interaction with different clusters can be described by one single contact angle (Zeng and Xu, 2015). In reality, aerosol surfaces are highly variable and they present different contact angles (Niedermeier et al., 2011). Contact angle and surface tension are difficult parameters to determine, and CNT uses many bulk thermodynamic properties to describe the behavior of microscopic nucleation. For instance, the contact angle is a macroscopic concept that might not hold for the initial germ, and there is a marked difference between the macroscopic angle and that of the ice germ due to the line tension effect (Evans and Lane, 1973). Another concern arises from the basic assumption of the CNT where the germ formation over a particle is assumed to follow a Boltzmann distribution (Chen et al., 2008). Moreover, the assumption of a spherical initial cluster (Murray et al., 2012) fails in accounting for dipole-dipole interaction in calculating the free energy of droplets. Among the weak points of CNT is the difficulty of experimentally measuring many parameters required to be used in CNT, requiring the parameterization of these quantities and making them vary over several orders of magnitude between studies (Krämer et al., 1999; Ford, 2004).

With these considerations in mind, we now turn to the main aspects of CNT for homogeneous and heterogeneous freezing. The formation of a cluster (also named nucleus) of the new phase is the first step during nucleation. In this process, n molecules from the actual phase form a cluster of the new phase. This occurs because of local density fluctuations of the old phase from a supersaturated state. In order for this cluster to continue growing and for the phase transition to take place, an energy barrier must be overcome. The free energy change during this process, ΔG, is given by

$$\Delta G = A\sigma - n\Delta\mu \tag{3.13}$$

where n is the number of molecules in the cluster, A is the surface area of the new cluster, σ is the interfacial free energy, $\Delta\mu$ is the difference in the chemical potential between molecules in the initial and new phase. The first term in Eq. 3.13 is positive and corresponds to the increase in free energy due to the formation of a cluster with surface area A. The second term represents the decrease in free energy associated with the change in chemical potential as the system transitions from the initial phase to the new phase. Using the relation $\Delta\mu = k_B T \ln S$, where K_B is the Boltzmann constant, T the absolute temperature, and S the supersaturation ratio, together with the expression for the number of molecules in a cluster, $n = V_T/V_1$ (with V_T the total cluster volume and V_1 the volume of a monomer), we can rewrite the Eq. 3.13 as

$$\Delta G = G_s - G_v = A\sigma - \frac{V_T}{V_1} K_B T ln S \tag{3.14}$$

where we have made explicit that the first term in Eq. 3.13 is associated with the surface area of the cluster (G_s), and the second term is related to the volume of the cluster (G_v). Figure 3.2 depicts two scenarios for the energy barrier (Eq 3.14). The teal lines represent the case where the system is in an unsaturated environment. In this case, both G_s (dashed line) and $-G_v$ (dotted line) are positive, and as a consequence, ΔG increases as the radius of the new cluster (R_p) increases. This implies that the energy

required to form a new cluster continuously grows with size, making the phase transition energetically unfavorable. In contrast, the orange lines illustrate the case of a supersaturated environment. As in the previous case, G_s remains positive (dashed line), but the volume-related term is now always negative ($-G_v < 0$, dotted line). This new dynamic causes the energy required for cluster growth to reach a maximum value (ΔG^*) at a specific radius, known as the critical radius (R_c). If the cluster grows slightly beyond this critical radius, it becomes energetically favorable for the cluster to continue growing.

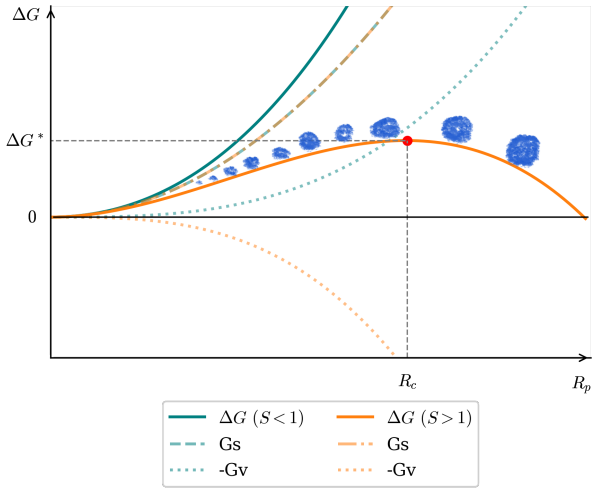


Figure 3.2.: Free energy required for cluster formation under unsaturated (teal lines) and supersaturated (orange lines) conditions. Dark blue colored circles illustrate the growth of the cluster.

The critical radius of the cluster, R_c, can be obtained by setting $\partial \Delta G / \partial R_p = 0$ in Eq 3.14 to get

$$R_c = \frac{2\sigma V_1}{K_B T ln S} \tag{3.15}$$

We now seek to determine the number of nuclei produced per unit time and volume. We introduce the steady-state rate of nucleation J as the number of nuclei per unit time per unit volume as

$$J = A \exp(-\frac{\Delta G_c}{K_B T}) \tag{3.16}$$

where ΔG_c is the energy barrier (ΔG) evaluated at R_c, and A is the pre-exponential factor. For a discussion of the nucleation kinetics and how J is calculated, the reader is referred to Seinfeld and Pandis (2016). We now extend our nucleation rate expression to Eq. 3.17 to account for kinetic effects. Specifically, we introduce an additional energy barrier that liquid water must overcome to break hydrogen-bond linkages in order to be incorporated into the ice lattice:

$$J = \frac{K_B T}{h} \exp(-\frac{\Delta F_{diff}(T)}{K_B T}) n \exp(-\frac{\Delta G_c(T)}{K_B T}) \tag{3.17}$$

where h is the Planck's constant, n ($\approx 10^{15}$ cm^{-2}) is the number density of water molecules at the ice nucleus/water interface, ΔF_{diff} is the diffusion activation energy of a water molecule to cross the water/ice embryo interface (Zobrist et al., 2007).

Now, let us consider the case in which the nucleation of a liquid droplet happens over the surface of an insoluble foreign surface. The major effect that the presence of the particle has over the nucleation is the alteration of the free energy barrier according to

$$\Delta G^*_{het} = \Delta G_{hom} f(m,x) \tag{3.18}$$

where ΔG_{hom} corresponds to ΔG in Eq. 3.14. The contact parameter m is the cosine of the contact angle θ between the nucleus and the substrate (Fig 3.3) and it is given by

$$m = cos\theta = \frac{\sigma_{SV} - \sigma_{SL}}{\sigma_{LV}} \tag{3.19}$$

where σ_{xy} are the interfacial tensions between the different phases (V: gas phase, L: liquid phase), and the substrate (S).

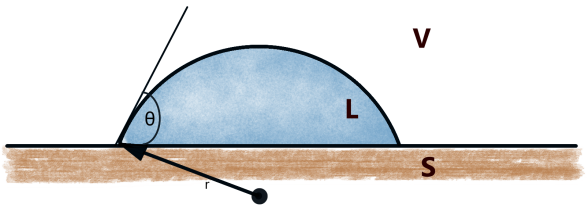


Figure 3.3.: Cluster formation on the surface of an insoluble particle. θ is the angle between the surface of the particle and the cluster (tangent line at the point where the solid particle (S), the liquid cluster (L), and the initial phase (V) meet).

In reality, atmospheric particles are not flat and they have curvature. This is taken into account through the function $f(m,x)$ (Seinfeld and Pandis, 2016):

$$f(m,x) = 1 + \left(\frac{1-mx}{g}\right) + x^3\left[2 - 3\left(\frac{x-m}{g}\right) + \left(\frac{x-m}{g}\right)^3\right] + 3mx^2\left(\frac{x-m}{g} - 1\right) \tag{3.20}$$

with

$$g = \left(1 + x^2 - 2mx\right)^{1/2} \tag{3.21}$$

and with

$$x = \frac{R'_p}{R_c} \tag{3.22}$$

where R'_p is the radius of the particle. Figure 3.4 shows the behavior of $f(m,x)$ for 4 different cases of x:

1. Small particle: If the particle is infinitesimally small, it is highly curved. As a consequence, $R'_p \to 0$ and $x = 0$. In this case, there is no effect of the foreign particle on the energy barrier, and $\Delta G^*_{het} = \Delta G^*_{hom}$.

2. $R'_p < R_c \to x < 1$: If the particle size is smaller than the critical radius (e.g. $x = 0.7$, dashed green line). At small contact angles, the foreign particle lowers the energy barrier. As the contact angle increases, this effect diminishes and approaches the same energy barrier as in the case without the particle.

3. $R'_p > R_c \to x > 1$: When the particle radius is already larger than the critical radius, the energy barrier in the presence of the particle at a contact angle of 0° is zero (dotted green line), meaning nucleation occurs instantaneously. As the contact angle increases, the energy barrier increases until it reaches the same value as in the homogeneous case.

4. Macroscopic droplet or flat surface: When the particle is much larger than the critical radius, x can be considered as $x \to \infty$, and the curvature effects of the foreign particle surface become negligible. This can also be interpreted as the cluster resting on a flat surface (Fig. 3.3). In this case, $f(m,x)$ reduces to $f(m) = \frac{1}{2}(2+m)(1-m)^2$ (dashed orange line in Fig. 3.4), and the energy barrier can be expressed as

$$\Delta G^*_{het} = \Delta G^*_{hom} f(m) \tag{3.23}$$

Additionally, when $x \to \infty$, Eq 3.18 corresponds to Eq 3.23

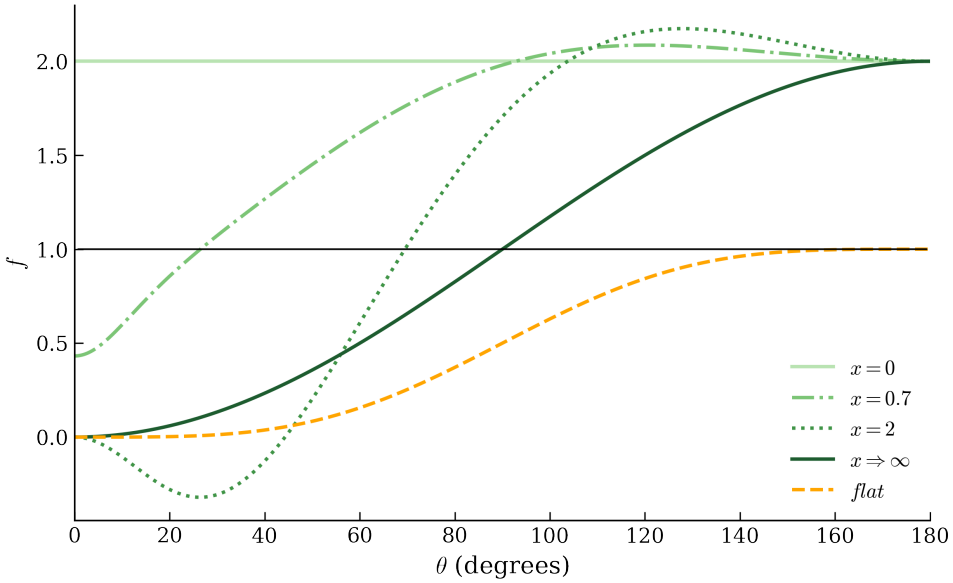


Figure 3.4.: Behavior of $f(m,x)$ for different cases. With $x = 0$ (green solid line), $x = 0.7$ (dashed green line), $x = 2$ (dotted green line), $X \to \infty$ (solid dark green line), and considering the case in which the surface of the particle is flat (dashed orange line).

Finally, the form for j_{het} (now in units of number of critical nuclei appearing on a unit surface area per unit time) is as in Eq 3.17 but using ΔG^*_{het} instead of ΔG_c. Once the nucleation rate is known, the number of ice crystals formed, N, is obtained according to (Pruppacher et al., 1998; Hoose and Möhler, 2012)

$$N(t) = \int_0^t J(t')B(t')dt' \tag{3.24}$$

where the temperature dependence has been changed for the time dependence (freezing rate) and $B(t')$ is the volume (V) of the system available for nucleation or the surface area (S_{area}) of foreign particles available for nucleation.

When comparing the number of nucleated particles predicted by CNT with experimental observations, significant discrepancies are often observed. These differences are in part due to the fact that key input parameters required by CNT for specific particle types, such as contact angle, water activity, and others, are frequently unknown or uncertain. As a result, various efforts have been made to improve CNT in order to better match theory with laboratory and field measurements. Table 3.2 summarizes some of these approaches.

Table 3.2.: Approaches used to describe ice nucleation.

Approach	Summary	Reference
Stochastic description	* Each droplet in an array has the same material and the same probability of freezing. * Single probability function. * Each nucleation event will lead to a droplet freezing. * This is the case for pure water freezing.	Murray et al. (2011)
Multicomponent stochastic description	* Consider mixture of particles, each one with its own nucleation probability.	Broadley et al. (2012), Stoyanova et al. (1994)
Singular description	* Neglect time dependence * Nucleation will occur at a particular site at a particular set of conditions (Temperature and RH)	Pruppacher et al. (1998)
Extended Modified Liquid Drop (EMLD)	* New definition of cluster and different barrier energy that CNT	Reguera and Reiss (2004)
Density Functional Theory (DFT)	* Based on microscopic molecular interactions. * Knowledge of intermolecular potentials of the system is required.	Nyquist et al. (1995)
Diffusive Interface Theory (DIT)	* Takes into account the interaction between several molecular layers in the phases interface * Takes into account bulk solid and liquid values of enthalpy and entropy. * Interface energy is size dependent. * Applicable to weakly polar substances	Gránásy (1993)

3.3.2. Active Surface Site Approach

Given the conceptual assumptions and experimental limitations of the CNT (Sect. 3.3.1) many alternative approaches have emerged to overcome these limitations and at the same time improve the representation of the number of INP for different aerosol types under various ranges of temperature and supersaturation. Among them, the active surface site approach (singular description in Table 3.2) is frequently used because it is easy to measure in experiments and translate to parameterizations that depend only

on one parameter. Under this framework, it is assumed that nucleation occurs instantaneously once a specific temperature is reached, therefore, time dependence is completely neglected, i.e. a longer stay of the aerosol-droplet population at the same temperature will not change the number of formed ice crystals. The locations where this nucleation occurs are known as "active sites". These sites possess specific features that are different from those of the rest of the particle surface, allowing them to promote nucleation at specific temperatures. Nucleation of the droplet in which the particle is immersed is initiated once the temperature is lowered below the characteristic temperature of one of the active sites (Fig. 3.5). Therefore, despite the fact that one particle may have different active sites with different nucleation temperatures, it is the warmer temperature that initiates the nucleation. Following this idea, a population of droplets will be characterized by each droplet having a specific nucleation temperature corresponding to the active site that nucleates first.

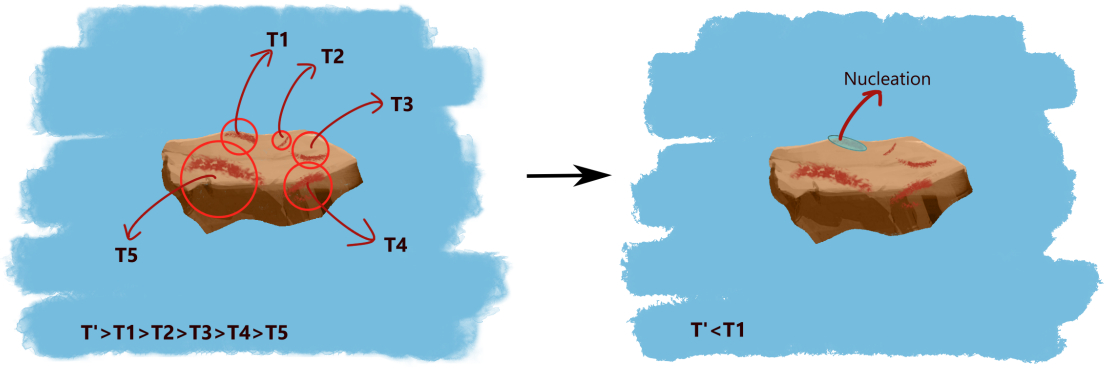


Figure 3.5.: Schematic representation of the concept of surface active sites in which an aerosol particle is immersed in a water droplet at temperature T' (blue background). Left: an aerosol particle is characterized by having different active sites (shapes inside red circles) which have specific nucleation temperatures (T1, T2, T3, T4, T5). Right: Once the temperature inside the droplet is decreased such that T2<T'<T1, the nucleation of the active site associated with T1 is triggered.

Considering the average number of active sites that become activated in an infinitesimal change of temperature on the surface of a particle, the differential nucleus concentration (Vali, 1971) is defined as

$$k(T) = \frac{1}{S_{\text{area}} N_0(T)} \frac{dN}{dT} \tag{3.25}$$

where $k(T)$ [m^{-2} K^{-1}] is the differential nucleus concentration of active sites per surface area and temperature change at temperature T, S_{area} is the surface area of the particle, and N_0 is the number of unfrozen droplets at temperature T. It is worth noting that the use of the original equation proposed by Vali (1971) has been altered changing volume to surface area (Vali, 2014). It is possible to relate the change in the number of frozen and unfrozen droplets through $dN = -dN_f$, with dN being the change in the number of

unfrozen and dN_f that in the number of frozen droplets. Considering that the probability of finding one or more active sites within dT follows a Poisson distribution (Vali, 1971) and noting that the presence of one or more active sites on the surface of the particle at temperature T leads to the freezing of the droplet, we obtain for a monodisperse aerosol

$$\frac{dN_f}{N_0(T)} = 1 - e^{-k(T)S_{\text{area}}\,dT} \tag{3.26}$$

It is possible to extend Eq. (3.26) to the case of a polydisperse aerosol as

$$\sum_{j=1}^{p} dN_{f,j} = \sum_{j=1}^{p} N_{0,j}(T)[1 - e^{-k(T)S_{\text{area},j}dT}] \tag{3.27}$$

with j being the jth size bin and p the number of size bins in the distribution. A common metric used to express the ice activity of particles is the cumulative nucleus concentration, also called ice nucleation active site (INAS) density, $n_s(T)$, which represents the number of active sites per surface area between temperature T and T'. It is possible to obtain $n_s(T)$ in two different ways. The first involves the use of Eq. (3.25) and the relationship $k(T)dT = -dn_s$. By integrating Eq. (3.25) and extending it to a polydisperse aerosol population, Eq. (3.28) is obtained:

$$\sum_{j=1}^{p} N_{f,j} = \sum_{j=1}^{p} N_{0,j}[1 - e^{-n_s(T)S_{\text{area},j}}] \tag{3.28}$$

Noting the similarities of Eq. (3.27) and Eq. (3.28), the procedure to obtain either $k(T)$ or $n_s(T)$ is the same. Expressing the exponential term as a Taylor series, we obtain:

$$\sum_{j=1}^{p} f_j = \sum_{j=1}^{p} q_j(b_j - \frac{b_j^2}{2!} + \frac{b_j^3}{3!} - ...) \tag{3.29}$$

where f_j is $dN_{f,j}$ or $N_{f,j}$, q_j is $N_{0,j}(T)$ or $N_{0,j}$, and b_j is $k(T)S_{area,j}dT$ or $n_s(T)S_{area,j}$, respectively, for Eqs. (3.27) or (3.28). Assuming that both $k(T)$ and $n_s(T)$ are independent of particle size, and that $k(T)S_{\text{area},j}\,|dT| \ll 1$ and $n_s(T)S_{area,j} \ll 1$, non-linear terms can be neglected, which leads us to the approximated equations for $k(T)$ and $n_s(t)$:

$$k(T) = -\frac{1}{dT}\frac{\sum_{j=1}^{p} dN_{f,j}}{\sum_{j=1}^{p} N_{0,j}(T)S_{area,j}} \tag{3.30a}$$

$$n_s(T) = \frac{\sum_{j=1}^{p} N_{f,j}}{\sum_{j=1}^{p} N_{0,j}S_{\text{area},j}} \tag{3.30b}$$

The second method consists of computing $k(T)$ according to Eq. (3.30a) and from there estimate $n_s(T)$ as

$$n_s(T) = \sum_{h}^{q} k_h dT_h \tag{3.31}$$

where q represents the number of dT_h intervals required to arrive at T from the initial temperature T_0, and k_h is the differential nucleus concentration at temperature T_h.

3.4. Cloud Ice Microphysics

In the previous section we discussed the different theories and approaches that describe the formation of ice crystals through homogeneous and heterogeneous ice nucleation (Sect. 3.3.1) and an alternative approach to describe ice nucleation in immersion freezing mode using the concept of active sites (Sect. 3.3.2). We now consider the evolution of ice crystals after their formation within clouds and their influence on cloud properties. Once the INPs initiate nucleation, ice crystals can grow through different mechanisms, such as diffusion from the vapor phase, aggregation, or riming. Ice number concentration can increase through secondary ice production, for example via droplet freezing and shattering (a supercooled droplet freezes, internal pressure builds, and the drop cracks/shatters, releasing several ice fragments, Lauber et al., 2018), rime-splintering, or collisional break-up. Some secondary ice production mechanisms fragment existing ice (collisional break-up), while others create new ice from supercooled droplets (droplet freezing and shattering). As secondary ice production increases the number of crystals (often without a commensurate mass increase), the mean crystal size can decrease; melting (or sublimation) also reduces individual crystal size. The initial state of nucleation, in which a few molecules have nucleated, is called an ice embryo. Once nucleated, this ice embryo will rapidly grow under favorable conditions of supersaturation into an ice crystal by vapor diffusion, i.e. water vapor molecules move from regions of high vapor concentration to regions of low vapor concentration. In case that water droplets and ice crystals coexist in a supersaturated environment with respect to water, ice crystals will grow faster than water droplets. This is because the supersaturation with respect to ice is higher in a supersaturated water environment. For example, in Fig. 3.1, when $S_w = 1$ (supersaturated environment with respect to water), the value of S_i (supersaturation with respect to ice) is always greater than S_w for temperatures smaller than 270 K. In this way, the water vapor gradient driving diffusional growth is larger for an ice crystal than for a cloud droplet (Fig. 3.6a). A special case of diffusional growth is when water droplets coexist in the vicinity of ice crystals. As mentioned, water vapor will be deposited on the surface of the ice crystal leaving a zone of low vapor pressure, given that saturation vapor pressure over water is higher than over ice at the same temperature, water droplets will evaporate to replenish the vapor and maintain vapor equilibrium. As this process continues, ice crystals will grow at the expense of evaporating cloud droplets. This is known as the Wegener-Bergeron-Findeisen process, and it is more efficient in mixed-phase clouds (Fig. 3.6b). Aggregation occurs when two or more ice crystals collide and clump together (Fig. 3.6c). The efficiency with which these ice crystals stay together after a collision is referred to as "sticking efficiency" and it depends on temperature. At warmer temperatures, ice crystals have a thicker quasiliquid layer around their surface, increasing the efficiency with which ice crystals clump after a collision. This process is more relevant for a couple of degrees warmer than $-10°$C. Another way in which

an ice crystal can increase in size is through riming (Fig. 3.6d). This occurs when an ice particle collides with a liquid particle that freezes upon contact, leading to an increase in the size of the ice crystal. Figure 3.6e and f show the formation of secondary ice crystals. In Fig. 3.6e a slower-falling ice crystal is fractured by graupel, after the collision the initial crystal is divided into multiple smaller ice crystals. Secondary ice production can also occur when supercooled droplets of appropriate size and temperature are captured by graupel (Fig. 3.6f), called Hallet-Mossop or rime-splintering process (Lohmann et al., 2016). The rime-splintering process operates mainly between -8 and -3° C when both small and large droplets are present; laboratory studies report $\approx$ 1 splinter per $\approx$ 250 accreted droplets (250 droplets captured by a graupel particle) with diameter larger than 24 µm, or equivalently $\approx$ 350 splinters per mg of accreted liquid droplets (Mossop, 1976; Field et al., 2017).

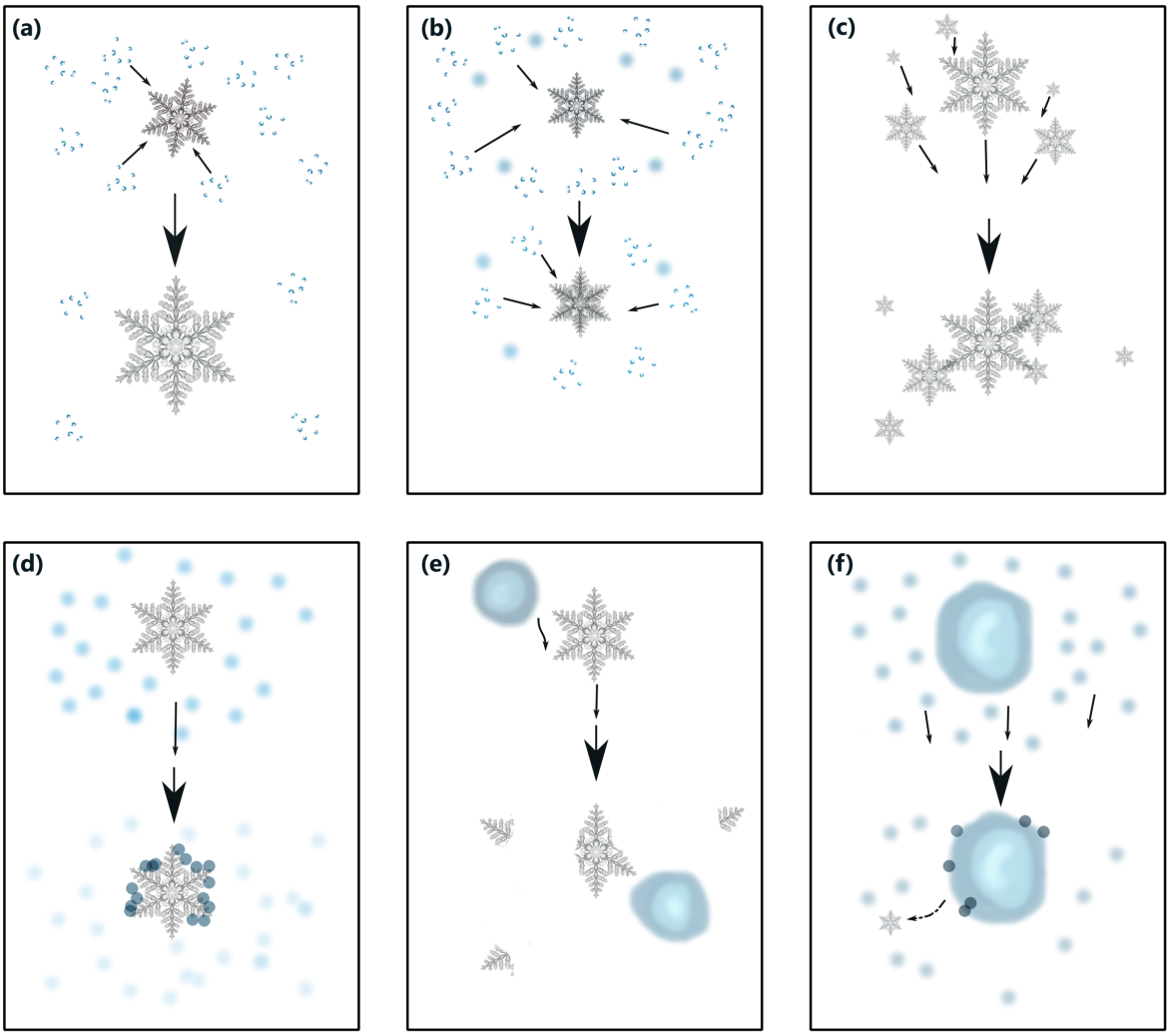


Figure 3.6.: Schematic of different processes that an ice crystal particle undergoes within a cloud. a) Diffusional growth, b) Wegener-Bergeron-Findeisen proces, c) aggregation, d) riming, e) collision, f) rime-splintering process. Small blue dots represent water vapor, medium blue circles represent cloud droplets, large blue shape represents graupel, and gray figure represents ice crystal.

4. Methods and Data

4.1. Laboratory ice nucleation experiments

In the following sections, the field campaigns whose data underlie the ice nucleation experiments are presented, specifically, the Iceland and Morocco campaigns conducted by colleagues (Sect. 4.1.1). Additionally, I participated in the J-WADI campaign in Jordan (Appendix C), but samples from Jordan returned too late for us to include them in our ice nucleation experiments.
Next, the MICOS campaign is introduced (Sect. 4.1.2), within which the ice nucleation experiments, AIDA, AIDAm, and INSEKT, were conducted. Section 4.1.3 presents the methodology to estimate particle surface area, in which an ellipsoidal particle shape is considered and contrasted with the common spherical simplification. Finally, Sect. 4.1.4 details the approach used to characterize the particle size distribution obtained from the samples injected in AIDA for ice nucleation experiments, covering particle sizes from the sub-micrometer range to several tens of micrometers.

4.1.1. Collection and preparation of natural dust samples from Morocco and Iceland

The mineral dust samples used to investigate dust ice nucleation activity were collected during field campaigns in Morocco (2019) and Iceland (2021) by partner researchers. The Morocco campaign was organized by the European Research Council project entitled FRontiers in dust minerAloGical coMposition and its Effects upoN climaTe (FRAGMENT) and the Iceland campaign co-organized between FRAGMENT and the project Iceland as a model for high-latitude dust sources – a combined experimental and modeling approach for characterization of dust emission and transport processes (HiLDA) (e.g. González-Flórez et al., 2022; Panta et al., 2023; González-Romero et al., 2023, 2024; Panta et al., 2025). Soil sampling in Morocco was carried out in September 2019 in the area of L'Bour (29°49'30" N, 5°52'25" W, Fig. 4.1 reproduced from Panta et al. (2023)), a dry lake located in the lower Draâ valley at the edge of the Sahara. The zone consists of a flat surface with a smooth hard crust in which under favorable weather conditions dust was frequently emitted. For a detailed characterization of the area and aerosols, the reader is referred to Panta et al. (2023), and González-Romero et al. (2023).
Icelandic soil samples were collected from a terminal lake connected to a nearby glacier (N 64°54'55", W 16°46'35", 710 m a.s.l., Fig. 4.2 reproduced from González-Romero et al. (2024)) in the Vatnajökull National Park in August 2021 (Dupont et al., 2024b). The area was flat and devoid of substantial roughness elements. Flooding from the nearby glacier regularly supplied fresh sediment to the area. A detailed

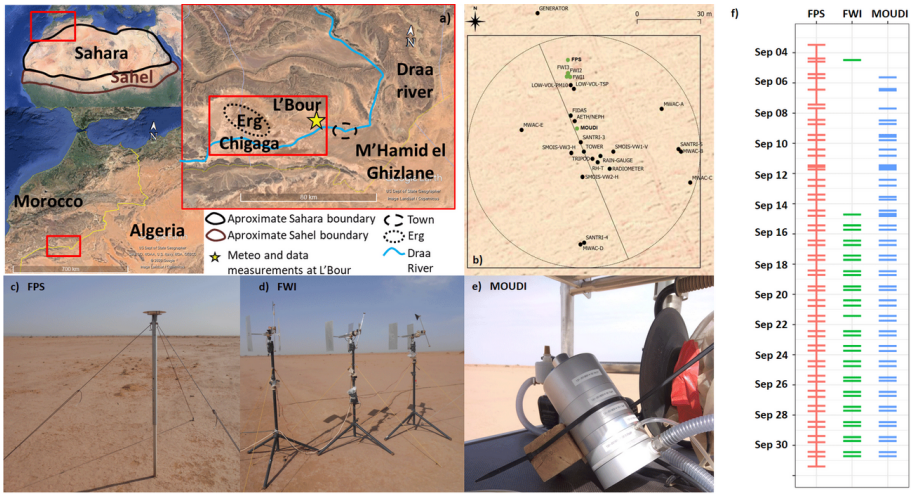


Figure 4.1.: Reproduced from Panta et al. (2023) (a) Northwestern Africa showing the area of operation of the FRAGMENT campaign. The main location of L'Bour is shown by a star and is located close to the Drâa river basin. (b) Schematic representation of different instruments used in the campaign, with green dots highlighting those instruments used for single particle analysis. (c) Flat-plate deposition sampler (FPS). (d) Free-wing impactor (FWI). (e) Cascade impactor (micro-orifice uniform deposit impactor, MOUDI). (f) Sampling schedule of particle collection using different techniques. The horizontal bar represents the start and end of the sampling time. Note that due to very short sampling time for FWI and MOUDI, the two bars (start and end) appear as one. Panel (a) was created using Google Earth (US Dept of State Geographer, Data SIO, NOAA, US Navy, NGA, GEBCO, © 2020 Google, Image Landsat/Copernicus).

description of the study site and sediment characteristics is presented in González-Romero et al. (2024) and of the properties of the emitted dust in Panta et al. (2025).

For both locations, sampling was done with a metallic shovel (50 cm^2 area, and 2 cm depth) in a stratified random sampling approach across 9 equally sized squared strata covering a total area of $100 \times 100\,m^2$. After collection, samples were stored in plastic bags and transported to the laboratory where they were dried for 24-48 h at 50°C. Three samples were collected within each stratum and then combined to three separate representative samples (hence each consisted of one sample per each stratum). Size-segregated samples for injection into AIDA (Sect. 4.1.2.1) were generated from the collected samples using both sieving and a cascade impactor. The procedure is described in Parra et al. (2014). In short, a cascade impactor Retsch TYP PI-1 was used, allowing separation into a maximum of seven stages ranging from 0.3 µm to >20 µm in diameter. Approximately 0.2 g of the sample that has been previously sieved through a 63 µm mesh was placed into the initial stage of the impactor, as instructed by the manufacturer. The air flow through the impactor was held constant at 2.4 $m^3\ h^{-1}$ with a compressed air pressure of 3–20 bars to disaggregate the particles before entering the impactor. To determine the mass of the sample collected in each stage, each ring of the impactor was weighed before and after the segregation process using a balance (with a precision of 0.0001 g).

Subsequently, the particle size distribution (PSD) was measured using a Malvern Mastersizer 2000 (Malvern Instruments Ltd), which employs the laser diffraction method based on Mie scattering theory (ISO 13320-1). The instrument is capable of sizing particles ranging from approximately 0.02 µm

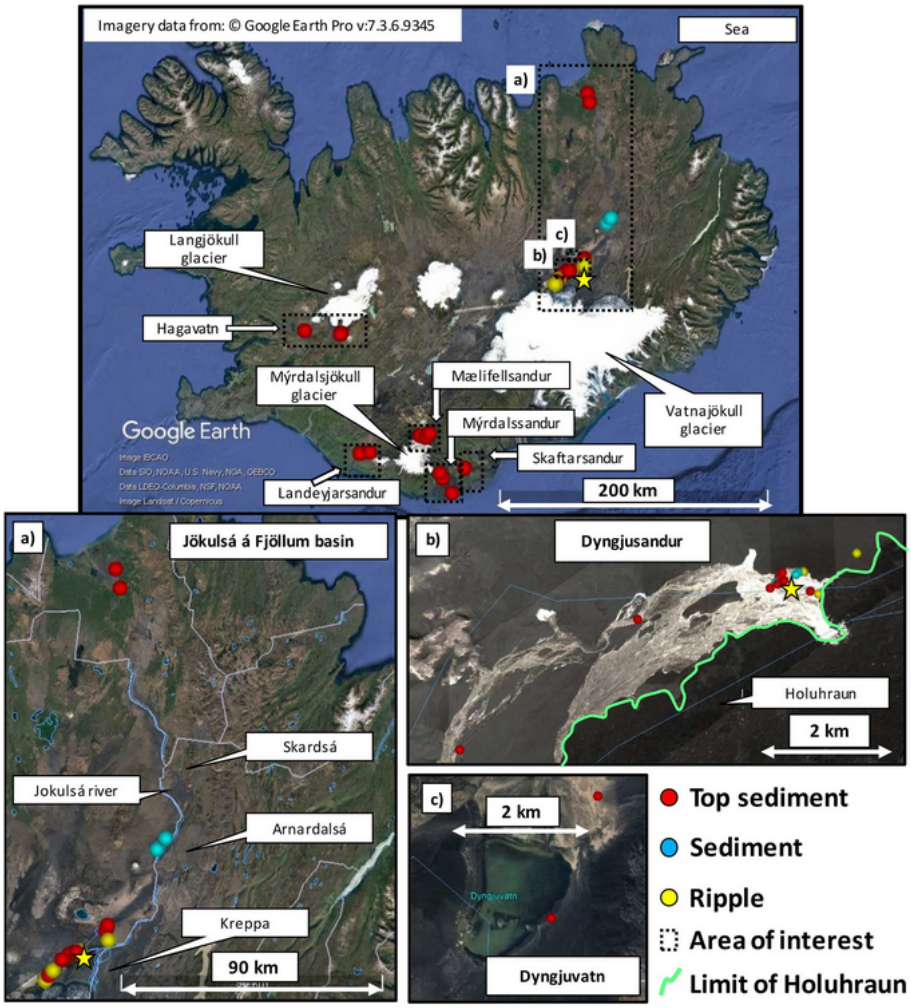


Figure 4.2.: Reproduced from González-Romero et al. (2024) Location of Iceland dust hotspots and samples. The green polygon marks the limits of Holuhraun lava field. Dashed black lines mark the area of the different dust hotspots in Iceland, and dots represent samples as top sediments (red), sediments (blue), and aeolian ripples (yellow). Basemap: imagery data from © Google Earth Pro v: 7.3.6.9345. Jökulsá á Fjöllum is marked as (a), and AVIRIS data flight images were used in the zoom-in of Dyngjusandur (b) and Dyngjuvatn (c) for a more updated vision of the lakes. The yellow star represents the experimental site.

to 2000 µm. Ethanol was used as dispersant. The refractive index for the dispersant and particles was 1.360 and 1.520, respectively. The technique yields volume-based particle size distributions, reporting diameters of equivalent spheres assuming a spherical shape.

4.1.2. MICOS campaign

The *Dust-induced ice nucleation: Effects of MIneralogical COmposition and Size* (MICOS) campaign took place from 21 November to 9 December 2022 with a total of 32 expansions in the Aerosol Interaction and Dynamics in the Atmosphere (AIDA) chamber. Our main focus was to study the ice nucleation activity of coarse ($2.5 \leq D < 10$ µm) and super-coarse ($10 \leq D < 62.5$ µm) particles defined in terms

of the volume-equivalent (geometric) diameter (D). Details about specific modifications developed and implemented in AIDA are given in Sect. 4.1.2.1.

4.1.2.1. AIDA and AIDAm cloud chamber

The AIDA chamber was an 84 m^3 aluminum vessel located in a thermostatic housing. The chamber allowed the monitoring and control of relevant variables such as temperature, pressure, and humidity. Ice and water supersaturation conditions were achieved in the chamber by expansion cooling with a mechanical pump, enabling the particles to act as INPs or as CCN (Cotton et al., 2007). In addition, the temperature inside the vessel was monitored with five thermocouples located at different levels. Given the larger size and inertia of the bigger particles, their injection into the chamber, residence time, and measurement in the chamber pose challenges, because these particles tend to settle faster and do not follow the airstream as smaller and lighter particles would do. For this reason, a new injection method was implemented for AIDA, in which a valve was used to flush the aerosol samples into the AIDA vessel using synthetic air at 4 bar for 10 seconds. Once particles were injected into the vessel, the aerosol PSD was measured online with two aerodynamic particle sizers (APS, range 0.523 - 19.81 µm; TSI GmbH, USA), one on a horizontal and another on a vertical sampling line, and a scanning mobility particle sizer (SMPS, range 0.014- 0.82 µm ; TSI GmbH, USA) on a horizontal sampling line. The total particle number concentration in the chamber was measured with a condensation particle counter (CPC3010, TSI, USA) using the horizontal sampling line. To identify and measure ice, and to extend the measured PSD to larger sizes, we used two optical particle counters (OPC) Welas 1 (detection range 0.7 - 46 µm) and Welas 2 (detection range 5 - 240 µm; Palas GmbH). Figure 4.3 shows a schematic of the facility and the instruments used during the experiments. It is worth noting that the newly developed AIDA mini (AIDAm) (Vogel et al., 2022) was also used during our experiments. AIDAm enabled us to perform multiple consecutive expansions similar to the ones from AIDA for aerosol sampled directly from AIDA. The size distribution for AIDAm was obtained with the same approach used for AIDA as a combination of APS-SMPS and Welas OPC (Sect. 4.1.4), but using the APS-SMPS sensors within AIDA together with the OPC located inside AIDAm (Vogel et al., 2022). Experiments with samples from each location (Morocco and Iceland) were conducted at 3 different initial temperatures, each between 248.15 K (-25 °C) and 257.15 K (-16 °C).

During each experiment in AIDA and before expansion, AIDA was used to sample particles to nuclepore filters for immersion freezing experiments with INSEKT, extending the temperature range that is achievable with AIDA.

All experiments consisted of the same steps: First, dust was injected into the chamber. During one hour, the aerosol number concentration distribution was measured every 6 minutes at constant temperature and pressure, sampling for INSEKT filters (Sect. 4.1.2.2) and electron microscopy at different sampling times, and multiple expansions with AIDAm were performed. Second, to ensure sufficient aerosol concentration, particularly of the large size fraction, the same aerosol sample type was injected again,

followed by the measurement of the PSD during the 6 minutes after injection. Subsequently, the AIDA expansion was carried out, in which temperature and pressure were decreased, leading to an increase in the supersaturation with respect to water and ice and promoting the droplet formation onto the particles and ice nucleation in immersion freezing mode. Once the expansion ended, AIDA was cleaned, removing all particles from the previous experiment by flushing with purified air until residual particle or gas concentrations return to background levels. In most cases, two experiments were conducted per day. According to Ullrich et al. (2017) and Vogel et al. (2022), the relative error for the INAS density obtained from AIDA and AIDAm is approximately 40 %.
Table 4.1 and Table 4.2 present an overview of the experiments conducted together with the corresponding temperature at which the first ice formation was observed.

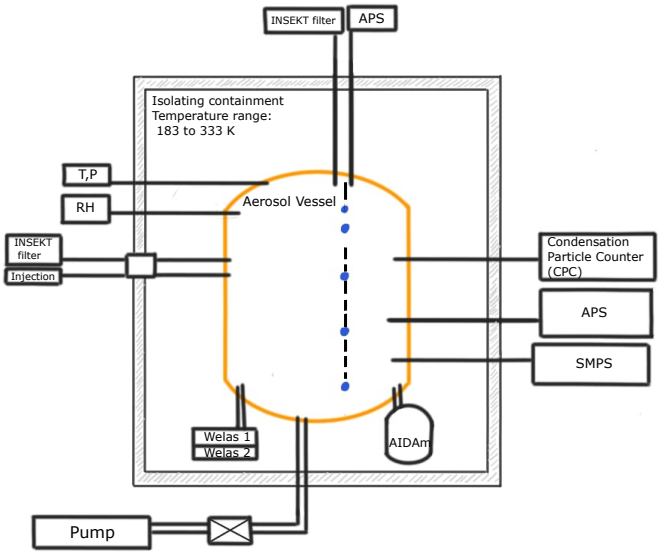


Figure 4.3.: Schematic representation of AIDA with the main instruments involved in the experiments.

4.1.2.2. INSEKT freezing assay

The Ice Nucleation Spectrometer of the Karlsruhe Institute of Technology (INSEKT) is a freezing assay, in which small volumes of clean water and aerosol solutions of interest are tested to determine their ice nucleation activity in immersion freezing mode as a function of temperature. A detailed explanation of the setup and working principle can be found in Schiebel (2017). The samples tested in INSEKT were collected from AIDA at two different locations, one at an intermediate height with a horizontal sampling line and the other one at the top of the chamber with a vertical sampling line (Fig. 4.3). The samples were collected on filters with a 0.2 µm mesh size (Whatman Nuclepore track-etched polycarbonate membranes, 47 mm) pretreated with a 10% H_2O_2 solution and rinsed with deionized water. Filters using the vertical sampling line were sampled for 20 minutes, and those using the horizontal sampling line for 30 minutes prior to AIDA expansion. After sampling, the filters were stored in sterile petri dishes, wrapped

Table 4.1.: Conditions during the AIDA experiments conducted with Moroccan samples. ID: experiment identifier, $C_{n,ae}$: initial (before chamber expansion) total number concentration, d_n: mean diameter for the number concentration size distribution, S_{ae}: initial total surface area concentration, $d_{1,s}$ and $d_{2,s}$ mean diameter of the bimodal surface area size distribution, T_{start}: temperature at which the first ice formation was observed.

Id	$C_{n,ae}$ $[10^8\, m^{-3}]$	d_n $[\mu m]$	S_{ae} $[10^8\, \mu m^2 m^{-3}]$	$d_{1,s}$ $[\mu m]$	$d_{2,s}$ $[\mu m]$	$T_{\textbf{start}}$ $[K]$
5	1.4	0.34	14.8	1.76	32	249.4
9	0.82	0.44	11.0	1.44	30	254.8
10	0.09	0.32	1.95	1.2	24	252.6
13	1.20	0.48	4.34	0.98	29	250.0
14	0.37	0.40	1.38	1.1	20	250.6
16	2.92	0.82	7.45	0.97	18	249.5
20	2.71	0.44	11	1.00	41	254.6
21	0.05	0.70	3.79	1.1	30	256.1
23	0.73	1.10	2.88	1.11	23	253.4
24	4.98	1.12	13.6	0.99	34	255.9
25	2.51	0.86	8.27	1.14	28	256.6
26	1.49	0.98	6.44	1.25	41	251.9
27	0.99	1.34	3.54	1.20	24	251.6
28	1.02	1.17	3.61	0.98	14	251.0
29	2.65	0.44	3.05	1.12	4.5	250.7

in aluminum foil, and frozen. For INSEKT experiments, each selected petri dish was unfrozen and the filter was suspended in 8 mL nanopure water that had been passed through a 0.1 µm syringe filter. Subsequently, the solution was placed on a rotator for 20 minutes. After concluding the rotation, the solution and 10 times dilution (to extend the temperature at which ice nucleation occurs) were prepared; later, 50 µL volumes were pipetted into 192 wells of two polymerase chain reaction (PCR) plates. The PCRs were introduced into the freezing mechanism and cooled at a constant cooling rate of 0.33°C min^{-1}. The freezing of wells was detected through changes in brightness using a camera mounted vertically and parallel to the plates (EO-23122, Edmund Optics monochrome camera). To rule out impurities in our samples, control freezing experiments were performed in which wells with pure water were tested to verify that the background freezing due to impurities was low compared to that of the samples. At each temperature interval, INP concentrations were obtained based on the frozen fraction of the wells, i.e. the number of frozen wells divided by the total number of wells (Vali, 1971), as (Schiebel, 2017)

$$C_{n,\text{INP},corr}(T) = -\frac{\eta}{V_{well}}\frac{V_{sol}}{V_{air}}[\ln(\frac{N_u(T)}{N_{all}}) - \ln(\frac{N_{u,bgr}(T)}{N_{all,bgr}})] \tag{4.1}$$

where $C_{n,\text{INP},corr}(T)$ is the INP concentration at temperature T, η is the dilution factor, V_{well} is the volume of each well, V_{sol} is the volume of the solution in which the filter was immersed, V_{air} is the volume of air used to sample the particles to the filter, $N_u(T)$ and $N_{u,bgr}(T)$ are the number of unfrozen wells for the aerosol solution and water control at temperature T (where bgr stands for background), respectively,

Table 4.2.: Conditions during the AIDA experiments conducted with Icelandic samples. ID: experiment identifier, $C_{n,ae}$: initial (before chamber expansion) total number concentration, d_n: mean diameter for the number concentration size distribution, S_{ae}: initial total surface area concentration, $d_{1,s}$ and $d_{2,s}$ mean diameter of the bimodal surface area size distribution, T_{start}: temperature at which the first ice formation was observed.

Id	$C_{n,ae}$ $[10^8\, m^{-3}]$	d_n $[\mu m]$	S_{ae} $[10^8\, \mu m^2 m^{-3}]$	$d_{1,s}$ $[\mu m]$	$d_{2,s}$ $[\mu m]$	$T_{\textbf{start}}$ $[K]$
3	0.54	0.48	3.97	2.00	27	249.7
6	0.76	0.91	13.7	3	28	244.9
11	1.89	0.91	14.1	2.00	36	249.7
12	0.40	1.4	2.97	2.02	31	249.6
15	2.53	0.51	8.08	1.7	28	249.5
17	1.87	0.41	6.66	2.00	31	253.5
19	2.58	0.53	12.0	2.02	31	252.9
22	1.70	0.52	7.64	2.24	27	253.1
30	0.46	0.45	2.25	2.08	21	245.9
31	0.42	0.40	2.35	2.04	31	247.2
33	1.71	0.82	5.85	2.10	29	247.3
34	0.91	0.51	8.24	2.88	29	247.5

and N_{all}, $N_{all,bgr}$ are the initial amount of wells for the aerosol solution and water control, respectively. INSEKT measurements of INAS density have an error of about 70 % (Vogel et al., 2022).

4.1.3. Surface area estimation

In order to obtain the differential nucleus concentration ($k(T)$) or the cumulative nucleus concentration, INAS density ($n_s(T)$) (Sect. 3.3.2) the surface area of the particles is needed. Previous studies have assumed that mineral dust particles can be approximated to spherical shapes (Niemand et al., 2012; Ullrich et al., 2017). However, newer studies on the shape of mineral dust have found that ellipsoids are better shape approximations (Chesler et al., 2022; Huang et al., 2023; González-Romero et al., 2024). Furthermore, the deviation of the aspect ratio (AR) from unity (AR-1) and the height-to-width ratio (HWR) of these ellipsoids both follow a log-normal distribution (Huang et al., 2020). Using ellipsoids as approximation for mineral dust shape, we computed the surface area using the globally averaged values (i.e., compiled across mineral dust source regions worldwide) of the AR and HWR distributions (Huang et al., 2020), i.e. a median AR of 1.70 ± 0.03, a median HWR of 0.40 ± 0.07, a geometric standard deviation for AR-1 of 0.70 ± 0.02 and for HWR of 0.73 ± 0.09 (Huang et al., 2020). Following a similar procedure as in Huang et al. (2020), volume-equivalent (geometric) diameters of ellipsoidal dust particles were obtained with Monte Carlo sampling from the AR-1 and HWR log-normal distributions. The surface area of each generated ellipsoidal dust particle is computed. Then, particles with the same volume-equivalent geometric diameter are grouped and the mean surface area is obtained. Combining the properties of our optical sensor (González-Flórez et al., 2022), with a wavelength centered at 0.44 µm, and a scattering angle from 85 to 95°, and the refractive index of our samples (detailed in Sect. 4.1.4), the conversion

from optical to geometric diameters was carried out based on Table S1 reported in (Huang et al., 2021). Figure 4.4a depicts the relationship between optical and geometrical diameter for the characteristics of our sensors and samples: for sizes smaller than 1 µm the geometric and optical diameters are similar, but for larger sizes the relationship changes, with the optical diameter initially smaller than the geometric diameter up to approximately 7 µm and larger thereafter. Building on this optical-to-geometric conversion, Figure 4.4b presents the surface area for the volume-equivalent geometric diameter for both ellipsoidal and spherical shapes; the two curves diverge with increasing diameter, reflecting the growing effect of particle asphericity on surface area at larger sizes.

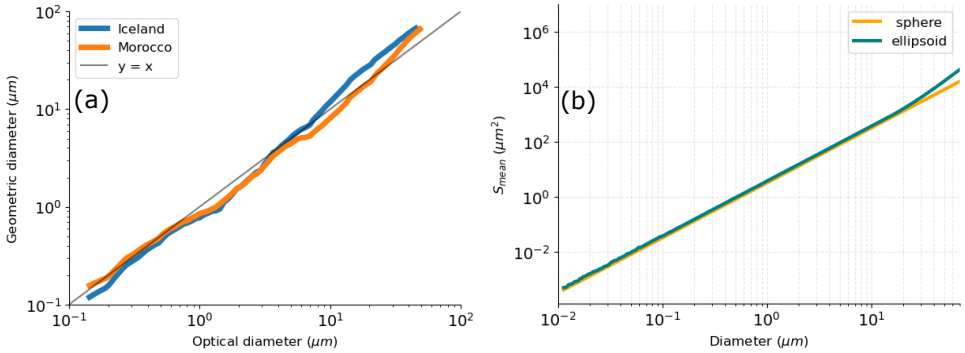


Figure 4.4.: a) Relationship between optical and geometrical diameter for Morocco and Iceland. Optical sensor with wavelength center at 0.44 µm, and 85 to 95° scattering angle, b) Surface area, S_{mean}, as a function of volume-equivalent diameter assuming spherical and ellipsoidal shapes for globally averaged values of mineral dust AR and HWR distributions.

4.1.4. Dust aerosol particle size distributions in AIDA and AIDAm

The dust aerosol number PSDs were obtained with APS, SMPS, and OPC. One APS was located at the top of the chamber sampling with a vertical line, and another APS and SMPS were located at an intermediate height sampling with a horizontal line. The additional vertically sampling APS was installed to identify and avoid possible losses from gravitational settling in the horizontal lines. For large particles, the number PSDs were measured with Welas 2 (an explanation of the threshold used is provided below). SMPS and APS were combined by merging overlapping size bins. The size distribution of the mobility diameter from the SMPS and the size distribution of the aerodynamic diameter from the APS are converted to size distributions of the volume equivalent diameter. Welas measurements were converted from optical to geometric diameter considering triaxial ellipsoidal shapes. The complex refractive index for Morocco was set to $n = 1.49 + 0.0015i$, where the real part 1.49 accounts for the refraction (phase velocity) and the imaginary part 0.0015 for the absorption (González-Flórez et al., 2022). For Iceland, the complex refractive index was set to $n = 1.59 + 0.004i$ (Baldo et al., 2023). For both Morocco and Iceland, we used an AR of 1.46 and a HWR of 0.45 (Huang et al., 2021; Panta et al., 2023), from which the optical-to-geometric diameter conversion of Fig. 4.4a (Sect. 4.1.3) was obtained.

To reduce measurement noise and minimize rapid fluctuations in concentration, particularly for smaller particle sizes, a moving average over 3 neighboring size bins was applied to the SMPS-APS data. After converting both datasets (SMPS-APS and Welas) to their respective geometric diameters, they were overlaid for comparison. Due to the reduced efficiency of the APS at larger particle sizes (beyond $\approx 3-4$ µm), a decline in measured particle counts is observed, while Welas reported higher concentrations at the same diameters. We used the intersection of measurements from APS and Welas, i.e. the transition point where the APS measurements fall below those of the Welas, as the threshold beyond which we utilized Welas data. However, due to the decreased efficiency of both instruments near their overlapping zone, the merged size distributions often exhibit an unrealistic dip in the transition region. However, this does not significantly affect the final results (see Sect. 5.1.2). Additionally, two other issues were encountered during the measurement of PSDs in AIDA. The first was the presence of residual monodisperse polystyrene latex (PSL) spheres used for calibrating the optical sensors. The second was that the CPC measured a lower particle concentration than the optical sensor during expansion, which is not physically realistic because the CPC's measurement range is broader than that of the optical sensor. The first issue was easily addressed, as the PSL particles exhibited a characteristic and clearly noticeable peak at the same diameter in all measurements, making them easy to identify and exclude from the PSD. The second issue was resolved by scaling the initial PSD (prior to expansion) to the maximum concentration observed during expansion. This approach is justified based on a common assumption in AIDA experiments, in which all particles nucleate into CCN. Therefore, the total particle number before and after expansion is conserved. Figures 4.5 and 4.6 show the surface area size distribution of the samples injected into AIDA, as well as the mean surface area size distribution of multiple experiments with the same sample ID for samples in AIDAm. The mean values and standard deviations of the multiple expansions in AIDAm are shown in Figs. 5.8 and 5.9 for Morocco and Iceland, respectively, prior to expansion for each experiment, as obtained using the approach described earlier. It is important to mention that due to technical problems with AIDAm in 7 out of 30 experiments (IDs 5, 10, 11, 12, 14, 20, and 21), no AIDAm expansions were carried out in those experiments. Additionally, Figs. 4.5 and 4.6 present the surface area distribution measured with laser diffraction (LD, Sect. 4.1.1) after sieving the samples, grouped by the stage of the cascade impactor they were collected from (Sect. 4.1.1). Although it relies on a different measurement principle than the other sensors, laser diffraction yields PSDs that are in reasonable agreement with those obtained from the combined SPMS-APS-Welas approach. The largest differences between the two methods are observed for IDs 5, 9, 10, 12, and 34, where the surface area distribution obtained with the combined instruments (SMPS-APS-Welas) tends to show higher values for diameters larger than 10 µm than the LD distributions. Conversely, experiment ID 29 exhibited a different behavior compared to both the combined instruments (IDs 25 and 28) and the LD technique. The reasons for this behavior are not clear.

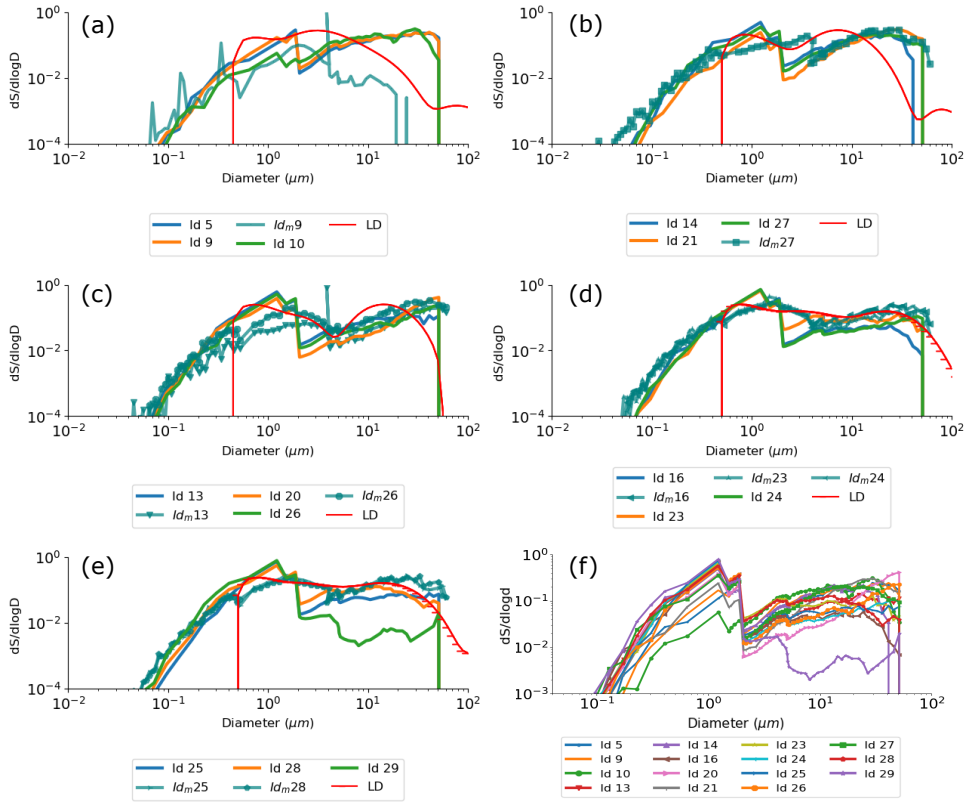


Figure 4.5.: Normalized surface area distribution measured during a 5-minute interval directly before AIDA (ID) and AIDAm (ID_m) expansion for Morocco for experiment a) ID: 5, 9, 10, ID_m: 9; b) ID: 14, 21, 27, ID_m: 27; c) ID: 13, 20, 26, ID_m: 13, 26; d) ID and ID_m: 16, 23, 24; e) ID: 25, 28, 29, ID_m: 25, 28; and f) for all experiments in AIDA. Additionally, the surface area distribution measured with laser diffraction (LD) technique after sieving the samples presented. The experiments are grouped according to the stage of the cascade impactor they were obtained.

4.2. The ICON-ART Modeling Framework

Simulations of dust aerosol particle emission, transport, and atmosphere physics state and properties, were performed with the ICOsahedral Nonhydrostatic (ICON) model in combination with the Aerosols and Reactive Trace gases (ART) extension, which enables the representation of aerosol and trace gas dynamics within the ICON atmospheric model.

4.2.1. ICON

ICON is a flexible, scalable, high-performance modeling framework for weather, climate and environmental prediction jointly developed by the German Weather Service (DWD), the Max Planck Institute for Meteorology (MPI-M), the German Climate Computing Center (DKRZ), the Karlsruhe Institute of Technology (KIT), and the Center for Climate Systems Modeling (C2SM). ICON employs an icosahedron-based unstructured triangular mesh to solve a set of prognostic variables (Gassmann and Herzog, 2008). The horizontal resolution is denoted as RxBy: Rx splits each icosahedral edge into x equal segments and

By applies y recursive bisections, so the total number of triangular cells is $n_c = 20x^2 4^y$ and the effective grid spacing is $\overline{\Delta X} \propto \sqrt{\frac{1}{x2^y}}$.
Table 4.3 presents the number of cells and effective grid resolution associated to a set of grids.

Grid	Number of cells	Effective grid resolution (km)
R2B04	20 480	157.8
R2B05	81 920	78.9
R2B06	327 680	39.5
R2B07	1 310 720	19.7
R2B08	5 242 880	9.8
R2B09	20 971 520	4.9

Table 4.3.: Total number of horizontal cells for a global domain and effective grid resolution for a set of ICON grid resolutions. From coarser (R2B04) to finer (R2B09) resolutions.

ICON was designed with scalability and flexibility in mind, offering the possibility of running global simulations on a single grid, limited-area (ICON-LAM) simulations, and global or limited-area simulations with refined nests. In ICON, nesting supports one-way and two-way parent–child coupling (multiple child domains per level), with dedicated interpolation, nudging, and feedback zones; vertical nesting is also possible, primarily by using a lower model top in the child domain, and optionally a different vertical level distribution. Limited-area runs use the same code base and add lateral boundary handling (Zängl et al., 2022; Deutscher Wetterdienst (DWD), 2024). For more information about nested domains and ICON capabilities, the interested reader can check the official ICON tutorial (Deutscher Wetterdienst (DWD), 2024).
Additionally, ICON offers three physics packages; these are numerical weather prediction (NWP), climate simulation (Pham et al., 2021), and large eddy simulation (Dipankar et al., 2015). The model is nonhydrostatic and formulated on the SLEVE (Smooth LEVel VErtical) terrain-following hybrid height-based coordinate, which smooths the influence of orography with height and ensures accurate representation of vertical transport and small-scale processes, especially relevant for convection and gravity waves (Zängl et al., 2015). The governing equations are discretized using a finite-volume method for mass-conserving transport, coupled with a semi-implicit semi-Lagrangian scheme for time integration. Vertical mixing and subgrid-scale processes are parameterized using a suite of physical parameterizations (Zängl et al., 2015).

4.2.2. ART

The ART extension is a modular framework integrated into ICON to simulate the spatiotemporal evolution of atmospheric tracers, including aerosols, reactive gases, and their interactions with meteorology, radiation, and cloud microphysics. It was mainly developed at KIT. It is primarily used for atmospheric composition modeling, climate-chemistry interactions, and aerosol-cloud-radiation feedback studies. ICON-ART solves the prognostic equations for tracer concentrations along with atmospheric

state variables, enabling online coupling between meteorology and chemistry/aerosol processes. The tracer transport follows the same advection scheme as ICON's dynamics, ensuring consistency and mass conservation. The physical and chemical processes and parameterizations used in ICON-ART are listed in the same sequence as ICON-ART computes them (Rieger et al., 2015; Hoshyaripour et al., 2025):

1. Emissions (natural and anthropogenic).
2. Sedimentation: treating separately monodisperse and polydisperse aerosols.
3. Turbulent diffusion and deposition.
4. Microphysics.
5. Chemical reactions (via mechanisms like MOZART or MECCA).
6. Aerosol dynamics.
7. Washout: different parameterizations are used for monodisperse (it is assumed that raindrops are monodisperse) and polydisperse aerosols.
8. Cloud cover.
9. Radiation.

The numerical time integration of individual processes is carried out step by step; that is, the tendency due to a given process is calculated using the respective prognostic variables, which have already been updated by the preceding processes. Once all processes have been updated for the current time step, the simulation advances in time and the procedure is repeated. Figure 4.7 illustrates the coupling of ART into ICON. This coupling is achieved through interface modules within ICON that contain subroutines responsible for calling ART modules. These interface modules ensure that ICON can still function independently when ART is not activated. The sequence of these calls for a complete time integration step is also shown in Fig. 4.7. Blue-colored rectangles represent processes implemented in ICON, while orange-colored rectangles correspond to processes implemented in ART. In ICON, fast physics includes saturation adjustment, turbulent diffusion, and microphysics. In ART, fast physics includes turbulent diffusion, washout, and chemical reactions. Similarly, slow physics in ICON consists of radiation, convection, and cloud cover, whereas in ART, it includes vertical transport due to subgrid-scale convection (Rieger et al., 2015; Hoshyaripour et al., 2025).

4.2.3. Dust emission representation in ART

ICON-ART simulates mineral dust emissions through an online, physically based parameterization that considers wind-driven dust uplift under dry conditions. The dust emission module is an adaptation of earlier schemes developed for the COSMO-ART model (Vogel et al., 2006) and later adapted and extended

within ICON-ART (Rieger et al., 2015). The dust emission flux in ICON-ART is online-coupled to the atmospheric dynamics and land-surface schemes. It is computed at each physics time step at erodible land grid points and depends primarily on the surface-layer friction velocity u_* and on a threshold u_{*t}, which is increased by soil moisture and by vegetation/roughness (drag partition). Additional factors include near-surface air density, stability, and land-surface conditions (e.g., snow or crusting) (Hoshyaripour et al., 2025). Emission occurs only when the friction velocity exceeds the threshold u_{*t}. ICON-ART assumes a three-mode lognormal size distribution for emitted dust particles, Fig. 4.8. The modes represent the clay, silt, and sand fractions. This size-resolved emission allows ICON-ART to simulate the transport and radiative effects of dust. Mineral dust emission uses the Alfaro and Gomes (2001) dust emission scheme to estimate the vertical dust flux from saltator impacts, while the horizontal saltation mass flux is parameterized as a function of friction velocity following Marticorena and Bergametti (1995), using the threshold friction velocity u_{*t} from Shao and Lu (2000). Spatial variability of emissions is constrained by pre-processed soil-texture/erodibility and source masks, which define the erodible fraction and provide soil parameters (e.g., clay fraction) entering the sandblasting efficiency. The emitted number and mass concentrations for each mode are calculated online during the model simulation and introduced into the prognostic tracer system. The respective size modes are linked to particle optical properties (used in the radiation scheme) and sedimentation velocities (used for deposition processes).

4.2.4. Two-moment cloud microphysics parameterization for mixed-phase clouds

ICON-ART uses the 2-moment cloud microphysical parameterization developed by Seifert and Beheng (2006). The scheme was developed in the context of mixed-phase clouds, designed to enhance the representation of cloud and precipitation processes in mesoscale atmospheric models, and with focus on high-resolution cloud-resolving models considering CCN effects on cloud formation. It prognoses both mass and number concentrations (2-moment scheme) for five hydrometeor types: cloud droplets, rain, cloud ice, snow, and graupel. A key feature of this parameterization is its explicit treatment of number concentrations, which enables the simulation of homogeneous and heterogeneous nucleation as well as CCN activation. This provides a more realistic representation of aerosol–cloud interactions, allowing for detailed investigations of aerosol effects on cloud microphysical and macrophysical properties.
In the following, a brief summary of the original two-moment scheme presented by Seifert and Beheng (2006) is provided, with a focus on the sections most relevant to this thesis, i.e., CCN and INP. The basic microphysical variables considered in the scheme are the partial power moments for number and mass concentration given by Eq 4.2 and Eq 4.3

$$M_c^k = \int_0^{x^*} x^k f_w(x)dx = \int_0^{\infty} x^k f_c(x)dc \tag{4.2}$$

$$M_r^k = \int_{x^*}^{\infty} x^k f_w(x)dx = \int_0^{\infty} x^k f_r(x)dc \tag{4.3}$$

respectively: Where x is the mass of a cloud drop or rain drop, $x^* = 2.6 \times 10^{-10}$ kg separates cloud drops from rain drops (which corresponds to a radius of $r^* = 40\mu m$), $f_w(x)$ is the drop size distribution (considering cloud drops and rain drops) and it has been assumed that it can be discomposed into 2 discontinuous functions $f_c(x)$ and $f_r(x)$ for cloud and rain drops, respectively. k represents the first two partial moments; with $k = 0$ being the number concentration ($M_c^0 \equiv N_c$, $M_r^0 \equiv N_r$) and with $k = 1$ the mass concentration (liquid water content; $M_c^1 \equiv L_c$, $M_r^1 \equiv L_r$).

The grid-mean bulk two-moment equations in general form can be expressed according to Eq 4.4

$$\frac{\partial M_i^k}{\partial t} + \nabla \cdot [\overrightarrow{v} M_i k] - \nabla \cdot [K_h \nabla M_i^k] + \frac{\partial}{\partial z}[\overrightarrow{v_{i,k}} M_i^k] = \mathbb{S}_i^k \tag{4.4}$$

where $i \in \{c, r\}$, $\overrightarrow{v}$ is the velocity, K_h is the turbulent diffusivity of heat, $\overrightarrow{v_{i,k}}$ is the mean sedimentation velocities, $\mathbb{S}_i^k$ represents the source terms (nucleation, collision, coalesecence, evaporation, among others). Additionally, the first two terms in Eq 4.4 represent the temporal and spatial change of the considered moment, respectively; the third term ($K_h \nabla M_i^k$) accounts for mixing due to subgrid turbulence and is the parameterization of the turbulent fluxes of hydrometeors, and the term $\frac{\partial}{\partial z}[\overrightarrow{v_{i,k}} M_i^k]$ accounts for the gravitational setting of particles.

The mass and number concentrations (first two partial moments) are coupled via the size distribution of hydrometeors, which is typically assumed to follow a functional form (e.g., gamma distribution or exponential distribution). For example, the generalized Γ-distribution is given according to Eq 4.5, where ν and μ are constants, and A and λ are coefficients that can be expressed by the number and mass densities. As many microphysical process rates (e.g., autoconversion from cloud droplets to rain) depend on both mass and number concentrations, both equations Eq 4.2 and Eq 4.3 are solved simultaneously and consistently.

$$f(x) = A x^{\nu} exp(-\lambda x^{\mu}) \tag{4.5}$$

The coupling between these two moments is explicitly shown in Eq 4.6, in which A and λ have been expressed in terms of the number and mass densities, and $\bar{x}$ is the mean particle mass ($\bar{x} = L/N$) (Seifert and Beheng, 2006).

$$f(x) = \frac{N}{\bar{x}} \left[\frac{x}{\bar{x}}\right]^{\nu} \frac{\mu}{\Gamma(\frac{\nu+1}{\mu})} \left[\frac{\Gamma(\frac{\nu+2}{\mu})}{\Gamma(\frac{\nu+1}{\mu})}\right]^{\nu+1} \times exp\left\{-\left[\frac{\Gamma(\frac{\nu+2}{\mu})}{\Gamma(\frac{\nu+1}{\mu})}\frac{x}{\bar{x}}\right]^{\mu}\right\} \tag{4.6}$$

From here, the moment of power-n can be derived and used in the general equation (Eq 4.4). This is expressed as

$$M^n = \frac{\Gamma(\frac{n+\nu+1}{\mu})}{\Gamma(\frac{\nu+1}{\mu})} \left[\frac{\Gamma(\frac{\nu+1}{\mu})}{\Gamma(\frac{\nu+2}{\mu})}\right]^n N \bar{x}^n \tag{4.7}$$

4.2.5. Nucleation of cloud ice

The number concentration of activated INPs for immersion freezing mode is obtained as the contribution from cloud and rain droplets as (Seifert and Beheng, 2006; Lüttmer et al., 2025).

$$\frac{\partial n_{imm}}{\partial t} = (C_{IMM}|_c - n_{inact})\frac{1}{\partial t} + \frac{\partial n_{imm}}{\partial t}|_r \tag{4.8}$$

Note that Eq. 4.8 differs from Lüttmer et al. (2025) by the inclusion of an additional $1/\partial t$ term to correctly account for the rate of change. The mass concentration is obtained as:

$$\frac{\partial q_{imm}}{\partial t} = \frac{\partial n_{imm}}{\partial t}|_c x_c + \frac{\partial q_{imm}}{\partial t}|_r \tag{4.9}$$

Where n_{inact} is the number of activated INP in m^{-3} and is tracked as an additional tracer according to Eq 4.10 in which τ_{inact} is the relaxation time and n_{dep} and n_{imm} is the INP number concentration due to deposition nucleation and immersion freeing, respectively (in m^{-3}); $C_{IMM}|_c$ accounts for the number concentration of activated INP for immersion freezing of cloud droplets (m^{-3}), q_{imm} is the mass concentration due to immersion freezing (kg m^{-3}), x_c is the mean cloud droplet mass (kg), and the sub-indices c and r indicate cloud or rain droplet, respectively.

$$\frac{\partial n_{inact}}{\partial t} = \begin{cases} -\frac{n_{inact}}{\tau_{inact}} & \text{if} \quad q_{tot} = \frac{\partial n_{imm}}{\partial t} = \frac{\partial n_{dep}}{\partial t} = 0 \\ \frac{\partial n_{imm}}{\partial t} + \frac{\partial n_{dep}}{\partial t} & \text{else,} \end{cases} \tag{4.10}$$

For deposition nucleation the equations take the same form as Eq 4.8 and 4.9 but the term accounting for rain droplets (terms with subindex r) is neglected, as it is assumed that for the temperature required for deposition nucleation almost all rain droplets have already nucleated. The variable $C_{IMM}|_c$ is parameterized as a function of temperature for conditions of supersaturation with respect to water and surface area (see Section 3.3.2) and it will be further explored in this thesis.

4.2.6. Cloud radiative effect

Radiation fluxes are computed online by the ecRad radiation scheme (Hogan and Bozzo, 2018) coupled to ICON-ART. ecRad is the European Centre for Medium-Range Weather Forecasts (ECMWF) modular radiative transfer package used operationally in the Integrated Forecast System (IFS) and in ICON. It computes shortwave (solar) and longwave (thermal) irradiances from the surface to the mesosphere and provides radiative heating rates and top-of-atmosphere (TOA) flux diagnostics at model levels. Using the radiative fluxes computed by ecRad, the net cloud radiative effect (CRE) at TOA is calculated according to Eq. 4.11.

$$CRE = CRE_{\mathrm{SW}} + CRE_{\mathrm{LW}} \tag{4.11}$$

where CRE_{SW} and CRE_{LW} are the cloud radiative effect for the shortwave (SW) and longwave (LW) radiation, respectively, and defined as

$$CRE_{\mathrm{SW}} = SW_{\text{all-sky}} - SW_{\text{clear-sky}}, \tag{4.12a}$$

$$CRE_{\mathrm{LW}} = LW_{\text{all-sky}} - LW_{\text{clear-sky}}, \tag{4.12b}$$

clear-sky diagnostics are computed by removing the cloud condensate and cloud fraction while keeping gases, and aerosols identical to the all-sky state. Each term in Eq. 4.12a and Eq. 4.12b is obtained as the difference between the downward and upward radiative energy flux (irradiance), $F = F^{\downarrow} - F^{\uparrow}$. According to this definition, if clouds reflect more solar radiation, all-sky outgoing shortwave flux is larger than clear-sky ($CRE_{\mathrm{SW}} < 0$) meaning a cooling of the atmosphere. On the other hand, if clouds trap longwave radiation, all-sky outgoing longwave flux is smaller than clear-sky ($CRE_{\mathrm{LW}} > 0$) meaning a warming of the atmosphere.

In order to compare the different results with a benchmark we are using NASA's Clouds Earth's Radiant Energy System (CERES, Wielicki et al., 1996) and the Energy Balanced and Filled (EBAF) monthly product (Loeb et al., 2018). CERES converts broadband radiances to TOA fluxes using empirically derived angular distribution models (ADMs) and combines Terra/Aqua polar-orbiting radiometers with GEO imagers (hourly between 60° S–60° N) to better represent the diurnal cycle; EBAF then applies an objective constraint so the global mean net TOA flux is consistent with observed heat storage (Earth's energy imbalance) (Doelling et al., 2013). EBAF Ed4.1–4.2 also provides spatially complete clear-sky fluxes for the total region (not only cloud-free footprints), which aligns the clear-sky definition more closely with how models compute clear-sky fluxes. Monthly means from EBAF at the native 1° grid were used. Area-weighted means from ICON-ART outputs to compare with CERES were computed. The comparison between CERES and the model is carried out using the absolute relative error (ARE) between the simulation (X_{sim}) and CERES (X_{CERES}) according to Eq. 4.13

$$\mathrm{ARE(X)} = 100\frac{|X_{\mathrm{sim}} - X_{\mathrm{CERES}}|}{|X_{\mathrm{CERES}}|} \tag{4.13}$$

4.2.7. Phase partitioning and occurrence of mixed-phase clouds

Ice nucleating particles affect the phase composition of clouds, affecting in which proportion clouds contain liquid droplets and ice crystals. The cloud phase composition is obtained considering the specific cloud liquid water content (q_c (kg/kg)), and the specific cloud ice water content (q_i (kg/kg)). As one of the the main focus of our work is about the influence of INPs on MPCs, we studied their influence through the cloud-phase defined according to Eq. 4.14 (Korolev et al., 2017).

$$\mu = \frac{q_i}{q_i + q_c} \tag{4.14}$$

where μ is the cloud phase; for $\mu = 0$ the cloud is purely liquid ($q_i = 0$), for $\mu = 1$ it is purely ice ($q_c = 0$), and intermediate values $0 < \mu < 1$ indicate mixed phase. The ratio is undefined when $q_i = q_c = 0$; in practice, we evaluate μ only where $q_c + q_i > 0$ and, when reporting means, we condition on MPC occurrence at the same level.

In addition to the cloud phase, MPC conditions are identified at each grid point (lat,lon,level) and time (t) when liquid and ice coexist and a temperature threshold is satisfied according to the Eq. 4.15

$$\mathrm{MPC_c}(t,h,c) = [q_c(t,h,c) > 0 \wedge q_i(t,h,c) > 0 \wedge T_{min} \leq T(t,h,c) < T_{max}] \tag{4.15}$$

with T_{min} and T_{max} specifying the mixed-phase temperature range (T_{min} = -38°C) and (T_{max} = 0°C), and $\mathrm{MPC_c}$ is the MPC condition to identify that grid point as MPC. MPC occurrence is obtained for each level (h) and column (c; lat,lon), the occurrence is the fraction of model output times with MPC at that point (expressed in percent) as

$$\mathrm{Occ}_{h,c} = 100 \times \frac{1}{N_t} \sum_{t=1}^{N_t} \mathbf{1}\{\mathrm{MPC}(t,h,c)\}. \tag{4.16}$$

where N_t is the total number of time steps, and $\mathbf{1}\{\mathrm{MPC}(t,h,c)\}$ is an indicator function: it equals 1 if MPC conditions are present at time t at (h,c) and 0 otherwise.

4.2.8. Modifications to ICON-ART

To separately track Icelandic dust, evaluate the possible source dependence of INP efficiency, and assess MPC sensitivity to source-aware parameterizations, we implemented the following modifications to ICON-ART

1. Implement source tagging by introducing tracers that identify dust emitted from Iceland and track it through transport and atmospheric interactions.
2. Implement new parameterizations based on experimental results. For the case of Iceland, two cases are considered based on the results from chapter 5: with and without size dependence.

The following describes the changes implemented to achieve the above technical steps. ICON-ART allows for the definition of new tracers through the use of "xml" files. In this way, the addition of the new tracers is reduced to the modification of the relevant files in the appropriate order. For this, the following files corresponding to the namelist `art_nml` were modified:

Listing 4.1: Modified file names and their corresponding variable name in order to include new tracers.

```
cart_aerosol_xml    = 'tracers_dustrad.xml'
cart_modes_xml      = 'modes_dustrad.xml'
cart_aero_emiss_xml = 'aero_emiss_dustrad.xml'
cart_diagnostics_xml = 'diagnostics_dust.xml'
```

The modified files are shown in Appendix A.
After applying these changes, ICON-ART includes a new set of tracers in its subroutines, enabling the tag of additional dust tracers. It is important to clarify that no new aerosol modes were added; the same three modes a, b, and c introduced in Sect. 4.2.3 and Fig. 4.8 are used consistently in all calculations. These modes apply to both tracer groups: "dustx" and "dustx_iceland", where x represents modes a, b, or c. Additionally, a geographic mask was implemented in the ART emission subroutines to ensure that each tracer group receives emissions solely from its designated source (Iceland or elsewhere). The general idea behind the mask is to use the tracer group names ("dustx" and "dustx_iceland") to determine from which regions dust emissions are allowed. For instance, if the tracer is "dusta_iceland", the subroutines recognize the name and restrict emissions to the area defined as Iceland. Conversely, if the tracer is "dusta", emissions are permitted globally, except over Iceland. This approach enables the addition of new tracers while requiring minimal changes to the existing subroutines, only a simple if statement is needed to distinguish between the two cases. The changes made to the code are described below.

- Additional arguments were added in the subroutine `art_emission_interface` to the function art_emission_dust. These are `p_patch` and `TRIM(this%modenames(1))`
- The function art_emission_dust was modified as shown in appendix A, in which the mask is created to allow emission for different parts of the world depending on the tracer's name.

In addition to the changes described above, other modifications were required to fully implement the new tracers into the ICON-ART subroutines. That is, specific tracer names are directly referenced in certain calculations. Without going into detail, these include subroutines related to optical properties such as aerosol optical depth, backscattering, and others.
Additionally, modifications to the ice-nucleation subroutines are necessary. However, since the ART ice-nucleation subroutines are currently incompatible with the main ICON branch (see Appendix B), I used a different approach. This approach consists of bypassing the ART subroutines for ice nucleation and instead using those implemented in ICON. While the main advantage of ART lies in its capability to represent chemistry reactions, this does not pose a limitation for our study since the focus is on the interaction between dust and super cooled water rather than on dust aging or chemical transformations. In this configuration, mineral dust is used as ice-nucleating aerosol (icpl_aero_ice = 3). Consequently, the subroutines associated with the variable icpl_aero_ice must be modified to incorporate the new parameterizations and tracers. As in ART, the ICON subroutines related to ice nucleation limit the dust fields and their derived quantities, such as total number concentration and total surface area, to the three default dust modes either by explicitly referencing dust variable names or by assuming three modes. Therefore, the following subroutines were modified to explicitly include the new tracers "dustx_iceland", as well as the corresponding parameterizations and diagnostic output variables (e.g., INP concentrations from Iceland and from the rest of the world, total surface area for each tagged group, and combined totals across all sources):

- `mo_nwp_gscp_interface`
- `aerosol_prepare_inas_dust`
- `mo_run_config`
- `mo_advection_utils`
- `mo_atmo_model`
- `cloudice2mom_run`
- `cloudice2mom`

With this new approach and the implemented modifications, the output analysis revealed no numerical artifacts or errors. Therefore, this configuration was adopted for the simulations.
Additionally, the parameterization referred to as SHLD accounts for the mineralogical composition of the Icelandic samples used in the immersion-freezing experiments (Sect. 6.1.4) and proposes adding a factor that multiplies the surface area to account for changes in mineralogy with size, and thus the variation of ice-nucleation activity with size, according to Eq. 4.17.

$$n_s(T) = \frac{\sum_j N_{j,f}(T)}{\sum_j N_{j,0} S_{j,\text{area}} f_j} \tag{4.17}$$

where n_s is the INAS density, $N_{j,f}$ is the number of activated particles, $N_{j,0}$ is the initial number of particles; $S_{j,\text{area}}$ is the surface area, f_j is the proposed term that accounts for changes in ice-nucleation activity associated with changes in mineralogy and defined for a specific size range, and j denotes the size bins that constitute the PSD. Since mineral dust particles in ICON-ART are defined by lognormal distributions, it is necessary to match the size ranges covered by each lognormal distribution to the definition of f_j. The effective factor, f_{eff}, is calculated as the mode weighted by the surface area according to Eq. 4.18

$$f_{\text{eff}} = \frac{\int_0^\infty f(d') d'^2 P(d') dd'}{\int_0^\infty d'^2 P(d') dd'} \tag{4.18}$$

Where $f(d')$ is the correction factor (f_j), d' is diameter, and $P(d')$ is the lognormal probability density function for each dust mode. Using the parameters of each dust mode (Fig. 4.8), Eq. 4.18 has an analytical solution and yields the following initial f_{eff} values for each mode: 0.07496 (dusta), 0.04350 (dustb), and 0.03163 (dustc). These parameters are integrated in the ICON ice nucleation subroutine when the total surface area concentration is calculated for each dust mode. It is important to mention that f_{eff} is recalculated online at each grid point and time step from the locally evolved modal parameters of each mode as the aerosol scheme transports and modifies the size distribution.

4.2.9. Simulation setup

The simulation setup consists of two domains coupled through two-way nesting. The outer domain, run in limited-area mode (LAM), covers the entire longitudinal range and extends from the equator to 90° N, with a horizontal resolution of approximately 20 km (R2B07). A higher-resolution domain is nested with center over Iceland (65° N, 18.6° W) and covers the range between 54.8° W to 1.89° E longitude and 55.78° N to 76.20° N in latitude, referenced as domain 2, with a spatial resolution of about 10 km (R2B08). The integration time step is 120 s for the coarse domain and 60 s for the nested domain. Both domains share the same vertical discretization, consisting of 90 levels with a top height at 75 km. The vertical grid follows the terrain up to 16 km altitude, above which levels transition to constant spacing.
A bulk mass-flux convection scheme is applied in both domains, representing shallow, mid-level, and deep convection through an ascending plume model that mixes with the surrounding environment air (Prill et al., 2022). Specifically, the Tiedtke–Bechtold parameterization (Bechtold et al., 2008) is used. The simulations span June to August 2021, preceded by a two-week spin-up period (15–31 May). The Model output is recorded at 2 hour intervals. The period from June to August 2021 was selected because it represents the months when Icelandic dust emissions are reported to be more activity. Previous studies have shown that dust activity in Iceland peaks during summer and autumn (Meinander et al., 2022; Shi et al., 2022). Focusing on these months allows us to capture episodes of intense local dust emissions and to assess their contribution at the regional scale in comparison with external dust sources. Moreover, experimental data from the HiLDA campaign provide in-situ measurements of dust concentrations for 2021 (Sect. 4.1.1), offering an excellent opportunity to evaluate the model's ability to reproduce dust emission and transport against both observations and other model studies.
The ICON-ART LAM simulations are driven by lateral boundary conditions from ERA5 reanalysis data (Hersbach et al., 2020). Additionally, meteorological variables (e.g., wind, temperature, pressure) are spectrally nudged towards ERA5 (Pham et al., 2021), with boundary data and nudged variables updated daily.
To distinguish Icelandic dust from other sources, a dust source-tagging approach was implemented in ICON-ART (Sect. 4.2.8). In this method, separate tracers are assigned to dust emitted from Iceland and to dust originating from the rest of the world. These tagged tracers are emitted and transported using the standard ICON-ART routines, with the added capability of tracking their contributions independently. Three experiments were performed to assess the activity of mineral dust INPs in immersion-freezing mode and their effects on clouds (Table 4.4). The default experiment follows the standard ICON implementation, which does not differentiate between dust sources and assumes a uniform ice-nucleating activity for all mineral dust, irrespective of mineralogical composition (Ullrich et al., 2017). In contrast, the LLD_HLD and LLD_SHLD experiments distinguish between LLD and HLD by applying parameterizations developed from Moroccan and Icelandic samples, respectively (Vergara-Palacio et al., 2026). The PSDs of the samples used to derive both parameterizations span almost three orders of magnitude,

from 10^{-1} to ≈ 60 µm , which sets the particle size range over which the parameterizations are considered valid when applied to the dust modes of Fig. 4.8 in the model. Furthermore, the LLD_SHLD experiment uses the proposed parameterization that accounts for the size-dependent ice-nucleating activity associated with the mineralogical composition of Icelandic samples.

Experiment	Description
Default	Current default parameterization for all dust sources from Ullrich et al. (2017).
LLD_HLD	Parameterization for low-latitude dust (LLD) and, for Iceland, high-latitude dust (HLD) sources.
LLD_SHLD	As LLD_HLD but accounting for ice-nucleation activity dependence on mineralogy and particle size for Iceland.

Table 4.4.: Different experiments considered in this study. Parameterizations are used for immersion freezing mode. The Default case uses Ullrich et al. (2017); LLD_HLD and LLD_SHLD use Vergara-Palacio et al. (2026).

4.3. Deriving Dust Optical Depth (DOD) from AERONET for model evaluation

We used Level 2.0 data from the AErosol RObotic NEtwork (AERONET). Several challenges arise when using AERONET observations for model evaluation because the reported AOD includes not only mineral dust but also contributions from other aerosol types, such as sea salt, biomass-burning, smoke, and anthropogenic pollution. Consequently, isolating the dust contribution or identifying dust-dominated conditions has been the subject of numerous studies (Toledano et al., 2011; Giles et al., 2012; Velasco-Merino et al., 2018; Obiso et al., 2024). The Ångström exponent (AE), typically derived between 440 and 870 nm, is widely used as a proxy for particle size and thus for aerosol type identification (Toledano et al., 2011). Low AE values indicate coarse particles, and it is common to apply an AE threshold to classify measurements as dust-dominated. Reported thresholds generally range from 0.3 to 0.75 (Toledano et al., 2011; Kok et al., 2014; Klose et al., 2021). In some cases, this criterion is combined with a minimum AOD threshold (e.g. AOD > 0.3) to exclude possible contributions from sea salt, which can also yield low AE values (Toledano et al., 2019). Another challenge when using AERONET data for short evaluation periods is the limited data availability, since measurements are not always continuous and gaps without observations are common. In this study, the approach of using the AE as a proxy to identify dust-dominated conditions is used, where values below 0.3 are regarded as indicative of dust. However, for summer 2021, the number of cases with both AE < 0.3 and concurrent AOD measurements is scarce (Fig. 4.9). For this reason, I selected hourly AERONET measurements from 2015 to 2021 for which overlapping information on AE < 0.3 and AOD was available. I then computed the mean across years, i.e., averaging the same day and hour over multiple years, and used this climatological mean as the reference for comparison with my simulation results. To ensure robustness (i.e., to reduce interannual variability and ensure that the climatological mean is representative), only data spanning at least three years were included.

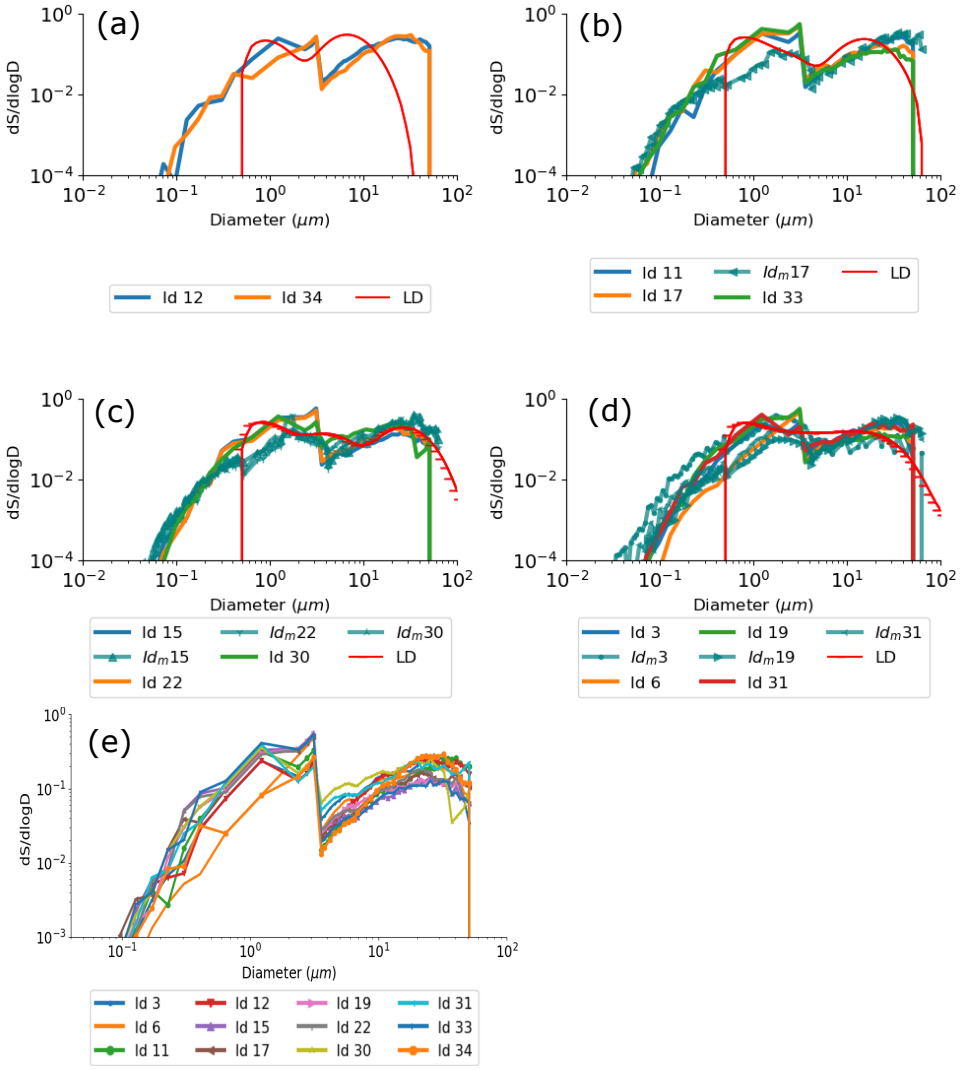


Figure 4.6.: Normalized surface area distribution measured during a 5-minute interval directly before AIDA (ID) and AIDAm (ID_m) expansion for Iceland for experiment a) ID: 12, 34; b) ID: 11, 17, 33, ID_m: 17; c) ID and ID_m: 15, 22, 30; d) ID: 3, 6, 19, 31, ID_m: 3, 19, 31; and e) for all experiments in AIDA. Additionally, the surface area distribution measured with laser diffraction (LD) technique after sieving the samples presented. The experiments are grouped according to the stage of the cascade impactor they were obtained.

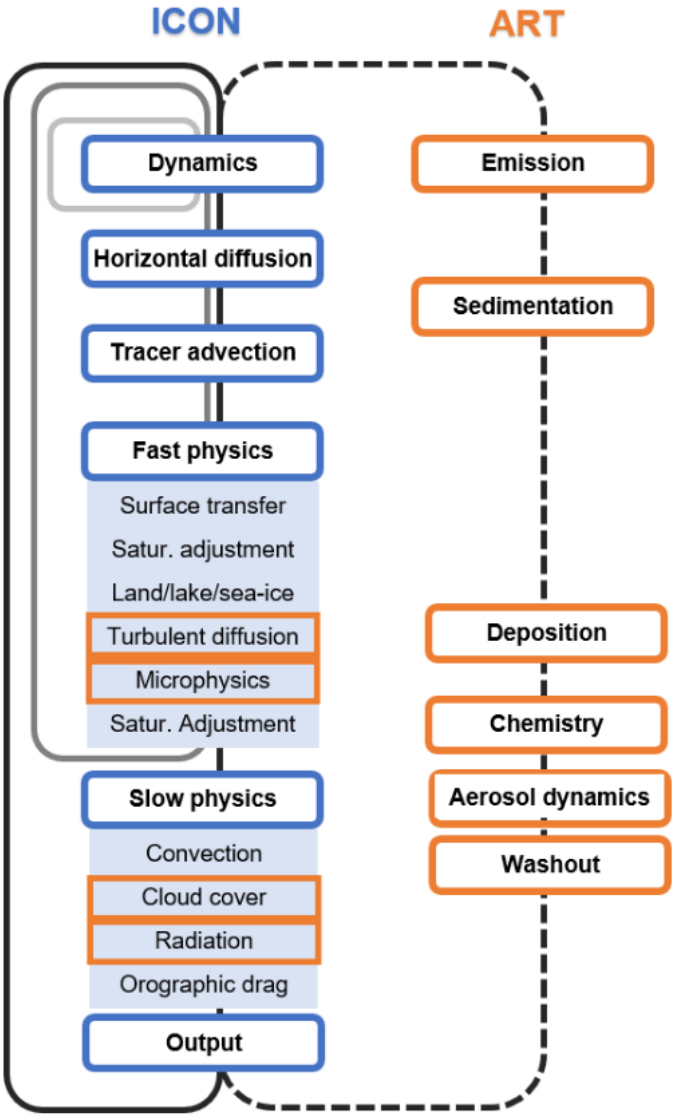


Figure 4.7.: Schematic of the coupling of ART into ICON. Blue boxes represent processes implemented in ICON, while orange boxes represent processes implemented in ART. Blue boxes with an orange frame indicate ICON processes in which ART tracers are treated within the ICON framework. Schematic taken from Hoshyaripour et al. (2025).

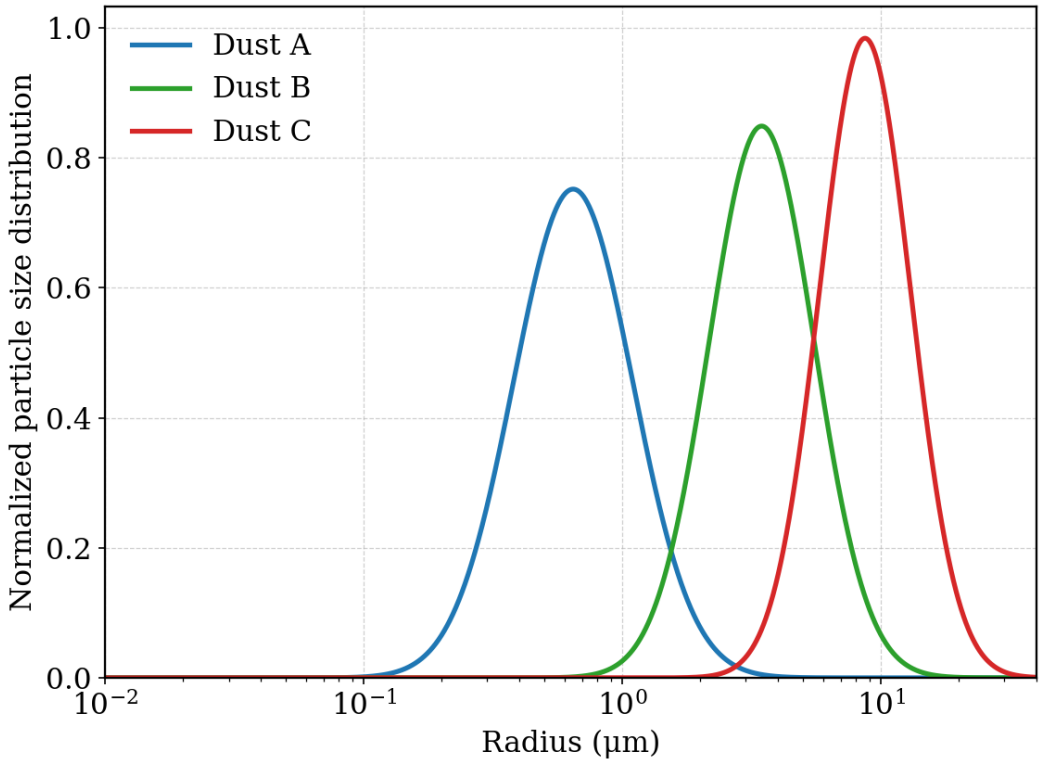


Figure 4.8.: Normalized lognormal particle size distribution for each dust mode, named dusta, dustb, and dustc, in ICON-ART. The geometric mean radius and geometric standard deviation for dusta, dustb and dustc are 0.6445 μm and 1.7, 3.454 μm and 1.6, and 8.672 μm and 1.5, respectively.

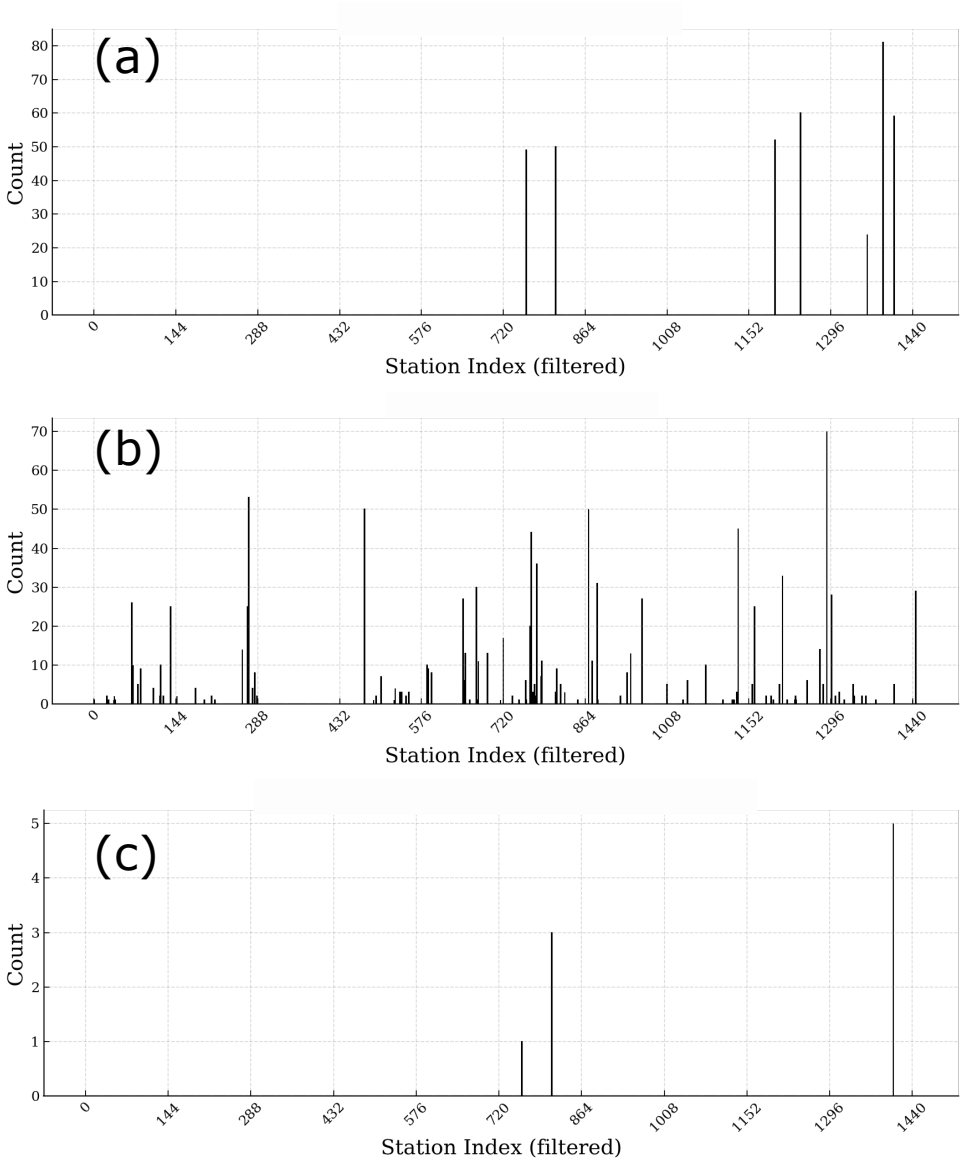


Figure 4.9.: Number of hourly AERONET measurements from June to August 2021 at all stations for (a) AOD at 551 nm, (b) AE values below 0.3, and (c) the overlap where both AOD and AE < 0.3 are available. "Station (filtered)" indicates that only stations with numerical data are included.

5. Results

5.1. Results from Laboratory Experiments

In this section, I present the results obtained from the ice nucleation experiments performed with AIDA, INSEKT, and AIDAm. In Sect. 5.1.1, I explored how the values for n_s obtained with different approaches and assumptions differ and under which circumstances the results agree. In Sect. 5.1.2, the results from AIDA and INSEKT for Moroccan and Icelandic samples are discussed considering the differential ($k(T)$) and cumulative (INAS density, $n_s(T)$) nucleus concentrations. Additionally, all experiments from AIDA and INSEKT techniques are combined to obtain a parameterization that best represents the data, considering the dependence of INAS density on temperature. Finally, in Sect. 5.1.3, I present results from AIDAm, from which I address the stability and repeatability of the experiments over time.

5.1.1. Influence of nonlinear terms on n_s

As presented in Sect. 3.3.2, the use of Eq. 3.30a and Eq. 3.30b assumes the argument of the exponential of Eq. 3.27 and Eq. 3.28 to be much less than 1. Given that we are considering particle sizes that expand over three orders of magnitude (i.e. from 10^{-1} to more than 10^{1}), it is relevant to evaluate whether or not this assumption and therefore the approximated solutions are valid. For this purpose, we computed $n_s(T)$ (a) with Eq. 3.30b and (b) including higher powers (up to 5 for stability reasons) in the Taylor series (Eq. 3.29) to obtain $k(T)$ and $n_s(T)$. For the case in which $k(T)$ is computed, Eq. 3.31 allows us to obtain $n_s(T)$. We then quantified the difference between these methods as the relative error,

$$RE = \left(\frac{|n_{s,app} - n'_s|}{n_{s,app}}\right) * 100, \tag{5.1}$$

where $n_{s,app}$ is the approximate value of $n_s(T)$ calculated with Eq. 3.30b, and n'_s is the value obtained including 5 terms in Eq. (3.29) (to obtain $n_s(T)$ directly) or with Eq. (3.31) (to obtain $n_s(T)$ through $k(T)$). To obtain the roots of Eq. 3.29 different approaches were evaluated, and Newton's method proved to be the most stable. Fig. 5.1 shows the resulting relative error for Moroccan dust for experiments with AIDA (Fig. 5.1a-b) and INSEKT (Fig. 5.1 c-d). It can be noticed that for INSEKT experiments, there is no appreciable difference between the approximated solution and the one considering higher-order terms (Fig. 5.1 c-d). This is due to the low IN activity present at the temperatures in which INSEKT experiments were carried out. On the other hand, substantial differences are observed for AIDA experiments. Experiments 5, 13, 14, 16, and 29 present the biggest differences for both methods with a relative error

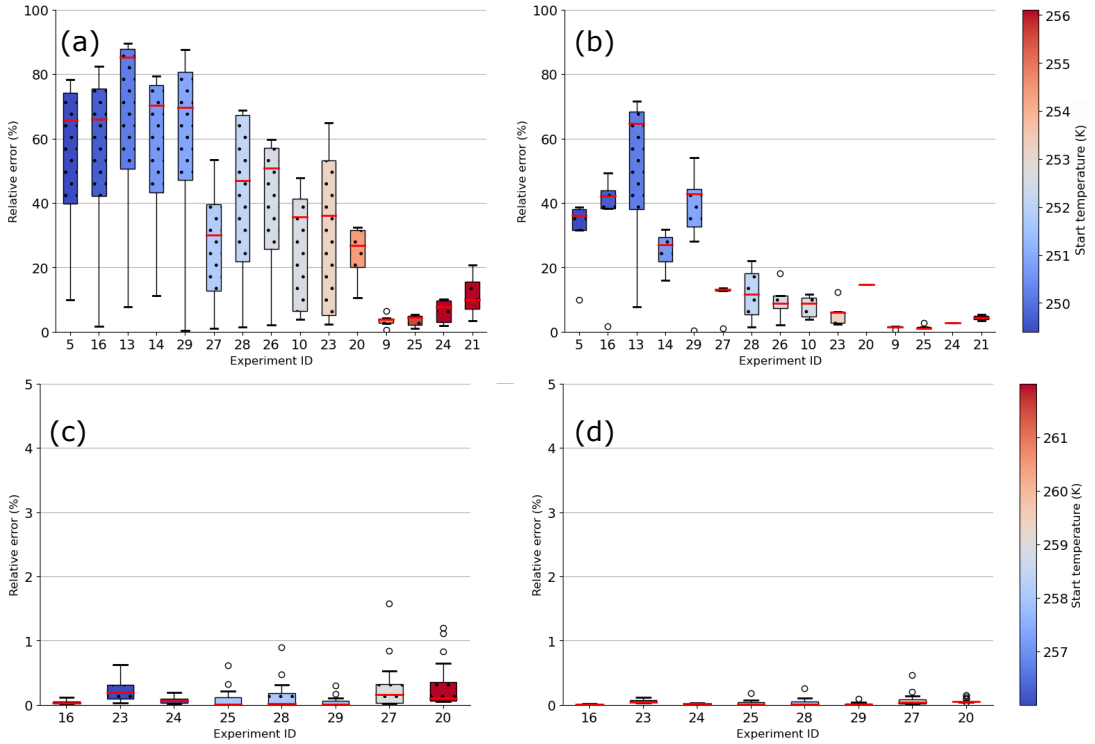


Figure 5.1.: Relative error between the different approaches of computing INAS density for Moroccan dust. The box represents the interquartile range (IQR) from the first quartile to the third quartile (Q1 to Q3), the horizontal orange line inside the box represents the median value. The whiskers extend to the smallest and largest values within 1.5 times the IQR, and outliers beyond the whiskers are shown as individual circles. Experiments are sorted by the temperature at which the first ice particle was detected, in order of increasing temperature. For AIDA experiments: (a) for polynomial of degree 5 (Eq. (3.29)) and (b) for summation of differential nucleus concentration (Eq. (3.31)). (c) and (d) as (a) and (b), but for INSEKT experiments.

closer to 90% when INAS is computed with a polynomial of degree 5 (Fig. 5.1a) and around 40% to 80% when it is obtained with $k(T)$ (Fig. 5.1b). The relative error increased with decreasing temperature during an experiment. For example, *RE* increased from experiment 26 to 29 and the start temperature in those experiments decreased from 251.9K in experiment 26 to 250.7K in experiment 29 (Tab. 4.1). Experiments conducted at the warmest temperatures (experiment IDs 9, 10, 20, 21, 23, 24, and 25) have a relative error of less than 40%. Generally, for the coldest temperatures, the error increases because the ice nucleation activity is higher (measured either through $k(T)$ or $n_s(T)$) making higher-order terms in the polynomial expression more relevant. Moreover, the use of a 5th-degree polynomial in the general expression (Eq. 3.29) is still an approximation that may be affected by numerical instability. For example, large values can cause high-degree terms to grow excessively.

Figure 5.2 presents the relative error for the Iceland experiments for AIDA and for INSEKT. The difference in the $n_s(T)$ values obtained with the different methods is almost zero for all INSEKT experiments. This is due to the low IN activity that the Icelandic samples presented at temperatures between 252 - 255 K. As was the case for the Moroccan experiments, there is a larger difference for AIDA experiments

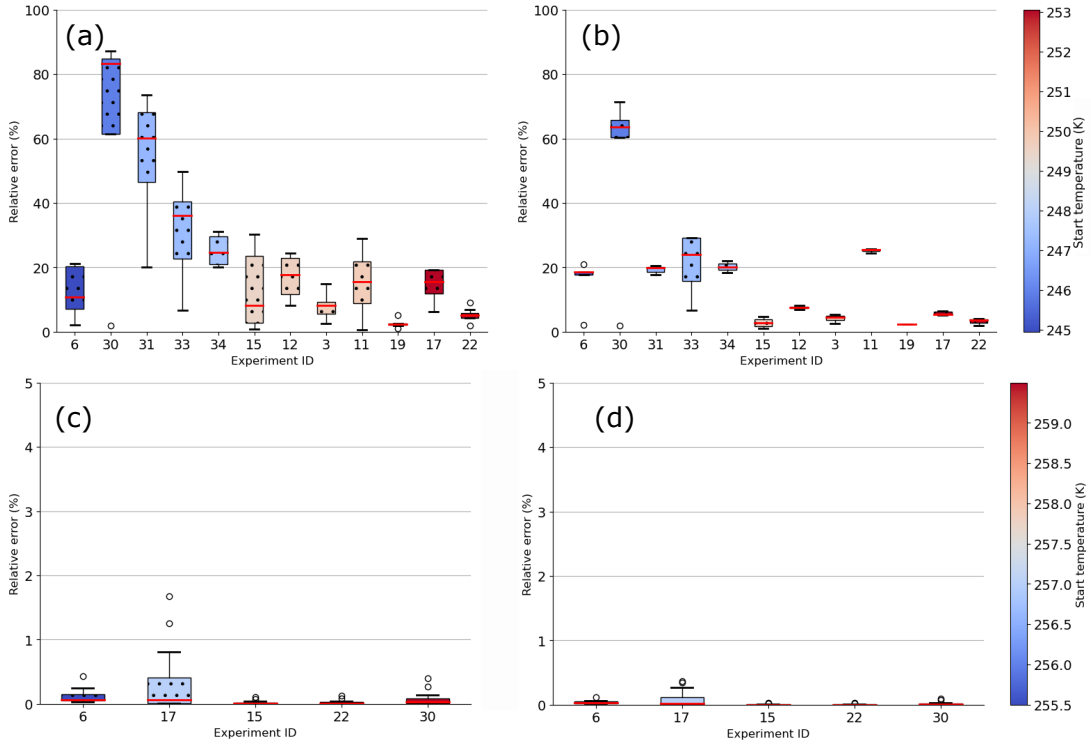


Figure 5.2.: Relative error for the different approaches of computing inas density for Iceland. The box represents the interquartile range (IQR) from the first quartile to the third quartile (Q1 to Q3), the horizontal orange line inside the box represents the median value. The whiskers extend to the smallest and largest values within 1.5 times the IQR, and outliers beyond the whiskers are shown as individual circles. Experiments are sorted by the temperature at which the first ice particle was detected, in order of increasing temperature. For AIDA experiments: (a) and (b) for polynomial of degree 5 and summation of differential nucleus concentration, respectively. For INSEKT experiments: (c) and (d) for polynomial of degree 5 and summation of differential nucleus concentration, respectively.

compared to INSEKT and a similar trend is observed, i.e. experiments at colder temperatures show larger relative differences.

We conclude that the commonly used assumption that $n_s(T)S_{\text{area},j} \ll 1$ (or equivalently $k(T)S_{\text{area},j}dT \ll 1$) needs to be revised when the surface area distribution covers several orders of magnitude and in particular when the INA is high. However, given that for most of our experiments the difference between both approaches was lower than 50% or even 30% (labels b, c, and d for Figs 5.1 and 5.2), and considering more terms in the computation of INAS did not change significantly the final fit, we will use the standard equations (Eqs. 3.30a and 3.30b).

5.1.2. Ice nucleation activity

The values of $k(T)$ and $n_s(T)$ obtained with Eqs. 3.30a and 3.30b are shown in Fig. 5.3 for Morocco and Fig. 5.4 for Iceland as a function of temperature and colored depending on the mean diameter of the surface area size distribution of the probed sample. Figures 5.3 a and b present the experimental results obtained with AIDA and c and d with INSEKT. The differential nucleus concentration, $k(T)$ (Fig. 5.3a,c)

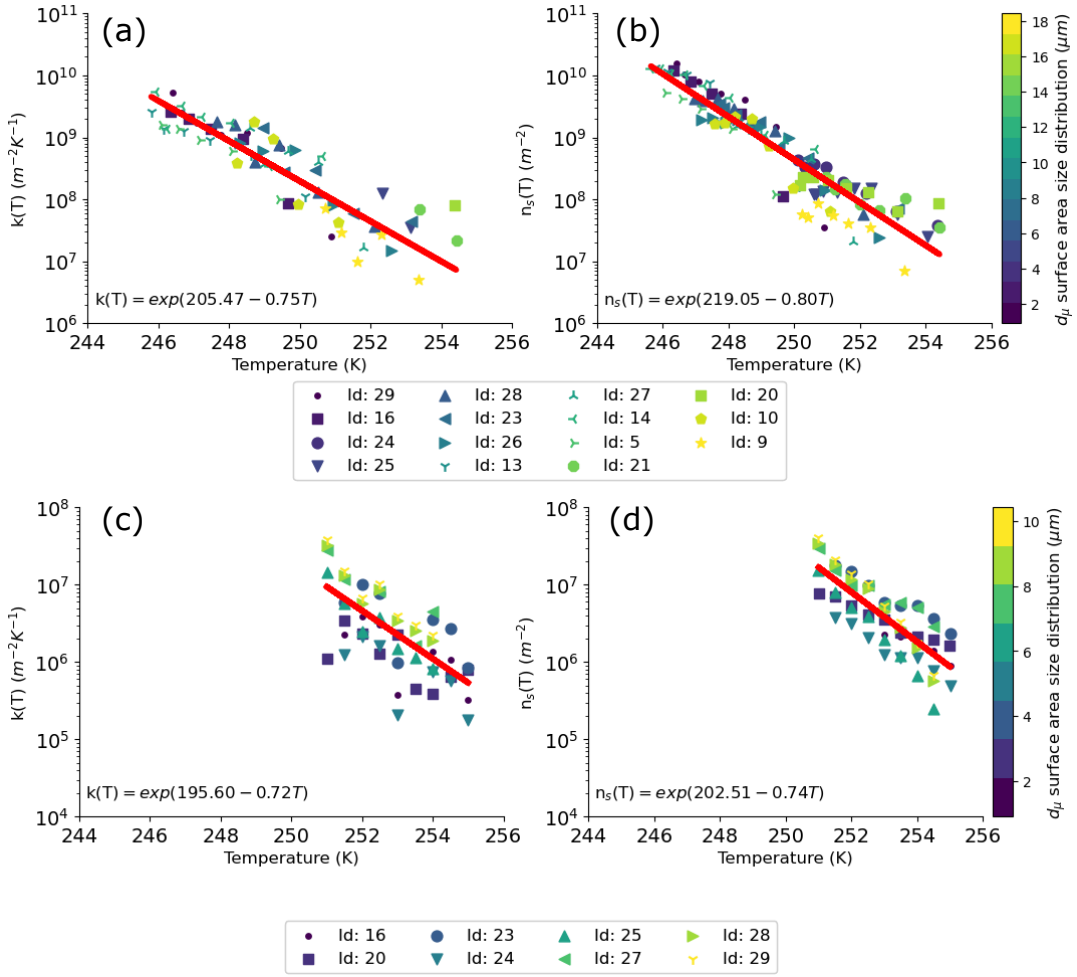


Figure 5.3.: Differential (a,c) and cumulative (b,d) nucleus concentrations obtained for samples from Morocco for AIDA experiments (a,b) and INSEKT experiments (c,d).

displays a larger variation from a linear behavior as the temperature is decreased for the same experiment. This is because $k(T)$ is more sensitive to variations in ice crystal number concentration than $n_s(T)$. While $n_s(T)$ generally increases with each new temperature step due to its cumulative nature, $k(T)$ can increase, decrease, or remain constant, reflecting the dynamic changes in ice nucleation.

When comparing metrics obtained with the same experiment techniques (Fig. 5.3a, b for AIDA and Fig. 5.3c,d for INSEKT) it is notable how similar the slopes of the linear regressions are: 0.75 for $\ln(k(T))$ and 0.80 for $\ln(n_s(T))$ for AIDA, and 0.72 for $\ln(k(T))$ and 0.74 for $\ln(n_s(T))$ for INSEKT. Interestingly, the different size distributions, indicated by their mean diameter, did not have a notable impact on the values obtained for $k(T)$ and $n_s(T)$, i.e. no color gradient is apparent across $k(T)$ or $n_s(T)$ for a given temperature in Fig. 5.3. For example, experiments 9 and 23, which started at similar temperatures, but tested dust aerosol with different mean diameters, presented almost the same behavior and ice nucleation activity.

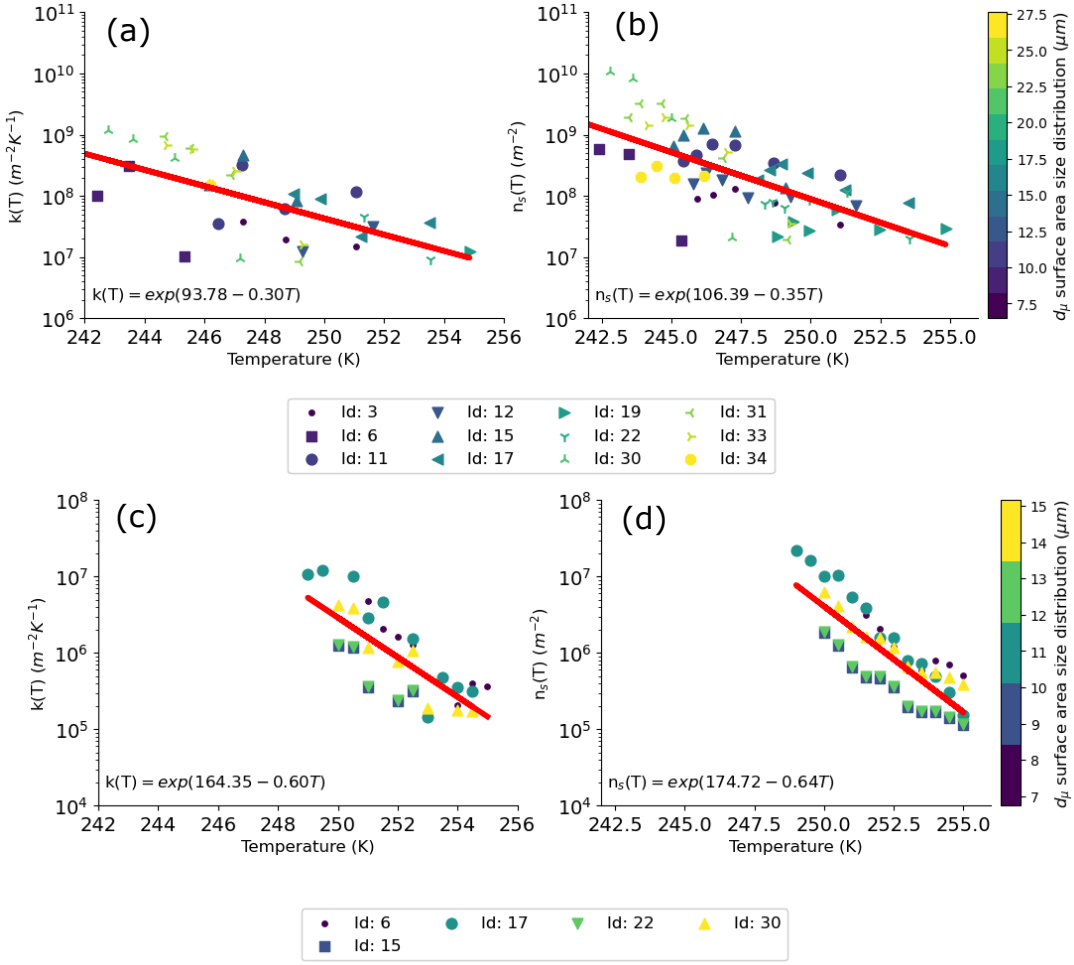


Figure 5.4.: Differential (a,c) and cumulative (b,d) nucleus concentrations obtained for samples from Iceland for AIDA experiments (a,b) and INSEKT experiments (c,d)

Figure 5.4 presents $k(T)$ and $n_s(T)$ obtained from AIDA and INSEKT experiments for Icelandic dust. It can be noticed that the logarithm of the differential nucleus spectrum for AIDA does not present a clear linear increment with the decrease in temperature, but rather a more dispersed behavior around the linear fit.

Whereas $\ln(k(T))$ shows considerable deviation and dispersion around a linear behavior, $n_s(T)$ follows a linear relationship well and with smaller dispersion, particularly for the INSEKT results.

Figure 5.5 combines our results from AIDA and INSEKT and shows INAS densities, $n_s(T)$, for Morocco (Fig. 5.5a) and Iceland (Fig. 5.5b) together with results from previous studies. For the temperature span of AIDA and INSEKT experiments, a notable spread in INAS densities of $\sim$ 1.5 orders of magnitude for Morocco and $\sim$ 2 orders of magnitude for Iceland can be observed. The disagreement between these two techniques is not new, and our results are consistent with previous observations (Hiranuma et al., 2015). Table 5.1 presents the coefficients for the linear regression ($a + bx$, P1) for both dust sources, Morocco and Iceland.

Besides our own experimental results, Fig. 5.5a also shows results from previous studies as a reference. It can be observed that our AIDA results are closer to previous fits for temperatures lower than 250 K, approaching the parameterization proposed by Ullrich et al. (2017), which is also based on AIDA experiments. Compared with Harrison et al. (2019), we obtained lower values for INAS densities from our experiments. However, our results are within the scaled values of 1 % and 20% of Harrison et al. (2019) for K-feldspar.

INAS densities for Iceland (Fig. 5.5b) show a greater spread than those for Morocco: $\sim$ 3 orders of magnitude in the 95 % confidence interval compared to $\sim$ 2 orders of magnitude for Morocco. Similar to our results for Morocco, INSEKT experiments yielded lower INAS densities than AIDA experiments in the temperature range in which they overlapped. The presented AIDA data (slope -0.35, Fig. 5.4b) is closer than the INSEKT data (slope -0.64, Fig. 5.4d) to the parameterization of Sanchez-Marroquin et al. (2020) (slope ≈ -0.46).

As mentioned in Section 4.1.4, experiment IDs 5, 9, and 10 for Morocco, and IDs 12 and 34 for Iceland, exhibited surface area distributions skewed toward larger sizes compared to those obtained using the LD technique. To assess the impact of these experiments on the derived INAS density fits, we performed a sensitivity analysis. This involved computing the INAS fit for Morocco and Iceland (one fit per location) under three different conditions: (1) using all experiments from Morocco and Iceland, (2) excluding the experiments that showed a skewed distribution, and (3) using only the experiments that exhibited a skewed distribution. The fits obtained for each case are shown in Fig. 5.6. For Moroccan fits, the difference between all experiments and the experiments without the skewed size distribution is minimal, while the discrepancy between the case considering all experiments and only the skewed experiments reaches a maximum of approximately 60% at the lowest temperature (around 246 K).

Similarly, Fig. 5.6b presents the $n_s(T)$ fits for Iceland. In this case, the differences among the fits remain below 20%. These results indicate that the influence of experiments with deviating surface area distributions relative to those obtained with the LD technique on the $n_s(T)$ fits does not exceed one order of magnitude. These variations lie within the confidence intervals shown in Figures 5.5a and b for Morocco and Iceland, respectively.

Table 5.1.: Coefficients from lower to higher power and Bayesian information criterion (BIC) for linear regression (P1; $ln(n_s(T)) = a + bT$ where T is temperature in K) for Morocco and Iceland, for the combined results from AIDA and INSEKT (Figure 5.5) measurements.

Dust Source	a	b	BIC
Morocco	291.41	-1.0885	540.3
Iceland	207.85	-0.7657	454.4

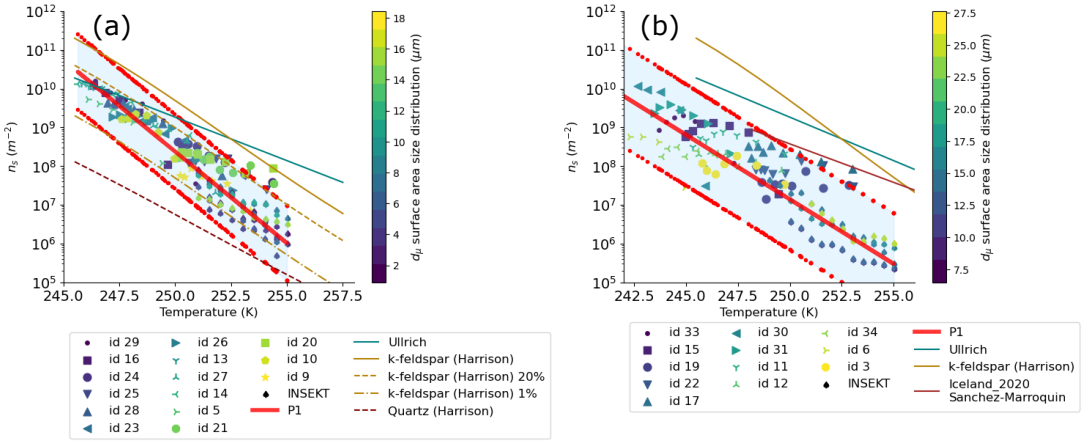


Figure 5.5.: Experimental values of INAS density from AIDA and INSEKT experiments for linear regression (P1) for (a) Morocco and (b) Iceland, Table 5.1 presents the coefficients for the linear regression. Also shown are the parameterizations from Ullrich et al. (2017) denoted as Ullrich, Harrison et al. (2019) denoted as K-feldspar (Harrison), K-feldspar (Harrison) 20%, and K-feldspar (Harrison) 1%, and Sanchez-Marroquin et al. (2020) labeled as Iceland_2020 Sanchez-Marroquin. The blue shaded area represents the 95% confidence interval.

5.1.3. AIDAm

AIDAm allowed us to perform ice nucleation experiments of the samples of interest at a higher temporal frequency than AIDA by repeatedly sampling aerosol from AIDA into a small volume chamber and completing an expansion experiment within 6 minutes. Each of these expansion experiments consists of three steps (Vogel et al., 2022): flush, in which AIDAm is flushed with air and aerosol from AIDA; expansion, in which adiabatic expansion and cooling initiate ice formation; and refill, in which AIDAm is replenished with air from AIDA to reach the same pressure again. This means that consecutive experiments in AIDAm consider evolutions in the aerosol PSD in AIDA, which we expect to contain a decreasing proportion of large particles during the one hour before AIDA expansion. AIDAm experiments thereby offer the opportunity to investigate the impact of changes in the dust PSD on ice nucleation activity. Figure 5.7 shows $n_s(T)$ colored by the expansion relative time to the sample injection (time since the first expansion in AIDAm for a given AIDA experiment) for (a) Morocco and (b) Iceland. It can be seen that for both sample sources the expansions are consistent over time for a period of $\approx$ 5000 s. Additionally, when the experiments were color-coded by mean PSD diameter, no clear trend was observed (not shown). It can also be observed that the values measured with AIDAm differ significantly from those obtained with AIDA (red line in Fig. 5.7a and b). The experiments using AIDAm show a shift of 6 to 7 K compared to AIDA. Vogel et al. (2022) discussed a dependence of the n_s values obtained with AIDAm on the flow rate. However, they found that at expansion flow rates of 10 L min^{-1}, both techniques agreed. It remains unclear whether this is a general trend for all aerosols or specific to the ones considered in the validation of the technique. In the present work, an expansion flow rate of 10 L min^{-1} was used. Therefore, the reasons for the disagreement between the two techniques are not clear, and for this reason, we did not include AIDAm in the calculations to obtain the parameterizations, but

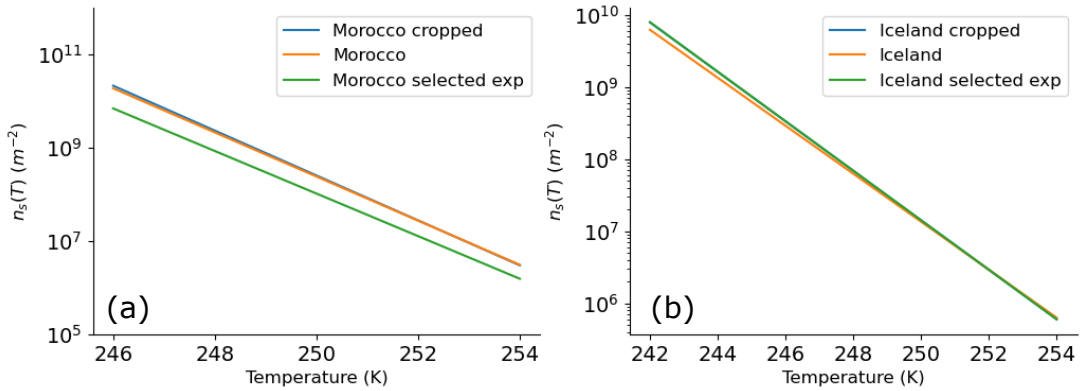


Figure 5.6.: a) INAS density fit computed with all experiments for Morocco (orange line, "Morocco"), not considering experiments IDs 5, 9, 10 (blue line, "Morocco cropped"), and only considering experiment IDs 5, 9, 10 (green line, 'Morocco selected exp'). b) as in a) but for all experiments for Iceland (orange line, "Iceland"), not considering experiment IDs 12, 34 (blue line, "Iceland cropped"), considering only experiment IDs 12, 34 (green line, "Iceland selected exp").

used it only to evaluate the reliability of the experiments over time and the dependence of IN activity on changes in the size distribution.

Additionally, the mean and standard deviation of the measured surface area distribution before expansion in AIDAm for the same experiment ID across different runs is presented in Figures 5.8 and 5.9 for Morocco and Iceland, respectively, along the distributions measured by laser diffraction right after the samples were sieved.

5.2. Modeling results

The following presents the modeling results for the three test cases listed in Table 4.4 for Summer 2021. Unless stated otherwise, all analyses are conducted over Domain 2 (54.8° W–1.89° E; 55.78° N–76.20° N; Sect. 4.2.9). Initially, the model evaluation is presented (Sect. 5.2.1), in which simulated dust aerosol optical depth is compared with AERONET observations and simulated PM_{10} with in situ measurements. Next, using the implemented tagging technique, Icelandic dust emissions and atmospheric concentrations are characterized (Sect. 5.2.2). The sensitivity study exploring the three test cases is then presented (Sect. 5.2.3). Finally, the impacts on mixed-phase cloud properties (Sect. 5.2.4) and the resulting cloud radiative effect (Sect. 5.2.5) are assessed.

It is important to note a limitation identified during the analysis: the current mineral dust emission scheme implemented in ICON-ART (Sect. 4.2.3) tends to underestimate dust emission at high latitudes, as is the case for Iceland. Consequently, although the results presented in this section are internally consistent with what the current version of ICON-ART produces, they likely underestimate the true INP burden from Icelandic dust, and the conclusions drawn here may change once the emission scheme is improved and calibrated against in situ measurements. Improving and calibrating high-latitude dust emissions is, however, beyond the scope of this work, whose main goal is instead to assess the change in INP influence

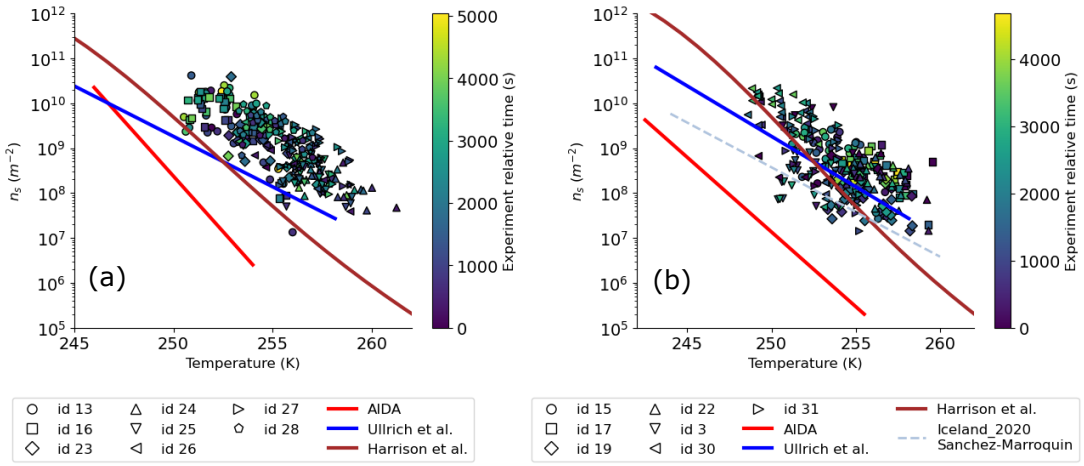


Figure 5.7.: INAS density for AIDAm experiments. Symbol color refers to the time at which AIDAm experiment is performed relative to the first expansion in AIDAm for each injection in AIDA. a) for Moroccan samples, AIDA is the fit developed with AIDA experiments for Morocco. b) for Icelandic samples, AIDA is the fit obtained with AIDA experiments for our Icelandic samples. In addition, relevant parameterizations from other authors are considered: Harrison et al (Harrison et al., 2019) is the fit for k-feldspar, Ullrich et al (Ullrich et al., 2017) and Iceland_2020 Sanchez-Marroquin (Sanchez-Marroquin et al., 2020).

from high-latitude dust sources when a source-specific INP parameterization is considered (Sect. 5.2.3). Nevertheless, this is an important finding, as it draws attention to a current and underexplored limitation of the model and highlights an opportunity to improve the dust emission scheme in future work.

5.2.1. Model evaluation

We evaluated simulated dust using dust aerosol optical depth (DAOD) because it provides a rigorous, column-integrated constraint directly tied to the model dust burden and optical properties. We compared model DAOD with AERONET observations at 551nm. Figure 5.10a shows the monthly mean for summer for each station calculated using the approach described in Sect. 4.3. On average, the simulated and observed DAOD agree within a factor of about two (blue dashed lines in Fig. 5.10a) with a correlation coefficient of 0.74.

To investigate the model performance at finer temporal resolution, I compared 2-hourly DAOD data for summer 2021 (Fig. 5.10b). In this case, the correlation decreased to 0.43, with a clear bias in the simulated values, particularly when observed DAOD is below 0.3, and with no apparent dependence on the time of year during summer (color scale in the figure). Figures 5.10c and d show the percentage of modeled DAOD values that are, respectively, more than twice as high or less than half of the observed DAOD. The model tended to overestimate DAOD at Dakar more than half of the time (Fig. 5.10c), a site along the West African dust outflow corridor. In contrast, it underestimated DAOD at Saada, Cerro Poyos, and NEONUKFS more than half of the time (Fig. 5.10d): Saada is a near-source North African site, Cerro Poyos (southern Iberia) lies in a downwind receptor/edge of plume region, and NEONUKFS is located in central North America, far from major dust sources and sampling long-range, diluted plumes. The JJA

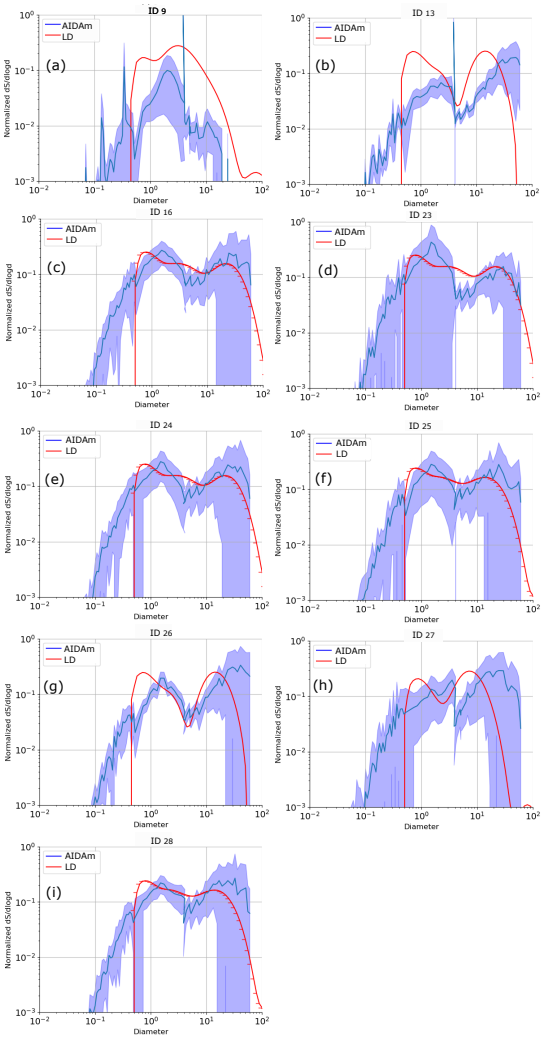


Figure 5.8.: Normalized surface area distribution for AIDAm experiments for Moroccan samples. The blue line represents the mean value, while the blue shading indicates the standard deviation across all expansions of the same sample, as measured by AIDAm sensors before expansion (SMPS, APS, and OPC). The red line represents measurements obtained using the laser diffraction (LD) technique on the freshly sieved sample.

mean simulated DAOD together with the location of the AERONET stations is shown in Fig. 5.10e. Stations with the largest model biases are generally located near the coast, where underestimation is more frequent (e.g., Saada and Cerro Poyos), likely reflecting a significant contribution of sea salt to the measured AOD. Overall, the model reproduced the monthly mean DAOD reasonably well at most stations, but tended to underestimate values at coastal AERONET sites probably due to the contribution of sea salt at those sites, which cannot be included in a dust-only simulation. Additionally, stations located closer to major dust sources such as Banizoumbou and Dushanbe showed good agreement. It is important to emphasize that this validation approach focuses on capturing the main DAOD behavior at each location, averaged over time. Thus, we conclude that the model reproduced the monthly-mean DAOD well, while the hourly underestimations likely arise from non-dust aerosol contributions in the observations that are not included in the simulation.

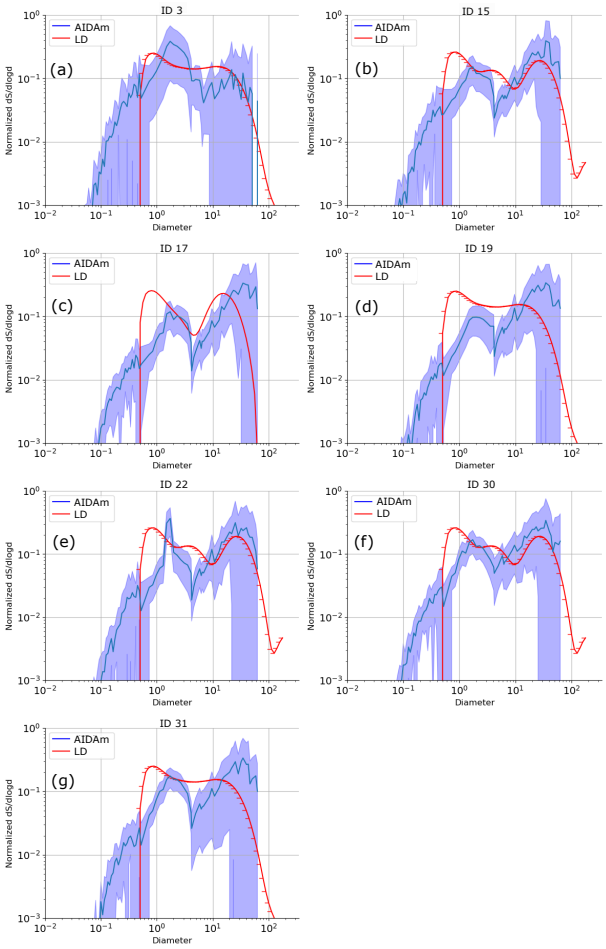


Figure 5.9.: Normalized surface area distribution for AIDAm experiments for Icelandic samples. The blue line represents the mean value, while the blue shading indicates the standard deviation across all expansions of the same sample, as measured by AIDAm sensors before expansion (SMPS, APS, and OPC). The red line represents measurements obtained using the laser diffraction (LD) technique on the freshly sieved sample.

Given that this study centers on the INA of Icelandic mineral dust in the immersion-freezing mode, it is relevant to validate the simulated dust concentrations over Iceland. However, AERONET data cannot be used for this purpose as there are no data for summer 2021. For this reason, we compared measured PM_{10} mineral dust concentrations at Mýrar, Iceland (63°30′27.4″ N, 18°19′45.2″ W) from the HiLDA measurement station (TU Darmstadt, Department of Geoinformation Science, 2025). These data were provided by research partners. Figure 5.11a shows the 2-hourly mean time series from June to August 2021 for both observed (black dots) and simulated (red dots) concentrations. Both datasets exhibited sporadic peaks in PM_{10} dust concentrations, consistent with previous studies that described Icelandic dust emissions as highly localized in time and space (Meinander et al., 2022; Cvetkovic et al., 2022). However, the timing of the peaks presented a modest agreement: in June and July 2021, observed PM_{10} peaks occurred earlier than those in the simulations. Figure 5.11b presents the scatter plot of simulated versus observed 2-hourly PM_{10} concentrations, colored by date. Simulated values are frequently more than an order of magnitude lower than the observations, particularly during the first two months of summer

2021. Figure 5.11c shows the weekly averaged time series, and Fig. 5.11d compares the corresponding simulated and observed values. These plots indicate that the largest discrepancies occur in the second and third weeks of June and the first week of July, when simulated concentrations are consistently more than ten times lower than those observed.

The average simulated Icelandic dust emission for summer 2021 is shown in Fig. 5.12, together with the main emission hotspots identified by Arnalds et al. (2016). The simulations indicate low emissions at most hotspots, with the exception of Mýrdalssandur, Skeiðarársandur, and Hagavatn. A comparison with the results of Meinander et al. (2022), who used the SILAM model (Sofiev et al., 2015) at 0.1×0.1° resolution (approximately 5 km E–W and 11 km N–S, whereas our grid resolution is about 10 km) for the same period of time, shows notable differences. SILAM highlights the areas between Dyngjusandur and Vonarskarð, as well as the region near Flosaskarað, as major emission sources, while in our simulations only Flosaskarað showed moderate emissions, with the main hotspots located at Mýrdalssandur and Skeiðarársandur. It remains unclear whether these discrepancies arise from differences in grid resolution, soil properties, or other factors. Further studies are therefore needed to better characterize and understand Icelandic dust emissions. However, the main goal of this study is to assess the sensitivity of cloud properties to the new parameterizations (derived from the experimental results; Sect. 5.1.2). For this purpose, discrepancies in the timing of dust events relative to other studies or observations do not severely limit our analysis.

5.2.2. Characterization of atmospheric Icelandic dust

An important question regarding the effects of different parameterizations on MPC properties is the extent to which Icelandic dust is transported, and over which horizontal and vertical regions it has a significant presence, as this is fundamental for quantifying its ice-nucleating activity in immersion freezing. Figures 5.13a, d, and g show the zonal mean atmospheric dust concentration together with the planetary boundary layer (PBL) height for domain 2 for June, July, and August, respectively. It can be observed that in June and July, most of the emitted Icelandic dust remains within the PBL. These months are also characterized by lower mean atmospheric dust concentrations compared to August. In contrast, August shows more intense emissions, with a vertical distribution that extends above the PBL and reaches pressure levels near 750 hPa (approximately 2–2.8 km). Notably, the zonal mean indicates that most Icelandic dust does not reach atmospheric temperatures colder than –10 °C.

Figures 5.13b, e, and h show the mean dust column burden (DCB) distribution for June, July, and August, respectively. For June and July, most of the emitted Icelandic dust remains near the source region. In contrast, during August (Fig. 5.13h), Icelandic dust was transported over greater distances, forming a distinct ‘bird-like’ pattern, with one plume extending northward and another towards the United Kingdom. This agrees with the zonal mean results, which indicate that in August the Icelandic dust reaches altitudes above the PBL, making long-range transport more likely. In all months, the highest dust concentrations are located near the Icelandic coast, with the maximum shifting from the Mýrdalssandur region

(in the south of the island) in July to areas near Hagavatn and Flosaskarað (in the northwest of Iceland) in August.

Figures 5.13c, f, and i (left y-axis, blue bars) show the frequency of the DCB magnitude in different bins for June, July, and August, respectively. A common pattern across the months can be observed, in which concentrations lower than $2.3 \cdot 10^{-3}$ g m^{-2} follow a similar frequency distribution, possibly indicating a constant and low emission of Icelandic dust through time. For July (Fig. 5.13f), a higher DCB value with low frequency is found (at $4.1 \cdot 10^{-3}$ g m^{-2}), possibly reflecting intense but localized emission activity. For August (Fig. 5.13i), higher and more frequent DCB concentrations are present. Despite the frequency distribution being skewed toward larger concentrations from June to August, the total DCB, calculated as the sum of the DCB from Icelandic dust, reaches similar values across all months (Figs. 5.13c, f, and i; red line, right y-axis).

5.2.3. Sensitivity study including newly developed INAS density parameterizations

This section analyzes total INP concentrations evaluated at the local ambient temperature (i.e., the temperature at each space–time point). All cases apply the same immersion-freezing thresholds: -38° C $\leq$ T $\leq$-6° C and supersaturation conditions (rh$\geq$100%). Figure 5.14 presents the INP column burden (INP contribution from multiple nucleation pathways and from all sources along the atmospheric column) for June, July, and August 2021 (rows) for the study cases listed in Table 4.4, i.e., Default, LLD_HLD, and LLD_SHLD (columns). The Default case (first column in Fig. 5.14) shows higher INP concentrations over the south of Iceland (Mýrdalssandur and Skeiðarársandur) in June and July (Figs. 5.14a and d), and over the central region (Hagavatn and Flosaskarað) in August (Fig. 5.14g). The higher INP concentrations are located between 65° N and 62.5° N in all months for the Default case. In addition to the INP column burden over Iceland, there is also a considerable contribution along the east coast of Greenland in all months. Over the ocean, elevated INP levels are more spatially sparse than in land. INP concentrations obtained when using dedicated parameterizations for low- and high-latitude dust sources are shown in Fig. 5.14b, e, and h (case LLD_HLD). It is relevant to remember that low-latitude dust samples correspond to Morocco, and high-latitude dust samples to Iceland. The use of the new parameterizations leads to a reduction in the INP column burden in regions where the highest values were found in the default case. For June (Fig. 5.14b), the INP hotspot located between M'yrdalssandur and Skeiðar'arsandur almost disappears. Additionally, a considerable reduction in INP column burden is observed over the Greenland coast and ocean. Similarly, the values for July with the LLD_HLD case show a strong reduction in the INP column burden, especially at latitudes higher than 70° N and over Greenland, when compared with the Default case. In contrast to this reduction, a more uniform and enhanced INP burden appears over Iceland, which was not present in the default case. In the same fashion, August (Fig. 5.14h) shows smaller values of column burden than the default case at specific locations, but with a more even spatial distribution. This feature is particularly evident over the ocean and Iceland. The default case is characterized by a high and localized INP column burden in the south-west and central parts of the

island (Hagavatn and Flosaskarað), with smaller concentrations toward higher latitudes. In contrast, in the LLD_HLD case this hotspot disappears, while both Iceland and higher latitudes exhibit a more widespread INP column burden. Figures 5.14c, f, and i show the LLD_SHLD case. This case uses the same low-latitude dust parameterization as the LLD_HLD case, but differs in the HLD parameterization by considering that not all particle sizes contribute equally to INP production; instead, their contribution depends on the mineralogical content of pyroxene associated with each size (Sec. 6.1.4). When contrasting the two experiments, LLD_HLD and LLD_SHLD, it is clear that the INP column burden over Iceland is further decreased in the LLD_SHLD case across all months. Conversely, there is an increase in the INP column burden over Greenland, although still showing a more even spatial distribution than in the default case (cf. Fig. 5.14d for default and Fig. 5.14f for LLD_SHLD). However, a different situation is observed in June for the LLD_SHLD case (Fig. 5.14c), where both Iceland and Greenland exhibit a reduction in INP column burden compared to the LLD_HLD case (Fig. 5.14b).

In Figure 5.15, the result of different parameterizations for the zonal-mean total atmospheric INP concentration are shown; the zonal mean was computed including only space–time points with nonzero INP concentrations. For this case, the analysis is restricted to the region 61° N $<$ lat $< 69^\circ$ N, where Icelandic dust makes its most significant contribution to INP concentrations (see Fig. 5.14, outside this region the Icelandic dust contribution to INP is several orders of magnitude lower). It is worth noting that the same zonal averages were also performed for the full domain shown in the previous plots, with little difference in the results. In the default case (Fig. 5.15, first column), INPs are present above 800 hPa over the entire latitude range, with concentrations below 0.1 m^{-3}. Furthermore, in all figures associated to the default case (Figs. 5.15a, d, g), INP concentrations increase above 600 hPa. Higher values occur in June (Fig. 5.15a) and August (Fig. 5.15g) at 700–900 hPa, up to an order of magnitude larger than in July (Fig. 5.15d). Additionally, in June and August the -6°C isotherm is located near 700 hPa, while in July it occurs higher, around 630 hPa and the relative humidity above 85% (black dots) remains confined below 900 hPa. These two conditions are critical since immersion-freezing parameterizations require $T < -6$°C and supersaturation with respect to water in the implementation in ICON. The second column of Fig. 5.15 shows the INP zonal averages for the LLD_HLD case. For nearly all latitudes, INP concentrations above 600 hPa (Figs. 5.15b, h) and 550 hPa (Fig. 5.15e) remain below 10^{-2} m^{-3}. At lower pressures, INP concentrations also decrease. For example, in the default case for June (Fig. 5.15a), concentrations between 400–500 hPa across almost all latitudes ranged from 10^2 to 10^3 m^{-3}. In contrast, for the same month in the LLD_HLD case (Fig. 5.15b), values are reduced to 10^0–10^1 m^{-3}. Notably, in all LLD_HLD panels the relative humidity exceeding 85% reaches higher altitudes (lower pressures) than in the default case (cf. Figs. 5.15d, e). The difference in the INP zonal averages for the LLD_SHLD case (third column in Fig. 5.15), compared with the LLD_HLD case, lies in the further reduction of INP concentrations near 600 hPa and in a subtle change of the vertical distribution below this level. For example, in the LLD_HLD case (Fig. 5.15e) a high INP concentration is observed between 300–400 hPa, which

is absent in the LLD_SHLD case (Fig. 5.15f). Conversely, in Fig. 5.15f, elevated INP concentrations appear between 200–300 hPa, whereas for the same pressure range they are lower in Fig. 5.15e.
Focus is now placed on the behavior of the three test cases (default, LLD_HLD, LLD_SHLD) on instantaneous INP concentrations in immersion-freezing mode. Figure 5.16 reports the total Icelandic INP share ($T_{\mathrm{INP,iceland}}$), defined at each grid point as $T_{\mathrm{INP,iceland}}/(T_{\mathrm{INP,iceland}} + T_{\mathrm{INP,elsewhere}})$) for concentrations larger than 10^{-3} m^{-3}. The objective is to quantify how much of the total INP production in immersion-freezing mode comes from Icelandic dust and how much from dust from elsewhere. Overall, it can be observed that the Icelandic INP share does not exceed 3% when aggregated over pressure levels (total INP computed over latitude-longitude and time; Fig. 5.16, first column: a, c, e), and does not exceed 5% when aggregated over time (total INP computed over latitude-longitude and height, and daily averaged; Fig. 5.16, second column: b, d, f). Additionally, for nearly all pressure levels and dates, the default case shows the largest and most frequent INP contribution relative to LLD_HLD and LLD_SHLD throughout all months. For instance, the Icelandic INP share approaches 2% near 800 hPa for the default case, whereas LLD_HLD and LLD_SHLD show negligible Icelandic shares at comparable pressures. Below 600 hPa, LLD_SHLD presents Icelandic shares similar to the default case, while LLD_HLD remains substantially lower (Fig. 5.16a). Similarly, the daily-averaged total Icelandic INP share shows the same pattern: the default case exhibits more days with Icelandic contributions, with maximum values reaching 5%, followed by LLD_SHLD, which shows lower Icelandic shares (Fig. 5.16b). For July (Fig. 5.16, second row), the maximum Icelandic INP share shifts to lower pressure levels compared with June (from $\approx$ 800 hPa to $\approx$ 600 hPa; Fig. 5.16c) and exceeds 2%. Furthermore, the LLD_HLD case shows more frequent and larger contributions than in June, and at higher pressure levels than the LLD_SHLD case. This behavior is consistent with Fig. 5.13b, which indicates that more Icelandic dust reached lower pressure levels than in June. The daily-averaged Icelandic INP share exhibits a pattern similar to June: the default case shows the highest and most frequent Icelandic shares, followed by LLD_SHLD, with the difference that there are more days with Icelandic contributions in July (Fig. 5.16d) for both the default and LLD_SHLD cases. For August, the default case continues to show the most frequent Icelandic INP share across pressure levels, mainly between 800 hPa and 450 hPa, but the LLD_HLD case now shows the larger Icelandic contribution at 350hPa with $\approx$ 2%, followed by the LLD_SHLD case at a similar pressure level and magnitude (Fig. 5.16e). This month also showed most Icelandic dust above the PBL height (Fig. 5.13g). A similar behavior is presented in the daily-averaged Icelandic INP share: the LLD_HLD case shows the largest value, and its daily frequency increased compared with the other months (Fig. 5.16e,f). For the default case, the number of days with Icelandic INP contributions was similar to June (20 days in both months; June and August), the LLD_HLD case presents the lower contribution among cases with 3 days for June, 2 days in July and 7 days in August; and the LLD_SHLD case shows a similar number of days with Icelandic INP shares across months (5 for June, 6 for July, and 5 for August).

5.2.4. Effect on mixed-phase cloud properties

Let's now focus on the effects that the consideration of the different parameterizations, default, LLD_-HLD, and LLD_SHLD cases have on cloud properties such as MPC occurrence, cloud-phase, rain rate, effective radius of liquid water, and snow rate. Cloud phase and occurrence were defined in Sect. 4.2.7. Additionally, rain rate indicates the efficiency of warm-rain processes (autoconversion; cloud water is converted into rain droplets, and accretion; existing raindrops grow larger by collecting smaller cloud droplets as they fall) and, below 0° C, the melting contribution from ice-phase hydrometeors. Snow rate tracks solid-phase precipitation production and reflects glaciation strength (the transition from super-cooled liquid water to ice). The liquid effective radius r^{w}_{eff} depends on droplet number and liquid water content and helps diagnose shifts between warm-rain and ice-dominated regimes (Yang et al., 2021; Ramadoss et al., 2024). In cases with higher INP concentrations, ice forms earlier and more abundantly, and the WBF process intensifies (vapor deposits onto ice while droplet liquid water is reduced to supply that vapor; Sect. 3.4). As a consequence, r^{w}_{eff} and the rain rate generally decrease. Conversely, lower INP concentrations delay glaciation, allowing supercooled liquid to persist; autoconversion/accretion strengthen, so rain rate and r^{w}_{eff} tend to increase. Interpretation of these diagnostics (rain rate, snow rate, and r^{w}_{eff}) is non-trivial, because they are affected indirectly by INPs and can be modulated by updraft strength, cloud depth, and environmental humidity (Korolev et al., 2017; Field et al., 2017). Nevertheless, when analyzed together with cloud phase and MPC occurrence, they provide a complementary view of how INPs influence cloud properties and processes. In Fig. 5.17 first row, all parameterizations exhibit a similar shape in MPC occurrence (dashed lines corresponding to upper x-axis), resembling a unimodal distribution with the maximum generally between 650-750 hPa and always below 15% in occurrence. In June, the default case shows a maximum MPC occurrence of $\approx$ 10% at $\approx$ 770 hPa (Fig. 5.17a). In July, the LLD_HLD case presents the largest peak ($\approx$ 14%) at a pressure level similar to June (Fig. 5.17b). For this month, the default parameterization departs from the unimodal pattern and exhibits three local maxima between 600-900 hPa. In August, the LLD_HLD case again yields the largest MPC occurrence, with the peak shifted toward 800 hPa. Across pressure levels, the LLD_HLD parameterization produces MPC occurrence comparable to the default case (Fig. 5.17a) or larger values (more than twice as large in July; Fig. 5.17b). In contrast, the LLD_SHLD case shows no consistent trend: it can be smaller than the default case above $\approx$ 600 hPa (June; Fig. 5.17a), larger than the default case at almost all levels (July; Fig. 5.17b), or only slightly different from the default case (August; Fig. 5.17c). Throughout all months, differences in MPC cover between parameterizations remain below 10%; profiles can be very similar (June; Fig. 5.17a) or show more pronounced differences (July and August; Fig. 5.17b,c). At the pressure levels of peak MPC occurrence, the MPC cover is $\approx$ 70% in June (Fig. 5.17a) and $\approx$ 75% in July and August (Fig. 5.17b,c).

The vertical structure of MPC cover exhibits two distinct peaks near 900 hPa and 700 hPa for all cases in June (Fig. 5.17a). In July, this double-peak pattern appears only in the default case, whereas LLD_HLD

and LLD_SHLD show a smoother profile over the same pressure range (Fig. 5.17b). In August, LLD_-HLD and LLD_SHLD display two peaks above 600 hPa, while the default case shows three consecutive peaks (Fig. 5.17c). The cloud phase for June, July, and August (second row of Fig. 5.17) exhibits a consistent vertical structure in all three months, a maximum near 980 hPa (larger ice presence), followed by a minimum around 850 hPa (larger liquid water presence), and then a gradual increase toward lower pressures, up to 300 hPa (the upper limit of MPC occurrence). Variability between months is small, the phase minimum occurs at comparable pressure levels (between 800–900 hPa), and the cloud phase generally remains within 35–45%. Likewise, the upper-level maximum is similar across months, reaching 80% near 300 hPa. Different parameterizations present similar cloud-phase shapes and values, with differences in the cloud phase smaller than 5% across pressure levels. For instance, in June (Fig. 5.17d) the default and LLD_SHLD cases present a similar curve for pressures higher than 750 hPa, while LLD_-HLD presents a shift toward larger cloud-phase values. However, for pressures lower than 750 hPa, the LLD_HLD and LLD_SHLD cases now agree more with each other, presenting larger values of cloud phase than the default case. On the contrary, for July (Fig. 5.17e) it is the LLD_HLD and LLD_SHLD cases that agree for pressure levels higher than 750 hPa, but below that level all cases present different values. Finally, in August (Fig. 5.17f) all curves present different cloud-phase values for pressures larger than 800 hPa and tend to diverge less at lower pressures. Let's focus now on how the different study cases affect the rain rate, effective radius of liquid water and snow rate inside MPCs. The first column of Fig. 5.18 presents the rain rate for June, July, and August for the three study cases. Figure 5.18a,d,g show that the rain rate is larger for most cases at higher pressure levels. Additionally, for all months and study cases, the mean monthly rain rate is always lower than 10^{-7} kg m^{-2} s^{-1}. For June (Fig. 5.18a), the default and LLD_HLD cases present similar behavior for pressures up to 700 hPa. In this same range, the LLD_SHLD case presents lower rain rates. For pressures lower than 700 hPa, there is an increase in the rain rate. This increase occurs at a different pressure level for each case, but all of them follow the same shape. For July (Fig. 5.18d), all cases present different rain rates for pressures higher than 900 hPa, with the default largest in magnitude, followed by LLD_SHLD and LLD_HLD, respectively. For pressures between 750-900 hPa, all cases follow a similar curve. It is for pressures lower than 750 hPa that LLD_SHLD shows a larger rain rate than the other cases. Additionally, LLD_HLD shows a peak in the rain rate between 450-610 hPa that is not present in the other cases. For August (Fig. 5.18g), all cases agree for pressures lower than 800 hPa, and for higher pressures LLD_HLD presents the larger rain rate, followed by LLD_SHLD. The second column in Fig. 5.18 presents the effective radius of liquid water for the months of June, July, and August. It is apparent that all months and cases follow similar shapes, with minimal differences above 800 hPa. There is no common trend across months regarding which case presents larger or smaller effective liquid-water radius. For June (Fig. 5.18b), the default and LLD_HLD cases present curves whose differences at any pressure level are smaller than 0.1 μm, while LLD_SHLD can present larger values, up to 0.5 μm, for pressure levels lower than 700 hPa. Similarly, for August (Fig. 5.18h), all cases present similar values, with the largest differences in the effective liquid-water

radius (about ≈ 0.5 µm) in the pressure range between 500 and 800 hPa. It is for July (Fig. 5.18e) that the largest differences are found; again, between 500 and 800 hPa, differences can be as large as 1 µm (e.g., at 700 hPa between the default and LLD_HLD cases). The snow rates presented in the third column of Fig. 5.18 for June (c), July (f), and August (i) indicate that no clear trend is observed regarding which case presents smaller or larger values across pressure levels for all months. Snow rates are larger than rain rates by roughly two orders of magnitude at their maximum values (about 10^{-5} versus 10^{-7} kg m^{-2} s^{-1} for snow and rain, respectively). It is also notable that, for all cases, each month retains the same general shape; the main differences arise from shifts in peak location or changes in peak magnitude. For June (Fig. 5.18c), the two peaks seen in the default case are also present for LLD_HLD and LLD_SHLD, with the first peak shifting from 900 hPa (default) to $\approx$ 800 hPa (LLD_HLD and LLD_SHLD). The second peak near $\approx$500 hPa is likewise present for LLD_HLD and LLD_SHLD, but it is smaller for LLD_HLD and larger for LLD_SHLD. Similarly, August (Fig. 5.18i) shows a shape comparable to June, characterized by two peaks, although inter-case differences are weaker: the default case generally exhibits smaller snow rates at several pressure levels than LLD_HLD and LLD_SHLD, which agree more closely with each other. In contrast, July (Fig. 5.18f) lacks the two-peak structure; the lower-level peak around 800-900 hPa apparent in June and August appears suppressed and is noticeable only for LLD_HLD.

5.2.5. Cloud radiative effect

Let's focus now on how the different study cases affect the CRE. Figure 5.19 presents the net, SW, and LW CRE (columns) for JJA (rows) for all cases considered in this study and for CERES (Sect. 5.2.5). It can be seen that the differences between cases are lower than 10% for all months and metrics (net, SW, LW). Additionally, there is no common month-to-month trend among cases regarding which produces a higher or lower net or SW CRE. It can also be observed that both net and SW CRE present a similar pattern. For June (Fig. 5.19, first row), the default case produces the largest net and SW CRE, followed by LLD_HLD and LLD_SHLD (Fig. 5.19a,b). In contrast, for July (Fig. 5.19d,e) the LLD_SHLD case produces the largest net and SW CRE, followed by the default case. A pattern similar to June is found for August, in which the largest net and SW CRE are obtained with the default case, followed by the LLD_HLD case (Fig. 5.19g,h). Contrary to the SW CRE, there is a month-to-month trend for the LW CRE (Fig. 5.19, third column), in which the LLD_HLD case presents the largest values followed by LLD_SHLD case.

In comparison with CERES, the LW CRE shows the largest discrepancies, absolute relative errors of 30% or more, and is consistently underestimated (Fig. 5.19 third column, pink bars). By contrast, SW CRE differences are smaller, peaking near 15% (default case in June and August; Figs. 5.19b,h), and they tend to overestimate CERES. Across both SW and LW, either LLD_HLD or LLD_SHLD (often both) provides the closest agreement with CERES. For instance, the default case yields a 7.1% absolute relative error for the net CRE (Fig. 5.19a). This absolute relative error is much smaller for LLD_HLD

and LLD_SHLD, at 2.1% and 1.2%, respectively. A similar reduction is found for the SW and LW components (Figs. 5.19b,c): LLD_HLD and LLD_SHLD yield comparable values in both SW and LW, whereas the default case shows a larger absolute relative error, with larger SW and lower LW CRE than CERES. For July, the default and LLD_HLD cases show net CRE values smaller than the CERES estimate, whereas LLD_SHLD is larger and has the lowest absolute relative error (0.7%), followed by the default case (6.3%; Fig. 5.19d). The SW and LW components show a different pattern for the same month: the smallest absolute relative errors occur for LLD_HLD, with 0.6% in SW (Fig. 5.19e) and 30.5% in LW (Fig. 5.19f). Across all cases for July, the LW CRE is underestimated; for SW, only LLD_-HLD underestimates, while the other cases overestimate. For August, the lowest absolute relative error in the net CRE is found for LLD_HLD (0.6%), followed by the default case (1.3%), and then LLD_-SHLD (13%), which is the only case that underestimates the net CRE (Fig. 5.19g). For the SW CRE, the smallest relative error occurs for LLD_SHLD (4%), followed by LLD_HLD (13%); in this case, all different cases of study overestimate the SW CRE (Fig. 5.19h). For the LW CRE, the lowest absolute relative error is obtained with LLD_HLD, followed by LLD_SHLD (41.6% and 43.1%, respectively; Fig. 5.19i).

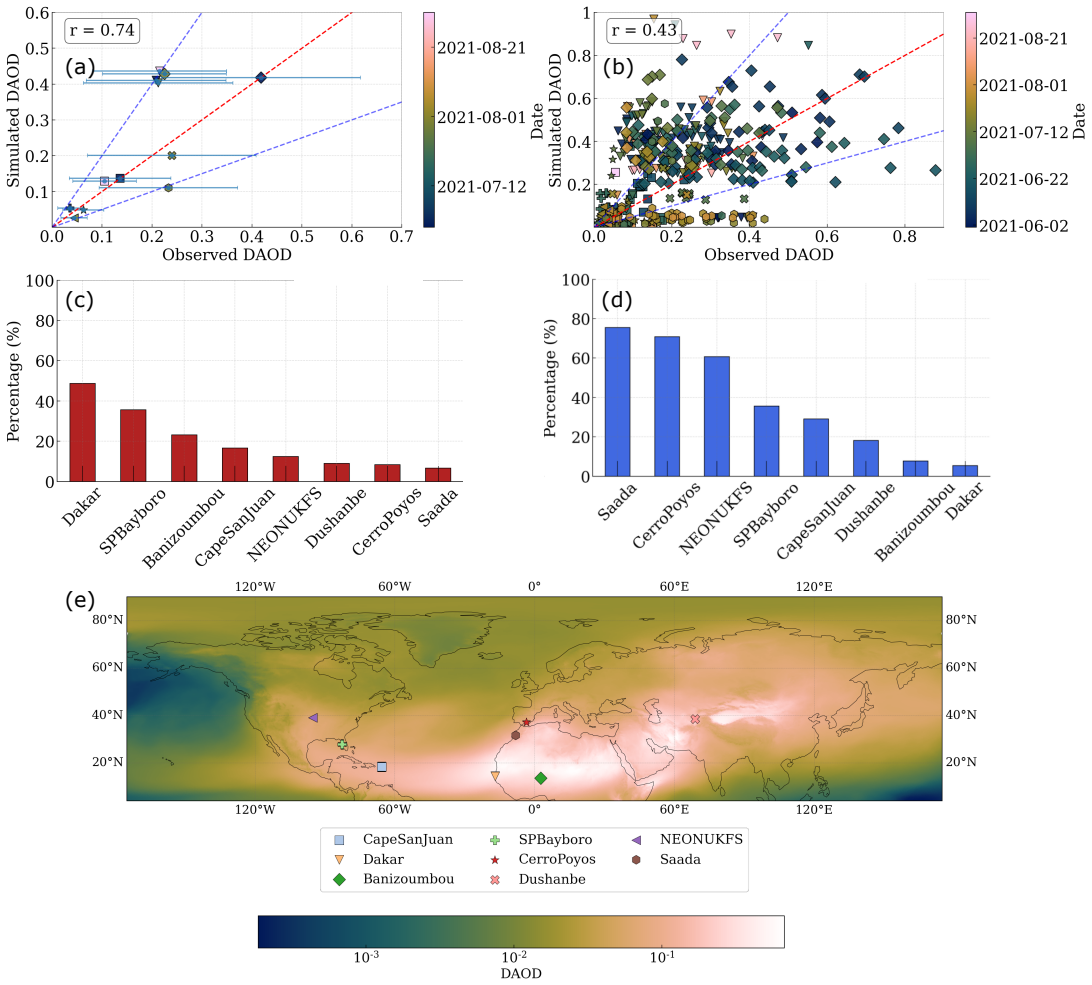


Figure 5.10.: Observed (AERONET stations, obtained with approach described in Sect. 4.3) and simulated DAOD with correlation coefficient (r): (a) monthly mean at each station (locations shown in panel e) for summer 2021, horizontal error bars represent the interquartile range (IQR), defined as half the distance between the 25th and 75th percentiles, (b) 2-hourly data for all stations (locations shown in panel e) during summer 2021, with symbols colored by date. The dashed red line indicates the 1:1 relationship, and the dashed blue lines indicate a factor of 2 bias. (c) percentage of simulated DAOD values exceeding the observed values by a factor of 2, and (d) percentage of simulated DAOD values more than two times lower than observed, both based on 2-hourly data. Panel (e) shows the mean simulated DAOD for summer and the station locations used in panels (a)–(d).

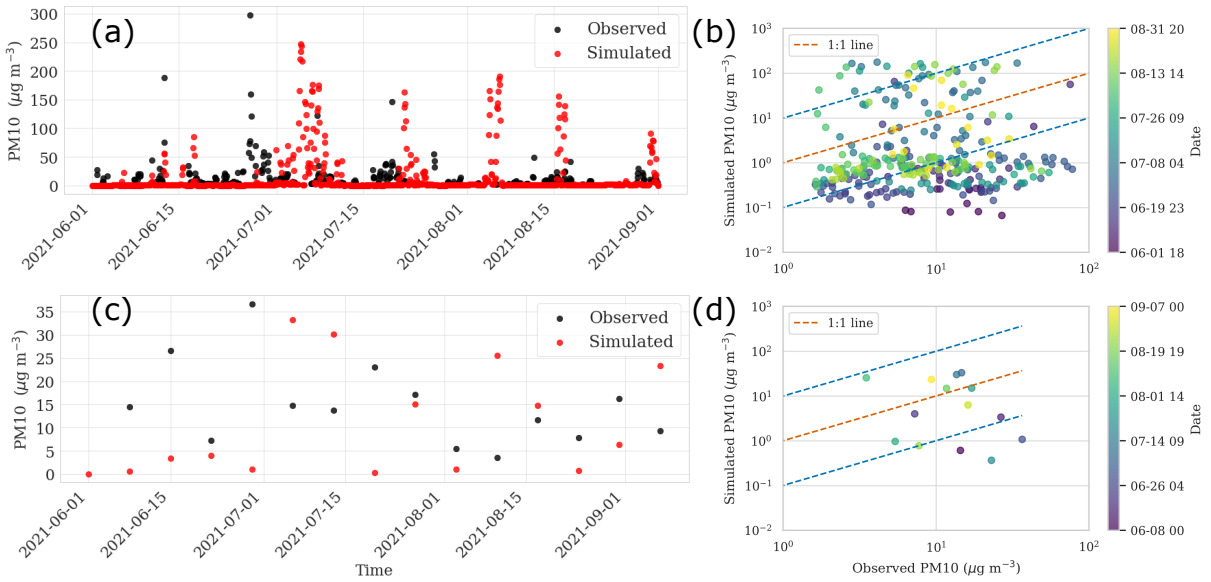


Figure 5.11.: Simulated and observed PM_{10} dust concentrations at Mýrar, Iceland (63°30′27.4″ N, 18°19′45.2″ W) during summer 2021. Panels (a) and (c) show 2-hourly and weekly mean time series of the measurements, respectively, while panels (b) and (d) present the corresponding simulated and observed values. Blue dashed lines are 10 times bias.

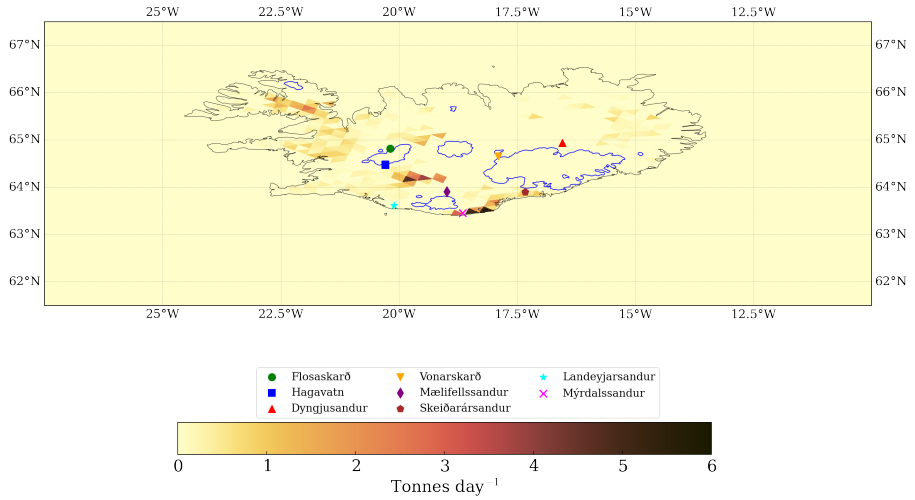


Figure 5.12.: Summer 2021 average simulated Icelandic dust emissions (tonnes day^{-1}). Markers denote emission hotspots identified by Arnalds et al. (2016).

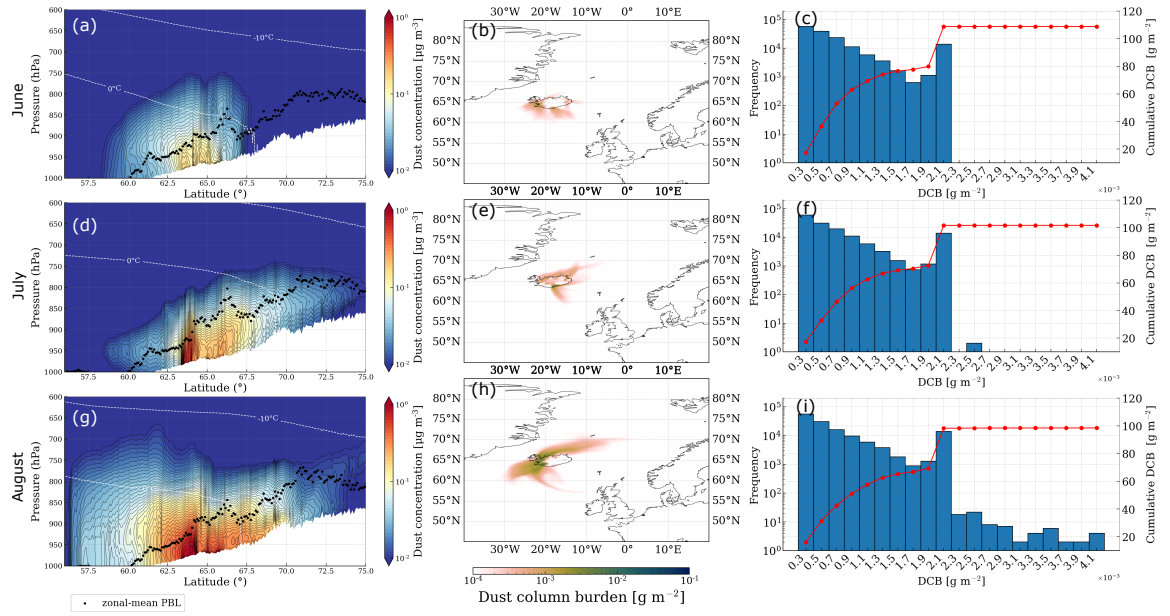


Figure 5.13.: Zonal mean atmospheric dust concentration and planetary boundary layer height (PBL; a, d, g), monthly mean dust column burden (DCB; b, e, h), and DCB frequency distribution (blue bars) with cumulative DCB across bins (red line, right y-axis; c, f, i) for June, July, and August, respectively. All metrics are computed over domain 2.

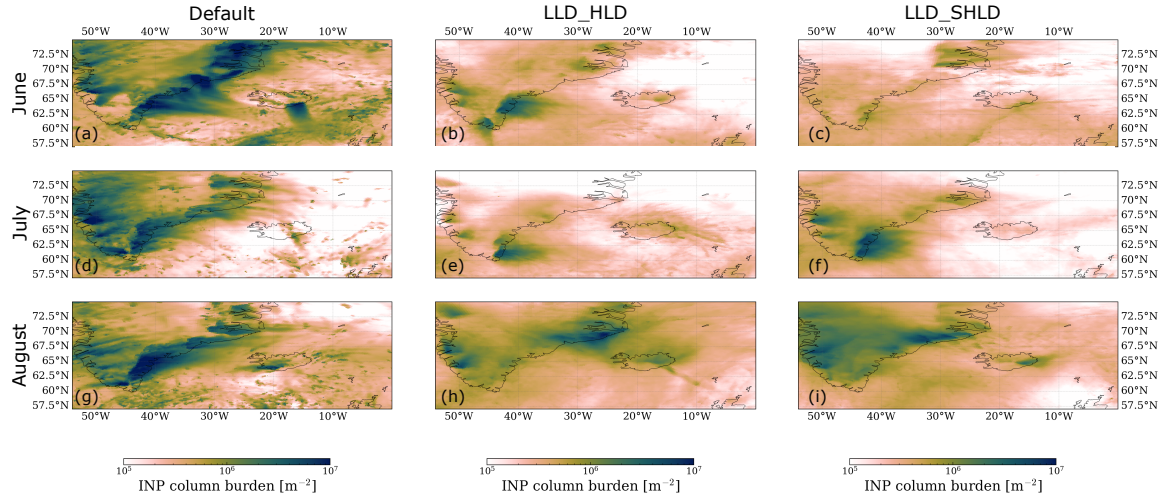


Figure 5.14.: Ice-nucleating particle (INP) column burden for June, July, and August 2021. Rows correspond to months; columns correspond to the default, LLD_HLD, and LLD_SHLD cases.

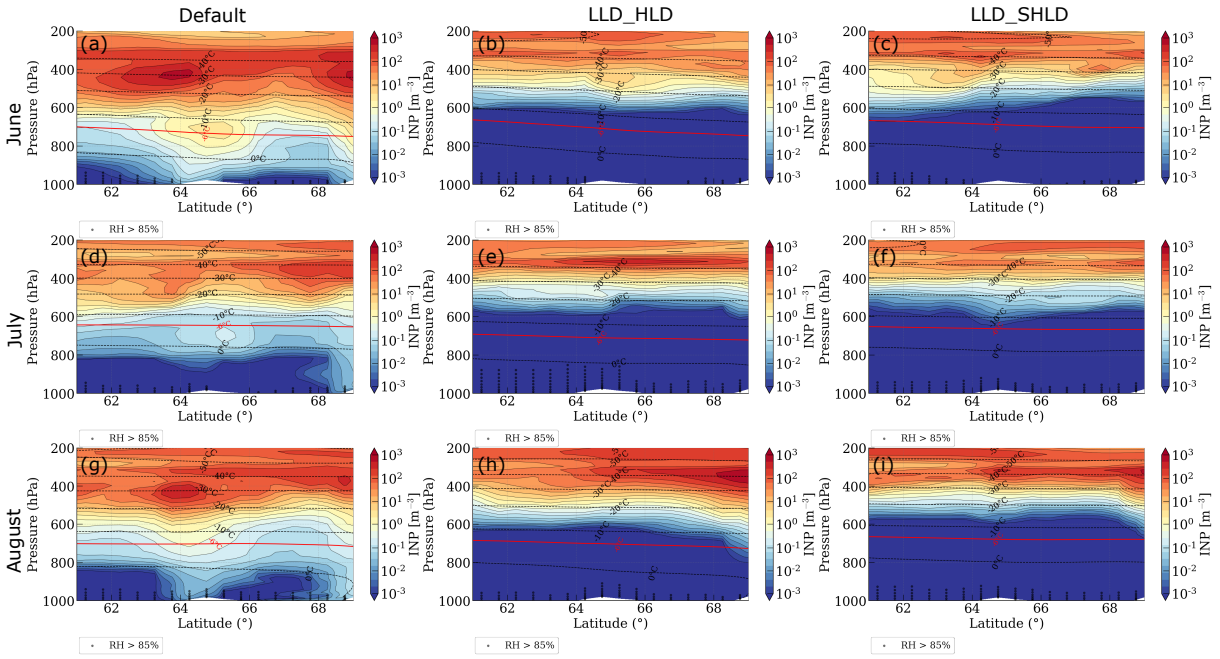


Figure 5.15.: Ice-nucleating particle (INP) zonal average for June, July, and August 2021 within the region 54.8° W $<$ lon $<$ 1.9° W and 61° N $<$ lat $<$ 69° N. Rows correspond to months; columns correspond to the default, LLD_-HLD, and LLD_SHLD cases. Red line shows the temperature zonal average for -6° C and vertical black dots the relative humidity zonal average above 85%.

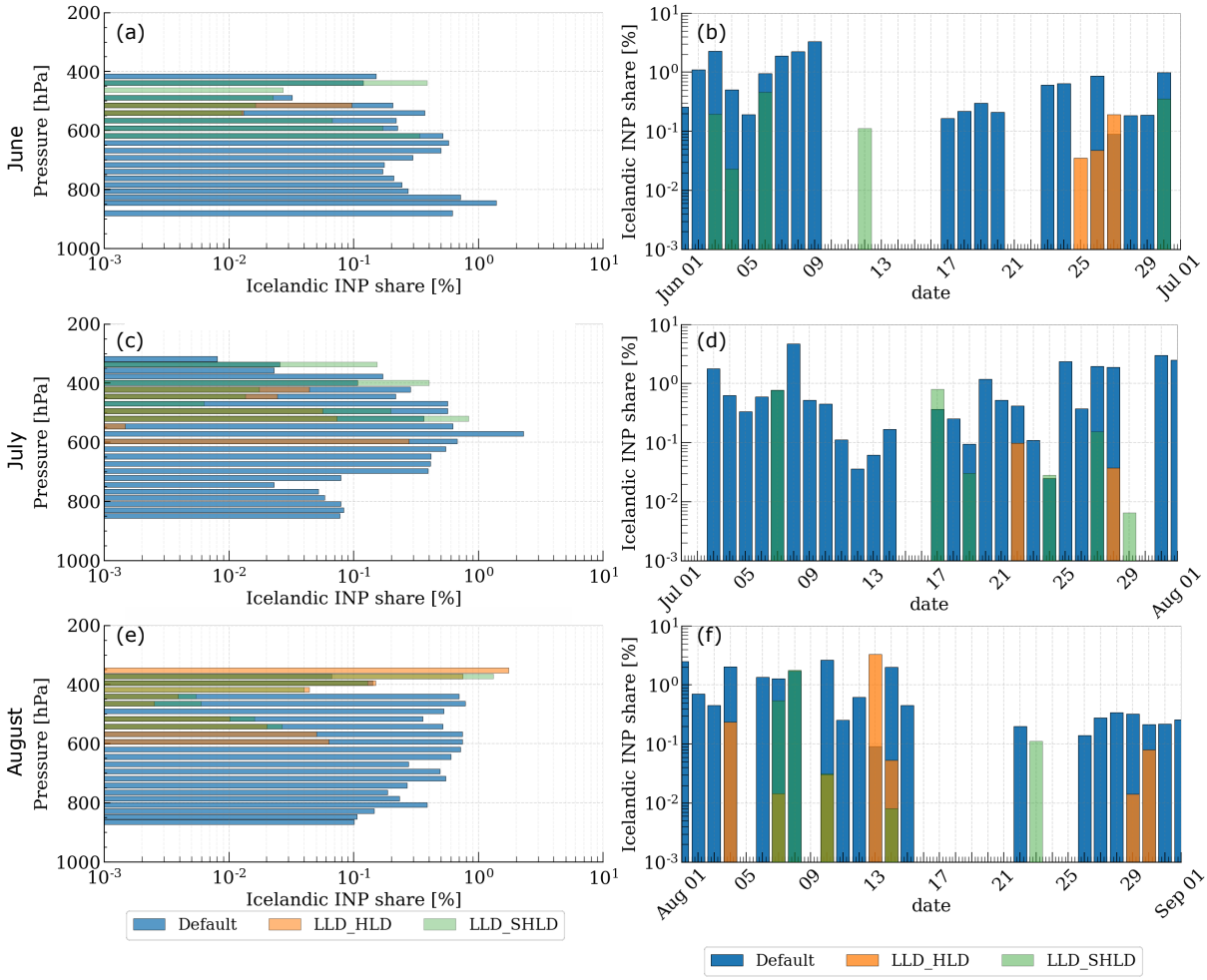


Figure 5.16.: Total Icelandic INP fraction (Icelandic INP over total INP; Icelandic plus elsewhere), summed over space and time (first column: a, c, e) and over space and height (second column: b, d, f), for June, July, and August 2021, for the three cases considered-default, LLD_HLD, and LLD_SHLD- within the region 54.8° W $<$ lon $<$ 1.9° W and 61° N $<$ lat $<$ 69° N. Rows correspond to months.

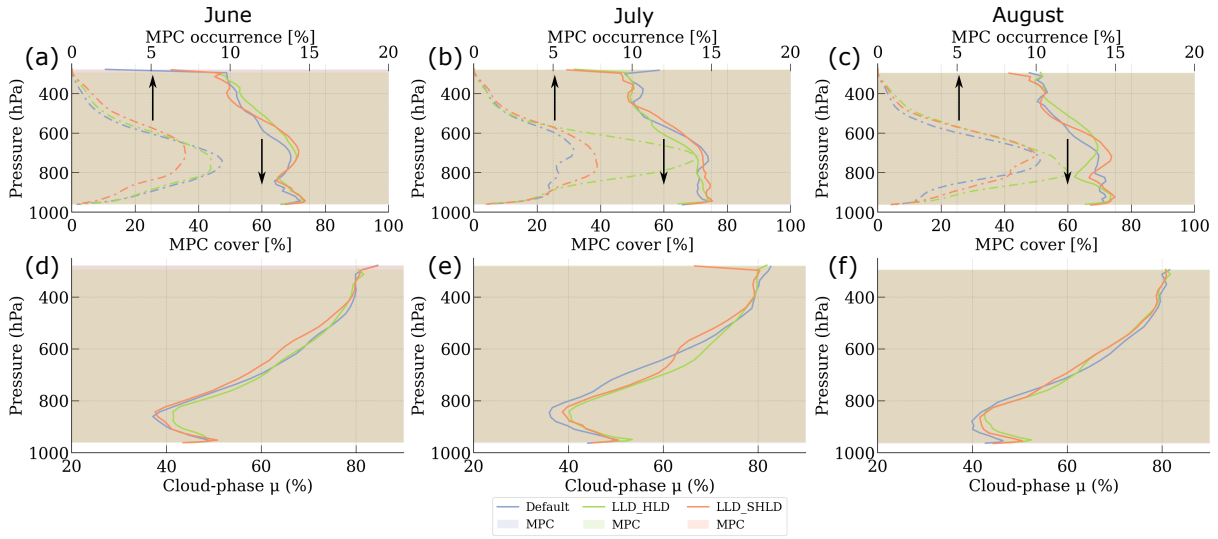


Figure 5.17.: Spatial averages of mixed-phase cloud (MPC) occurrence (top row) and spatiotemporal averages of MPC cover (bottom row) for June (a,d), July (b,e), and August (c,f) of 2021. Curves denote simulation cases: default (blue), LLD_HLD (green), and LLD_SHLD (orange); shaded bands show the corresponding MPC presence (overlapping of all color give a brownish color). Black arrows in panels (a–c) mark the x-axis used for the dashed curves (top axis) and the solid curves (bottom axis).

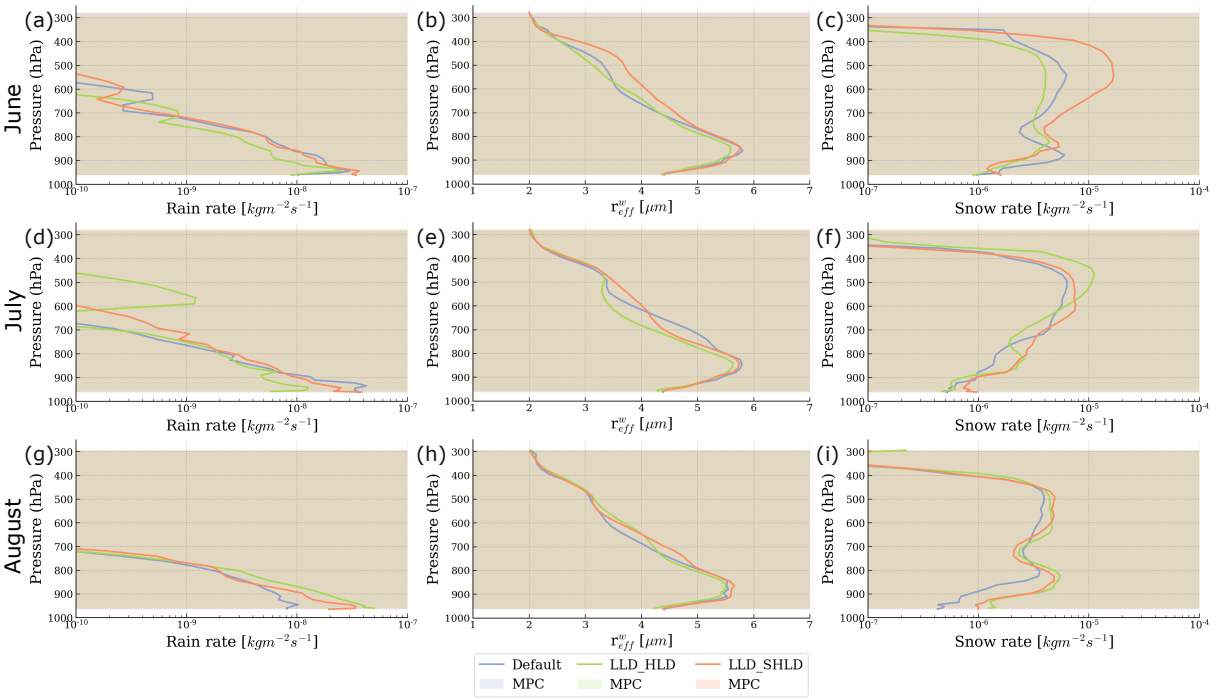


Figure 5.18.: Spatiotemporal profiles inside MPCs for June, July, and August (rows). Columns show rain rate (a,d,g), effective radius of liquid water (b,e,h), and snow rate (c,f,i). Lines denote simulation cases, default (blue), LLD_HLD (green), and LLD_SHLD (orange), and the shaded bands indicate the corresponding MPC presence.

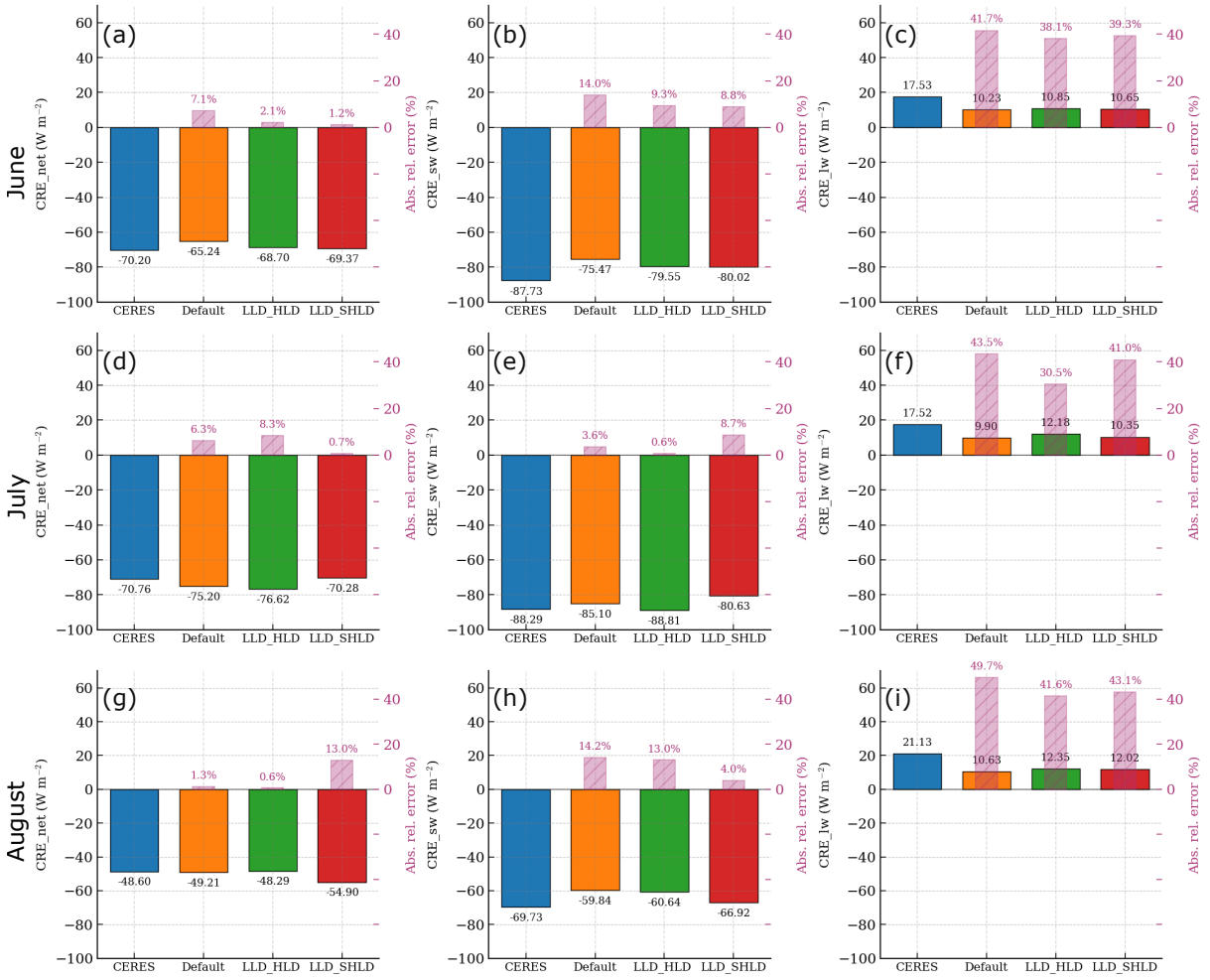


Figure 5.19.: Monthly cloud radiative effect (CRE) averaged over the study area for June, July, and August 2021 (rows). Columns show total CRE (a,d,g), shortwave (SW) CRE (b,e,h), and longwave (LW) CRE (c,f,i). Pink bars, referenced to the right y-axis, give the absolute percent error (positive value) of each case relative to CERES.

6. Discussion

6.1. Discussion of the experimental results

Several studies have found a correlation between the presence and amount of specific minerals, i.e. from the feldspar family (K-feldspar), quartz, pyroxene family, clay minerals (illite, kaolinite), in dust samples and the ice nucleation activity of these samples, pointing out that a better understanding of the IN behavior and accurate parameterizations can be obtained when the mineralogical composition of the samples is considered (Zimmermann et al., 2008; Atkinson et al., 2013; Harrison et al., 2019; Jahn et al., 2019). Motivated by this, in Sections 6.1.1 and 6.1.2, we analyzed the IN activity of our samples in the context of their mineral composition. Additionally, given the broad size range of our particles, their mineralogical composition may vary across different sizes. For this reason, in section 6.1.3, we investigate the impact of variations in mineralogical composition with particle size on IN activity for samples with different PSDs. Based on our findings of the previous sections and following previous works that scaled IN activity to the content of certain minerals in the studied samples (Atkinson et al., 2013; Harrison et al., 2019), we computed INAS density again in section 6.1.4, but scaling the surface area to the fraction of the main ice-active group of minerals at each size.

6.1.1. Mineralogy of Moroccan samples

A comprehensive analysis of our Moroccan samples was carried out in Panta et al. (2023). Here, we focus on the mineralogical single-particle composition and its dependence on size. In short, Panta et al. (2023) analyzed more than 300.000 freshly emitted individual particles using offline analysis with scanning electron microscopy (SEM) coupled with energy-disperse X-ray spectrometry (EDX). In their analysis, quartz was found to be the second largest constituent of the analyzed particles behind clay minerals. Furthermore, externally mixed feldspar represented 3.2% of all particles by mass, and a 10th of it was estimated to correspond to K-feldspar. An important finding of the Moroccan samples analyzed was that the relative amount of externally mixed feldspar and K-feldspar was invariant across particle size. In contrast, the mass fractions of complex quartz-like and feldspar-like particles increased with particle size, ranging from 5% to 18% for feldspar-like particles. As shown in Sect. 5.1.2, INAS densities obtained from our experiments fell within the 1% and 20% K-feldspar scaled fits (Harrison et al., 2019) and that the values obtained with AIDA aligned with the 20% K-feldspar scaled fit (Fig. 5.5a). Although quartz is the second largest constituent by mass of our samples, we observed a higher ice nucleation activity than that obtained for quartz by Harrison et al. (2019) (Fig. 5.5a). In order to understand the possible

role of quartz in promoting ice nucleation, it is important to mention that our samples were collected in September 2019 and stored in plastic bags. Later, in November 2022, they were sieved and stored in small plastic containers. Finally, one month later, they were used in AIDA and INSEKT experiments. The fact that our samples did not exhibit INA similar to quartz might suggest that, despite quartz being larger in mass contribution than feldspar, most of its active sites may have become inactive or quartz contribution was masked by the more active components like feldspar. Harrison et al. (2019) found that the INA of quartz samples decreased substantially after exposure to air during storage, as well as after exposure to water (Kumar et al., 2019). Consequently, the primary source of active sites in our Moroccan samples likely comes from the less abundant, but more aging-resilient feldspar active sites.

6.1.2. Mineralogy of Icelandic samples

The single-particle composition, size, shape, and mixing state of our freshly emitted Icelandic particles were studied in Panta et al. (2025). The size-resolved chemical and physical composition of over 190.000 individual particles with geometric diameters spanning from 0.1 µm - 120 µm were analyzed with computer controlled scanning electron microscopy/energy dispersive X-ray spectroscopy (ccSEM/EDX). It was found that the most abundant particle composition was Medium-Al mixed silicate particles (volcanic glass-like particles) varying between 35% and 93% by volume of the total aerosol population. Furthermore, a proportion of the Icelandic particles presented sulfate particles, suggesting the contribution of volcanic emissions. Potassium was almost absent from the samples. It was also observed that the relative volume fraction of the quartz-like particle group decreased with size, disappearing at 4 µm. In the same way, pyroxene occupied a higher relative volume fraction for smaller sizes, disappearing almost completely for diameters larger than 16 µm. However, the complex quartz-like structure was almost constant with size. As Panta et al. (2025) pointed out, notable differences emerge when comparing the mineralogy of Moroccan and Icelandic samples. For example, Icelandic dust consisted mainly of glass, intermediate plagioclase, and pyroxene. On the other hand, Moroccan samples were dominated by clays, feldspar, quartz, and calcite. Therefore, differences in the ice nucleation activity between these two dust sources are expected, confirming our experimental results (Fig. 6.1).

The INA of samples from Iceland and, more generally, close to volcanoes was already the focus in previous studies (Jahn et al., 2019; Steinke et al., 2011; Hoyle et al., 2011; Sanchez-Marroquin et al., 2020). In Fig. 6.1, we present a comparison between our parameterization and experimental data and other parameterizations from earlier studies. It can be seen that our parameterization (Table 5.1) predicts values almost one order of magnitude lower than previous studies for Iceland (Steinke et al., 2011) and pyroxene (Jahn et al., 2019). Pyroxene is particularly relevant because it has been suggested to be one of the most important minerals promoting the IN activity in volcanic samples. As the reason for this, it has been hypothesized that exsolution and the presence of perthitic microtextures (surface features that serve as ice-active sites) can occur in minerals commonly seen in volcanic ashes such as pyroxenes (Jahn et al., 2019). Contrasting our parameterization with the one obtained by Sanchez-

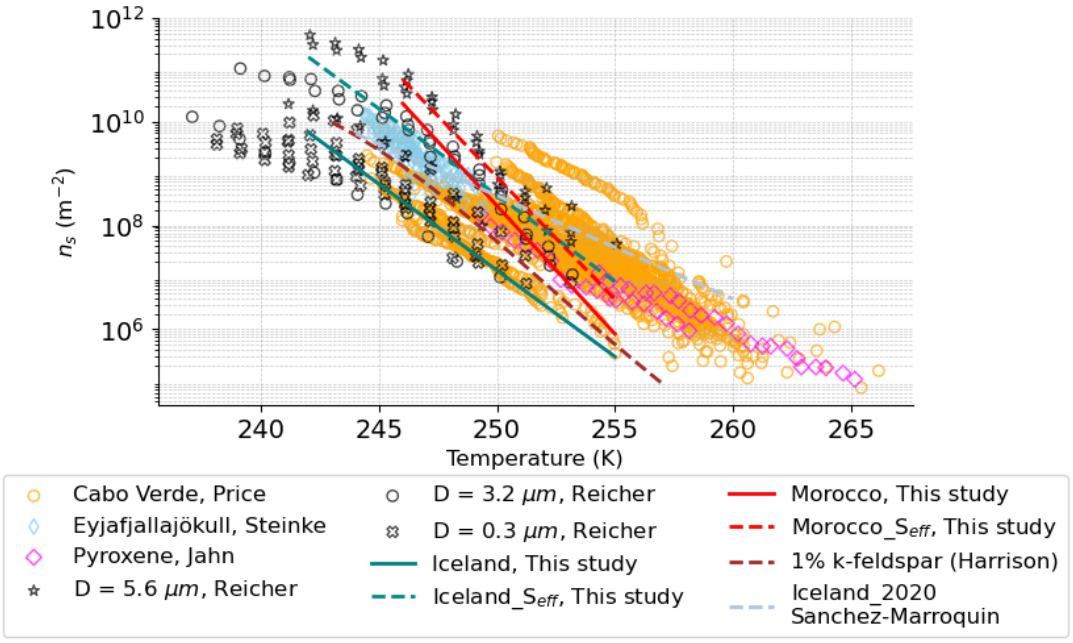


Figure 6.1.: INAS density parameterizations for Morocco with standard (red solid line) and effective (red dashed line) surface area, and Iceland with standard (blue solid) and with effective (blue dashed line) surface area. Comparison with experimental data from Steinke et al. (2011, blue diamonds), Jahn et al. (2019, purple diamonds), Price et al. (2018, orange circles), 1%-K-feldspar scaled Harrison et al. (2019, brown dashed line), Sanchez-Marroquin et al. (2020, light blue dashed line), and Reicher et al. (2019, open black stars, circles, and diagonal crosses) for samples with different cut-off diameter.

Marroquin et al. (2020), at first sight a large discrepancy appears. Nevertheless, upon closer inspection, interesting features can be noticed. First, the spread of n_s values derived with the same technique, i.e. INSEKT or AIDA experiments, for the whole temperature range is close to 1 order of magnitude (Fig. 5.4). Second, comparing the values obtained at the same temperature but with different techniques (AIDA vs. INSEKT) the spread increases to $\approx$ 2 orders of magnitude (Fig. 5.5). Additionally, data derived only with AIDA shows better agreement with Sanchez-Marroquin et al. (2020) parameterization. This variability of values between experiments might point to a variability in mineralogical content or other properties of the particles which might have a stronger impact at temperatures higher than 250 K given that for lower temperatures the n_s values tend to agree more for the considered experiments. Therefore, additional studies are needed to understand the differences in IN values when wet and dry techniques are used and whether these differences are related to the mineralogical composition of the samples.

As said before, pyroxene is considered one of the most ice-active groups present in samples of volcanic origin. The values obtained by Sanchez-Marroquin et al. (2020) are larger than those expected from pyroxene. However, the particles analyzed by Sanchez-Marroquin et al. (2020) are airborne samples making it feasible that their composition and IN activity is altered in comparison with samples obtained at surface level.

6.1.3. Size dependence

In the previous section, links between ice nucleation activity and mineralogy were considered. In this section, we discuss how the relationship between mineralogy and ice activity depends on particle size. For example, as mentioned in Sect. 6.1.1, the relative volume fraction of the complex feldspar-like and feldspar mixtures increased with particle diameter for our Moroccan samples. The subsequent question is therefore whether this size dependence has any influence on the INA of the samples. To answer this, we compared experiments carried out with the same start temperature, but with different surface area concentration ratios of the three modes (S_{fr}, S_{cr} and S_{scr}) defined according to Eq. 6.1:

$$1 = \frac{S_f}{S_T} + \frac{S_c}{S_T} + \frac{S_{sc}}{S_T} = S_{fr} + S_{cr} + S_{scr} \tag{6.1}$$

where S_T is the total surface area concentration. S_f, S_c, and S_{sc} are the surface area concentration coming from fine, coarse and super-coarse particles.

6.1.3.1. Moroccan samples

Figure 6.2 presents the ice active fraction (%) for the selected AIDA experiments. Overall, no strong relationship between the surface area ratio contribution of particles of a certain size (fine, coarse or super-coarse, Fig. 6.2e) and the ice active fraction was found. For instance, Fig 6.2a presents a similar ice active fraction for experiments 5 and 16, in which the contribution of super-coarse particles to the total surface area to experiment 5 is higher than to experiment 16. In Fig. 6.2b experiments 9 and 20 exhibit a similar ice active fraction and have a similar contribution of super-coarse particles, but with a difference in the proportion of fine and coarse contributions. Figure 6.2d presents the case in which for one experiment almost all the surface area concentration comes from fine particles (experiment 29, 99 %) while the other experiment has a more even contribution from fine, coarse, and super-coarse (experiment 28, 40%-30%-30%). In this example, the largest difference in ice activity was observed at warmer temperatures. At colder temperatures, the difference is less pronounced. A similar trend is observed for experiments 26 and 27, Fig 6.2c, in which the ice active fraction presents a similar behavior regardless of the difference on their surface area fractions.

A reason for similar ice active fractions of the samples regardless of their size distribution is probably that the relative volume fraction of K-feldspar, the most ice-active mineral in the sample (Atkinson et al., 2013), was constant throughout the size distribution. This same behavior, i.e. almost equivalent ice-activity between samples and temperatures, can be concluded from Figs. 5.3 a and b, in which all experiments can be described by a straight line with a low dispersion. This behavior suggests that, if there is any dependence, in order to observe this dependence of the ice active fraction on size, more substantial contrasts between the surface area distributions in the compared experiments are required.

6.1.3.2. Comparison with other studies for Moroccan samples

Evidence for a dependence of the ice active fraction on particle size has been reported in earlier studies. Figure 6.1 presents data from a study where airborne particles from mid-latitude were collected and subsequently sieved and their ice-activity analyzed as a function of particle diameter, finding dependence of INA on size (Reicher et al., 2019). It can be seen that our fit for Moroccan samples is in agreement for particles with a cut-off diameter of 3.2 µm. Although there is a difference in ice activity with size distribution for cut-off diameters of 5.6 µm and 3.2 µm, this is not as pronounced as for particles with cut-off diameter of 0.3 µm, consistent with our results that the dependence of n_s on particle size requires a strong difference in the size distribution. Nevertheless, it is important to acknowledge that differences between airborne and surface-collected particles have been observed (Boose et al., 2016). Additionally, the mineralogy of the samples analyzed in Reicher et al. (2019) was not explicitly examined. Therefore, comparisons of our samples with the ones in Reicher et al. (2019) should be interpreted with caution.
In another study, airborne particles from the Eastern Mediterranean were sampled and their INA assessed (Gao et al., 2024), finding a positive correlation between the proportion of coarse particles ($1 \geq$ µm) and the average number concentration of INP. The strength of the correlation was dependent on the source of the sample and whether the sample was above or below the planetary boundary layer, giving place to aging and mixture with other components, e.g. biological substances, and not solely to mineralogy. In conclusion, evidence of higher IN activity as the aerosol population contains larger particles was not clearly observed for our Moroccan samples.

6.1.3.3. Icelandic samples

Regarding our experiments, Fig. 6.3e and f show the surface area concentration ratio and number particle concentration ratio of each experiment divided according to the pyroxene size dependence presented in Panta et al. (2025). Comparing again, this time for Icelandic dust samples, our experiments carried out at similar start temperatures but with different size ratio contributions, we found that almost all experiments that contained a higher proportion of small particles yielded higher ice active fractions (Fig. 6.3). For example, in Fig. 6.3a, experiment 3 exhibited a lower ice active fraction than experiment 11. Additionally, experiment 3 showed a lower surface area ratio for particles with diameters smaller than 4 µm compared to experiment 11. A similar trend can be observed in Fig. 6.3d. Despite a difference of approximately 1 K in the initial temperature between experiments 6 and 30, experiment 6 (conducted at a lower temperature) did not exhibit a higher ice active fraction. Interpreting this result in conjunction with the surface area ratio (Fig. 6.3e), we note that the contribution of particles with diameters smaller than 2 µm to the total surface area is significantly lower in experiment 6 than in experiment 30. Experiments 17 and 22 (Fig. 6.3c) displayed nearly identical ice active fraction activity and surface area ratios. Finally, Fig. 6.3c reveals a gradient in ice active fraction activity, increasing from experiments 34 to 33 to 31. Notably, the contribution of particles with diameters smaller than 2 µm to the total surface

area in experiment 34 was minimal. This experiment exhibited the lowest ice active fraction values, and only at a temperature approximately 246.5 K did its ice active fraction become comparable to that of experiment 33. This behavior aligns with the size dependence of pyroxene, where the relative volume fraction of pyroxene is higher for smaller particle sizes and decreases with increasing size. Consequently, a larger surface area concentration from small particles implies a higher probability of pyroxene content and the presence of active sites. However, a discrepancy arises in experiment 31. Based on the aforementioned reasoning, experiment 33 would be expected to exhibit the highest ice active fraction among the compared experiments, as it has the highest contribution from particles with diameters smaller than 4 µm at that temperature. Contrary to this expectation, experiment 31 demonstrated the highest ice active fraction. The reasons for this deviation remain unclear. Nevertheless, we can conclude that, in general, a trend was observed in which experiments with similar surface area ratios exhibited similar ice active fractions, and those with a greater contribution from smaller particles (diameters below 4 µm) tended to have higher ice active fractions.

6.1.3.4. Comparison with other studies for Icelandic samples

Contradictory behavior has been reported regarding the ice-activity of Icelandic and volcanic samples. Steinke et al. (2011) did not observe differences in n_s when evaluating samples with diameters smaller than 5 µm and samples with diameters smaller than 10 µm. On the other hand, Jahn et al. (2019) found that, when analyzing 4 different size fractions (PM2.5, PM2.5-10, PM10-37, and PM37) of the same sample, the smallest particles showed a higher n_s. Nevertheless, the difference between PM2.5-10 and PM10-37 was not very pronounced, with the most noticeable difference being the onset of ice nucleation, which occurred at a warmer temperature for PM2.5-10. Finally, Sanchez-Marroquin et al. (2020) reported that samples with the largest surface area had the highest number of INP concentration. However, when analyzing the data in terms of n_s (normalizing the number concentration of INP by the total surface area) or the ice active fraction (ice number concentration divided by the aerosol concentration), there was no clear trend with size.

What can explain the ambiguity regarding results on the size dependence of INA of volcanic-related samples? Following the idea that pyroxene is one of the main players in the INA of samples of volcanic origin, we can confirm that in our Icelandic samples, the greatest contribution to the relative volume fraction of pyroxene came from particle sizes in the range 0.1 - 8 µm and almost no contribution came from sizes larger than 16 µm (Panta et al., 2023). This feature may explain why in Steinke et al. (2011) no size dependence was observed. In their experiment, when including particles larger than 5 µm the size fraction contributed only around 5% to the total surface area (Fig. 6.4). Under the assumption that the size dependence of mineralogical composition followed a similar behavior as for our samples, only a small proportion of pyroxene was removed compared to what remained in their experiment with particles smaller than 5 µm. Hence, the total amount of pyroxene or minerals with similar size dependence for both samples did not differ substantially, leading to a similar ice activity. This reasoning also matches with

what was reported in Jahn et al. (2019). In their study, PM2.5 exhibited the highest ice active fraction. PM2.5-10 presented a similar onset of freezing and at the early stage of cooling had a similar behavior as PM2.5, but once the most active sites were activated, the ice active fraction later became comparable to PM10-37, which lacks most of the pyroxene under the assumption that their samples have a similar mineralogical size dependence to ours. However, the above reasoning does not explain that in Sanchez-Marroquin et al. (2020) more INP were related with larger surface area concentrations. Nevertheless, as mentioned before, the relationship presented in Sanchez-Marroquin et al. (2020) for n_s or the ice active fraction with size does not clearly indicate that samples with larger surface area concentration will have a higher INA. Additionally, the fact that the ice active fraction in their experiments spans several degrees of temperature is a strong indication of the heterogeneity of the samples, as well as the variation in the size-resolved composition of the different samples, indicating a more complex composition and interplay of different ice nucleating agents.

6.1.3.5. Quantitative assessment of size dependence

We have computed pairwise comparisons of the ice active fraction between experiments sharing the same dust source but differing in particle size distribution. For each pair, we report the median $\log_{10}$ ratio ($\tilde{r}$) of frozen fractions at matched temperatures (temperature difference smaller than 0.7 K), defined as $\tilde{r} = \text{median}\left(\log_{10}\frac{FF_a}{FF_b}\right)$, where FF_a and FF_b are the ice active frozen fractions at matched temperatures for experiments a and b, respectively, as reported in Figs. 6.2 and 6.3 for Morocco and Iceland, its interquartile range ($\text{IQR}_{\log}$), the geometric mean ratio ($G = 10^{\tilde{r}}$), and the two-sided Wilcoxon signed-rank test p-value. The Wilcoxon signed-rank test is a non-parametric test of the null hypothesis that the median log ratio is zero, i.e. that the two experiments are statistically equivalent. A p-value below 0.05 indicates that the null hypothesis is rejected at the 5% significance level, meaning that a difference as large as observed would occur by chance in fewer than 5% of cases if the two experiments were truly equivalent.

For Morocco (Table 6.1), the four pairwise comparisons yield geometric mean ratios ranging from 0.664 (experiments 27 and 26) to 2.138 (experiments 28 and 29), indicating that at the typical matched temperature, experiment 28 has 2.138 times higher frozen fraction than experiment 29. Only one pair reaches statistical significance (experiments 28 and 29, p=0.016). The remaining three pairs show no significant difference (p in the range of 0.062–0.375), and the median log ratios are similar to their $\text{IQR}_{\log}$, e.g. experiments 5 and 16 have a $\tilde{r}$ of 0.277 and $\text{IQR}_{\log}$ = 0.180. This shows that the ice active frozen fraction shows no systematic dependence on particle size for Moroccan dust: the differences between size fractions are modest, statistically weak, and do not point consistently in any direction.

For Iceland (Table 6.2), all five pairs with sufficiently large number of matched points (n$\geq$ 6) yield statistically significant differences (p in the range of 0.008–0.031), with geometric mean ratios ranging from 2.1 to 8.3. The pairs with the largest G values correspond to experiments 31 and 34 and experiments 11 and 3, with geometric mean ratios of 8.296 and 5.043, respectively. As shown in Fig. 6.3, experi-

ments 11 and 31 contain a larger contribution from particles with diameters smaller than 0.8 µm to the total surface area than experiments 3 and 34. In contrast, Fig. 6.3c shows that experiments 17 and 22 have nearly identical surface area fractions, which is reflected in their statistics: although experiment 17 is consistently above experiment 22 (p=0.008), the ratio varies considerably across the temperature range (IQR_{log}=0.306, $\tilde{r}$=0.360), with a geometric mean ratio closer to those observed for Moroccan paired experiments. It is worth noting that for all other Icelandic pairs the IQR_{log} is at least half the value of $\tilde{r}$, indicating a more consistent and strong offset across temperatures. Furthermore, the case of experiments 31 and 33 is noteworthy: despite experiment 33 having a larger surface area contribution from particles smaller than 8 µm than experiment 31, experiment 33 exhibits systematically lower ice active frozen fractions at comparable temperatures, a difference that is statistically significant (p=0.016, $\tilde{r}$=0.477, IQR_{log}=0.237). It is not clear why this pair deviates from the general trend, whereby a larger contribution from smaller particle diameters to the total surface area is associated with higher ice-active frozen fractions at equivalent temperatures.

The one pair that does not reach significance (experiments 30 and 6, p=0.125) is constrained by n=4 matched points, for which p=0.125 is the minimum achievable p-value by construction of the exact Wilcoxon test, regardless of size effect. However, the geometric mean ratio of 5.399 and IQR_{log} of 0.208 for this pair are consistent with the other Iceland pairs. Taken together, the Iceland comparisons provide quantitative evidence for a size-dependent ice nucleation activity signal that is both statistically significant and physically large.

Table 6.1.: Derived statistics for the pairwise logarithmic ratio of ice active frozen fraction between experiment number a ($\exp_a$) and experiment number b ($\exp_b$), defined as $\log_{10}(FF_a(T)) - \log_{10}(FF_b(T))$, computed at matched temperatures (temperature difference smaller than 0.7 K) for the Morocco experiments shown in Fig. 6.2. n is the number of matched ice active frozen fraction pairs used in the calculations, $\tilde{r}$ is the median logarithmic ratio, IQR_{log} is the interquartile range of the log ratio ($Q_{75} - Q_{25}$), $G = 10^{\tilde{r}}$ is the geometric mean ratio, and W_p is the two-sided Wilcoxon signed-rank test p-value.

$\exp_a$(#)	$\exp_b$(#)	n	$\tilde{r}$	IQR_{log}	G	W_p
5	16	5	0.277	0.180	1.893	0.062
20	9	7	0.054	0.069	1.131	0.297
27	26	7	-0.178	0.152	0.664	0.375
28	29	7	0.330	0.220	2.138	0.016

6.1.4. Effective surface area

The previous results (Table 5.1) were calculated with the standard assumption that $n_s(T)$ is independent of size, i.e. the density of active sites is constant for all size bins. However, under the assumption that the INA of a sample can be linked to the content of a specific mineral or group of minerals, the probability of finding an active site over the surface will not be the same as for all sizes when the relative fraction of

Table 6.2.: Derived statistics for the pairwise logarithmic ratio of ice active frozen fraction between experiment number a ($\exp_a$) and experiment number b ($\exp_b$), defined as $\log_{10}(FF_a(T)) - \log_{10}(FF_b(T))$, computed at matched temperatures (temperature difference smaller than 0.7 K) for the Iceland experiments shown in Fig. 6.3. n is the number of matched ice active frozen fraction pairs used in the calculations, $\tilde{r}$ is the median logarithmic ratio, $\mathrm{IQR}_{\log}$ is the interquartile range of the log ratio ($Q_{75} - Q_{25}$), $G = 10^{\tilde{r}}$ is the geometric mean ratio, and W_p is the two-sided Wilcoxon signed-rank test p-value.

$\exp_a$(#)	$\exp_b$(#)	n	$\tilde{r}$	$\mathrm{IQR}_{\log}$	G	W_p
11	3	8	0.703	0.220	5.043	0.008
31	33	7	0.477	0.237	2.998	0.016
31	34	6	0.919	0.222	8.296	0.031
33	34	6	0.326	0.151	2.117	0.031
17	22	9	0.360	0.306	2.293	0.008
30	6	4	0.732	0.208	5.399	0.125

that mineral varies with size. This is the case for both of our samples, Morocco and Iceland, where the relative fractions of feldspar and pyroxene vary with particle size.

If enough information about the mineral composition of a sample is known (as well as its size dependence) and if there is a group of minerals that dominates the INA (for example, feldspar), we hypothesize that accounting for this information when computing the surface area will improve the obtained value of $n_s(T)$ to predict the concentration of INPs. To test this hypothesis, we calculated $n_s(T)$ again, but this time we scaled the surface area to the fraction of feldspar or pyroxene present in each size bin (effective surface area) according to Panta et al. (2023, 2025).

Figure 6.1 presents the obtained fit for $n_s(T)$ ($ln(n_s(T))$ = 211.5026 - 0.7669T for Iceland and $ln(n_s(T))$ = 291.6934 - 1.0845T for Morocco) using the effective surface area ("Iceland_S_{eff}, This study" and "Morocco_S_{eff}, This study"). The main effect of incorporating this new surface area for Iceland is an increase in the n_s value by ≈ 1.5 orders of magnitude. Additionally, the new fit agrees with previous measurements of samples with similar origin or mineralogy, such as those reported by Steinke et al. (2011) and Jahn et al. (2019). This result can be interpreted as a good indicator that the INA of Icelandic samples can be scaled to the content of pyroxene at each size of the considered PSD.

Regarding Morocco, the effect of considering the effective surface area is less pronounced as for Iceland, Figure 6.1 shows that the difference between both parameterizations is less than 1 order of magnitude and is within the 95% confidence interval of the parameterization obtained with the complete surface area. This can be understood in terms of the mineral composition dependence on size, there is low variation of the relative volume fraction of feldspar (and k-feldspar) with size and accounting for almost 30% for all sizes (Panta et al., 2023).

The differential nucleus concentration is a less commonly used metric in comparison with n_s. Nevertheless, it provides additional information that cannot be derived from $n_s(T)$, for example, the computation of $w = \Delta ln(k(T))/\Delta T$ (Vali, 2014) allows comparing the freezing activity of samples when the temperature is varied ΔT. In this way, nearly constant values of w indicate that the freezing activity of

the sample varies in a constant fashion when temperature is changed. $k(T)$ was presented in Fig. 5.3 for Morocco and Fig. 5.4 for Iceland. Moroccan samples presented a similar slope (w, especially for AIDA experiments) and less spread of the data around the linear fit, while Icelandic samples showed a larger difference in slope for AIDA experiments and a pronounced deviation from a linear behavior for INSEKT experiments. Upon closer inspection, it can be noticed that for our Moroccan samples, $k(T)$ decreased nearly exponentially with temperature (Fig. 5.3a), whereas a more complex shape is observed for our Icelandic samples, where for temperatures warmer than 248 K the data presents a lower spread than for colder temperatures (Fig. 5.4a). In the work of Vali (2014), w was analyzed for several previously published experiments and it was found that no general trend in the behavior of w was present, i.e. deviations from the linear trend were quite frequent, and no possible sources of the deviations were suggested. Taking into account the characteristics of the mineral size dependence of our samples, as well as the results from preceding works discussed in previous sections and our own results, we hypothesize that one reason for the change in the exponential decrease of $k(T)$ with temperature is the variation of the presence of the same dominant factor promoting ice nucleation. In the context of our experiments, this dominant factor was linked to mineralogy. In our Moroccan samples, all size bins presented contributions from K-feldspar and feldspar, and the biggest difference in the INA for samples of different surface area ratio contributions from fine, coarse, and super-coarse particles was observed at warmer temperatures. On the other hand, we observed a strong dependence with size of the fraction of pyroxene, one of the main minerals for ice nucleation in our Icelandic samples. Pyroxene was mainly present in particles smaller than 8 µm and almost absent in particles with diameters larger than 16 µm. In this way, once the smaller and more active sizes nucleate at relatively warm temperatures, the subsequent nucleation is likely dominated by other minerals or a different probability of finding active sites on the surface of the remaining particles, changing the behavior of nucleation and the slope of w. To test this hypothesis, further experiments are required using samples of which the size dependence of their mineralogy is known and in which different size distributions/fractions are considered.

6.2. Discussion of the modeling results

In Sect. 5.2.1, the comparison between simulated and observed PM_{10} concentrations revealed that some concentration peaks exhibited timing mismatches. Several factors can explain the timing mismatch between the observed and simulated PM_{10} concentrations reported in Fig.5.11. Model simulations were performed with a horizontal grid resolution of $\approx$10 km; although fields were interpolated to the station's latitude, longitude, and height, Iceland's dust sources are highly localized, so this resolution may be too coarse to represent isolated events accurately. Small errors in emission timing, plume transport, or deposition can shift modeled peaks by days, reducing correlation at daily scales despite reasonable weekly means (Jin et al., 2021). A more robust validation requires comparison against multiple observation sites; however, such measurements are sparse in time and space for Iceland. With respect to the

Icelandic dust transport, the analysis for the months of June, July, and August highlights a clear seasonal shift in Icelandic dust vertical distribution and transport between months. In June–July, the zonal-mean fields showed dust largely confined within the planetary boundary layer (PBL) and with lower mean atmospheric concentrations; by August, emissions intensified and the vertical extent regularly exceeded the PBL, reaching 700 hPa (2.5–3.2 km), a configuration that favors long-range transport. These features are consistent with prior modeling and pathway analyses showing that most of the emitted dust is deposited in Iceland itself or in the near ocean (Groot Zwaaftink et al., 2017). From an INP perspective, the zonal-mean temperatures indicated that regions with Icelandic dust rarely fall below -10° C, especially in June and July (Fig. 5.13a,d,g). This limits the potential for Icelandic mineral dust to act as immersion-mode INPs, since, for all test cases considered here (Table 4.4), the maximum immersion-freezing activation temperature in the current ICON implementation is -6° C. Consequently, even with appreciable dust within the PBL, the instantaneous INP efficacy for immersion freezing mode is modest in early summer as was shown in Fig. 5.15a,d,g. Figures 5.14 and 5.15 indicated that Icelandic INPs were largely confined to Iceland itself. This becomes especially clear when replacing the Ullrich et al. (2017) scheme (default case) with the source-aware parameterizations of Vergara-Palacio et al. (2026) (LLD_HLD and LLD_SHLD cases): the default scheme yields INP values that are up to three orders of magnitude larger than the Icelandic (HLD) parameterization and about two orders of magnitude larger than the Moroccan (LLD) parameterization (Figs. 5.5 and 6.1). As a consequence of the lower INP activity assigned to Icelandic dust in the Vergara-Palacio et al. (2026) schemes, the activated INP over Iceland decreased by more than two orders of magnitude above 600 hPa, leading to a much weaker aloft INP signal. Additionally, Fig. 5.16 shows that the main contribution of Icelandic INP to the total INP concentration in immersion-freezing mode occurred between $\approx$ 400 hPa and 900 hPa for all months considered (JJA), even though the largest concentrations of Icelandic dust were generally located at pressures higher than 700 hPa. This can be explained by the fact that the pressure levels with the largest Icelandic dust concentrations were often warmer than the immersion freezing threshold (-6° C). Although Icelandic dust was less frequently found at pressures lower than 700 hPa, those levels more often satisfied the temperature and supersaturation conditions required for immersion freezing. Another variable to consider when comparing the other test cases with LLD_SHLD is that, unlike the others, LLD_SHLD is scaled by mode-specific constant factors (Sect. 4.2.8). Thus, the ice-nucleation activity predicted by LLD_SHLD depends on the emitted dust in a different manner than the other parameterizations. The default and LLD_HLD cases use the total particle concentration and the total surface area of atmospheric Icelandic dust, whereas LLD_SHLD assigns a larger weight to the surface area contributed by smaller particles, leading to a different calculated total surface area. Although the diagnosed MPC properties changed only modestly across the experiment set (Table 4.4), the CRE responses differed noticeably. For every month, either LLD_HLD or LLD_SHLD agreed better with CERES than the default case. This improvement likely reflects differences in cloud occurrence/cover and, to a lesser extent, precipitation (rain/snow) rates. For example, in July the LLD_HLD configuration yielded the closest

overall match to CERES, with an absolute relative error in SW CRE < 1%; July is also the month when cloud occurrence was roughly twice as high in LLD_HLD than in the other cases (Fig. 5.17b). Increased cloud presence is consistent with a more negative SW CRE, particularly when other controls—such as liquid effective radius and rain/snow rates—remain similar across experiments (Fig. 5.18d–f). However, although LLD_HLD and LLD_SHLD differ only in the HLD parameterization, they exhibited notable differences in the estimated CRE. For July and August, the disagreement in SW CRE between LLD_-HLD and LLD_SHLD was larger than their respective differences from the default case (Fig. 4.13d,e and g,h for July and August, respectively). Examining the cloud properties for these same months reveals no clear trend between LLD_HLD and LLD_SHLD. For example, in July the MPC occurrence associated with LLD_SHLD exceeded the default case but remains below LLD_HLD (Fig. 5.17b). Nevertheless, the SW CRE in July for LLD_SHLD was the largest, at -80.63 Wm^{-2} compared to -85.10 Wm^{-2} and -88.81 Wm^{-2} for the default and LLD_HLD case, respectively. If MPC occurrence alone controlled SW CRE (with other cloud properties held constant), one would expect the smallest occurrence (default case) to yield the largest SW CRE. The fact that LLD_SHLD attained the less negative SW CRE despite an intermediate MPC occurrence indicates sensitivity to additional factors, such as modest differences in cloud optical depth (via LWP and effective radius), cloud-phase, cloud altitude and vertical overlap, horizontal distribution relative to solar zenith angle, and surface albedo. Over highly reflective surfaces (snow/sea ice), increasing cloud cover can reduce the top-of-atmosphere reflected shortwave relative to the bright surface, making the SW CRE less negative or even positive; conversely, the same cloud change over a dark ocean strongly increases reflection, making SW CRE more negative. Therefore, the larger SW CRE differences between LLD_HLD and LLD_SHLD, despite broadly similar bulk cloud metrics, are physically plausible and likely arise from small but radiatively important shifts in cloud optical/thermodynamic properties and their co-location with high-albedo surfaces, rather than from MPC occurrence alone. Differences between the test cases in simulated LW CRE are smaller than for SW CRE, indicating that the cloud properties controlling LW CRE are less sensitive to the choice of parameterization, and thus to INP concentration, than those controlling SW CRE. Additionally, all test cases underestimate LW CRE relative to CERES. This bias could be related to a combination of factors such as lower cloud-top heights (warmer tops), reduced infrared optical thickness (thinner clouds), or smaller high-cloud fraction/overlap, each of which increases all-sky outgoing LW radiation and thereby decreases LW CRE. For example, in July the LLD_HLD case yields the largest LW CRE (Fig. 5.19f), coinciding with the largest MPC occurrence (Fig. 5.17b). That said, it remains difficult to attribute CRE differences unambiguously to any single cloud property, given the covariation among microphysics, macrophysics, and thermodynamics. This underscores the need for targeted sensitivity studies to isolate how INP parameterization choices propagate to radiative effects. Finally, we note that our experiments differ only in the immersion-freezing pathway; deposition nucleation was held fixed (use of Ullrich et al. (2017) parameterization for all test cases). Future work should examine the impact of alternative deposition-mode parameterizations on clouds and cloud radiative properties.

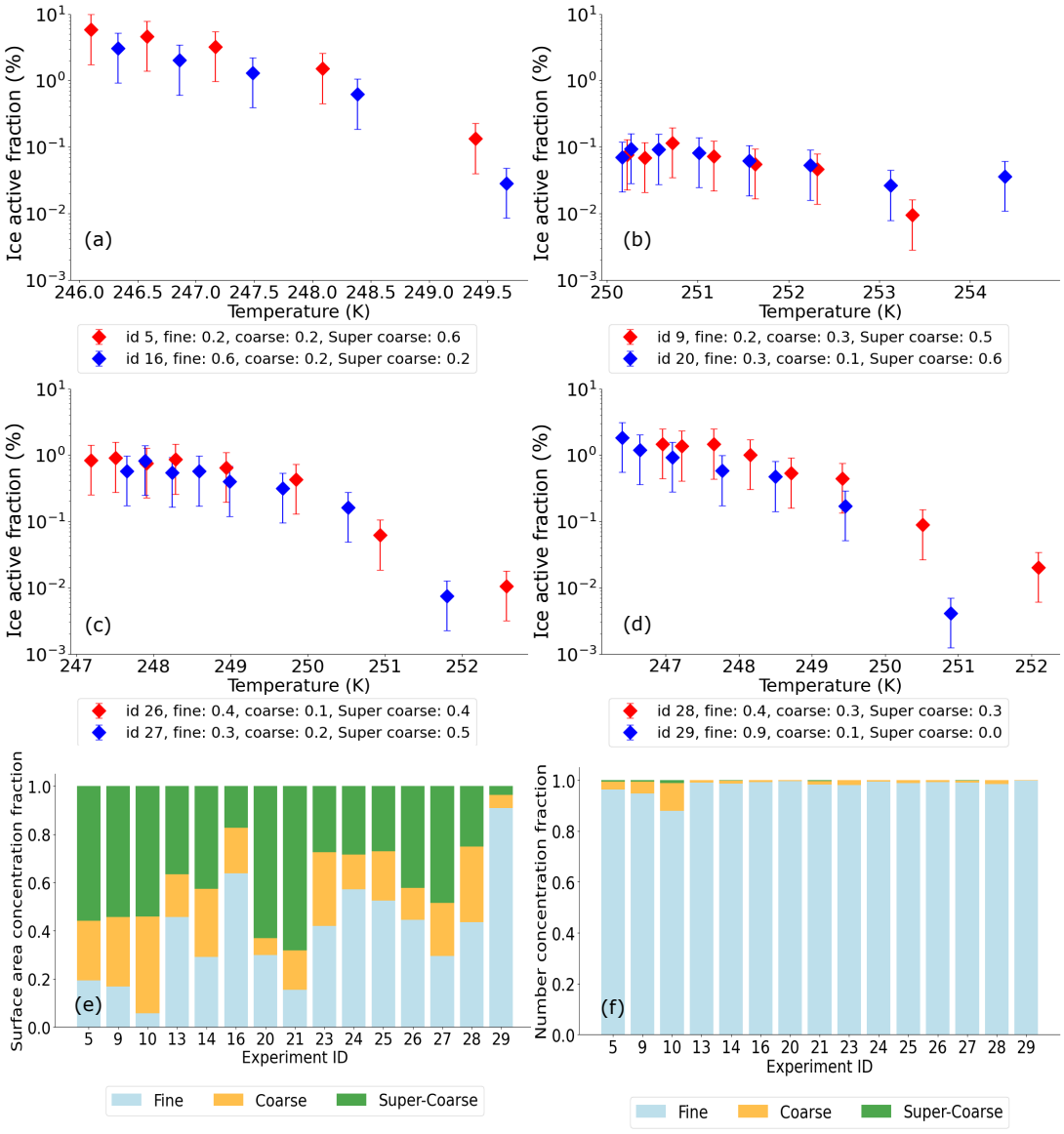


Figure 6.2.: Ice active fraction for AIDA experiments carried out with the same initial temperature, but using dust aerosol with different contributions of fine, coarse, and super-coarse particles to the total surface area for Moroccan samples, contribution from each size range are indicated in the label. a) experiments 5 and 16 at 249 K, b) experiments 9 and 20 at 254 K, c) experiment 26 and 27 at 252 K, d) experiment 28 and 29 at 251 K, e) Surface area concentration ratio and, f) number fraction of particles for Moroccan samples divided into fine, coarse, and super-coarse particle contributions for each experiment.

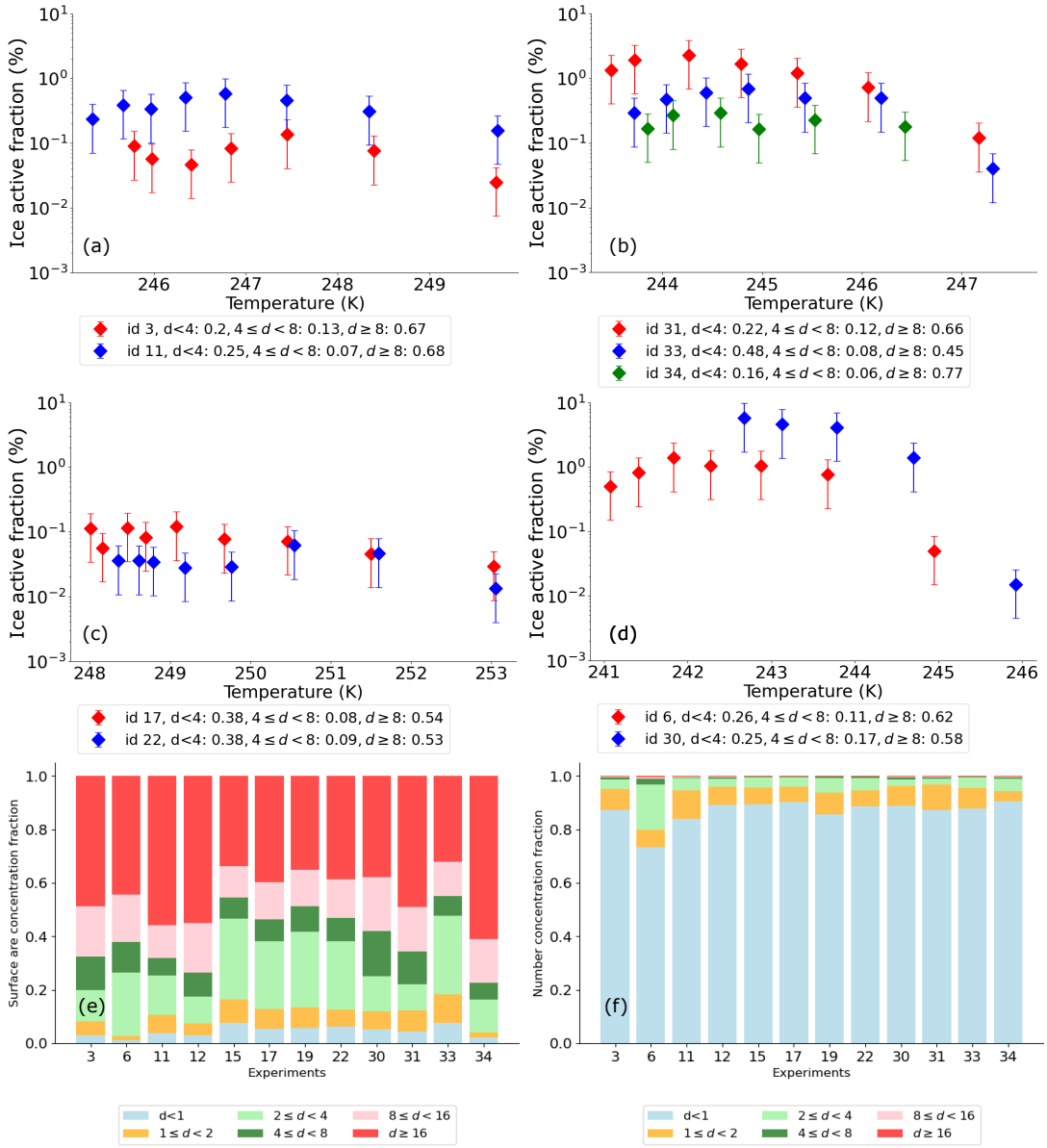


Figure 6.3.: Ice active fraction for experiments with Icelandic samples carried out at the same initial temperatures: a) T ≈ 249 K, b) T = 247 K, c) T = 253 K, d) 245, labels indicate the contribution to the total surface area from each bin. A more detailed division is presented in e) Surface area concentration ratio and f) number fraction of particles for samples divided according to the size dependence of the pyroxene relative volume fraction presented in Panta et al. (2025).

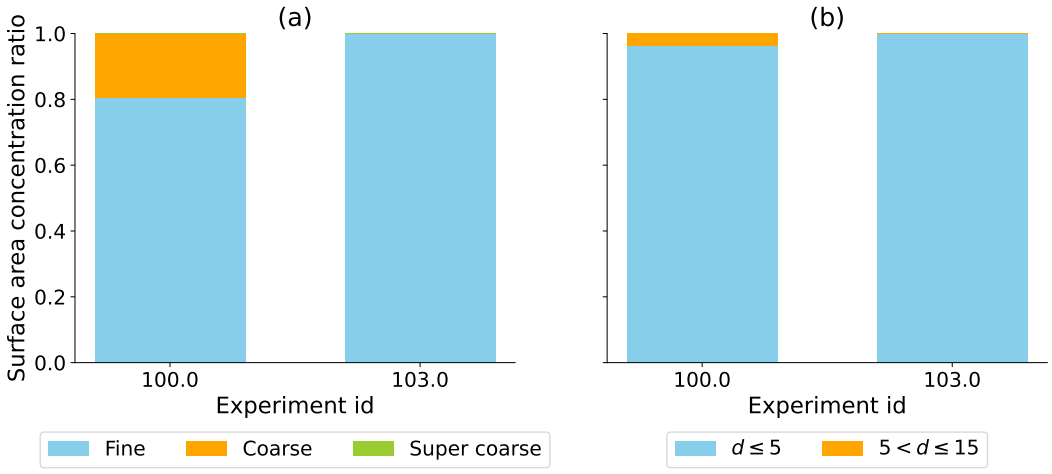


Figure 6.4.: Surface area concentration ratio for Iceland experiments in Steinke et al. (2011). Contribution of size ranges divided into (a) fine, coarse, and super-coarse particles, (b) $d \leq 5$ and $5 < d \leq 15$. Metrics computed according to information presented in Fig. 3 in Steinke et al. (2011). Exp 100 with a cut-off of 15 µm, and exp 103 with a cut-off of 5 µm.

7. Summary

Mineral dust particles are among the most abundant aerosol components in the atmosphere by mass. They are emitted from arid and semi-arid regions worldwide and can be transported over thousands of kilometers. During transport, mineral dust particle size distribution can extend up to tens of micrometers and interact with the atmosphere, influencing a wide range of processes, including the Earth's radiation budget, the hydrological cycle, and even human activities and health. One of the most important interactions is the ability of mineral dust to act as ice-nucleating particles (INPs). By facilitating the phase transition of water from liquid or vapor to ice, dust particles can alter cloud microphysical properties. Clouds are central to weather and Earth's energy balance, yet their representation and characterization remain major challenges in atmospheric science.

Extensive research has examined the efficiency and mechanisms by which mineral dust initiates ice formation, identifying key nucleation modes, such as immersion freezing, condensation freezing, deposition nucleation, and contact freezing, and developing parameterizations relating ice activity to dust source, temperature, and supersaturation. Nevertheless, significant uncertainties remain: results across studies often diverge, open questions persist, and there is ongoing debate about which theoretical frameworks most accurately describe these phenomena. Two issues are of particular importance and have received comparatively little attention. First, the relevance of high-latitude dust sources (e.g., Icelandic dust) as INPs in regional and global contexts remains insufficiently quantified. Second, the role of super-coarse and giant particles (diameters >10 μm) is not yet fully understood, since most past parameterizations were developed using narrow size distributions that largely excluded this fraction. Addressing these questions will improve our understanding of dust as INPs, help constrain their climatic impact, and ultimately lead to more accurate atmospheric and climate models.

Building on these knowledge gaps, this study aims to investigate the ice-nucleating activity of mineral dust particles ranging from submicrometer sizes to tens of micrometers in the immersion freezing mode, considering both low- and high-latitude dust sources. Furthermore, we test the results using the state-of-the-art numerical model ICON-ART, with a particular focus on mixed-phase clouds (MPCs), one of the most abundant and climatically relevant cloud types.

To achieve our objectives, we combined field campaigns and laboratory experiments involving international collaborations with researchers from different countries such as Germany, Spain, and France, and numerical simulations. Surface-level dust samples systematically collected during two previous field campaigns in Morocco and Iceland were used. Sample preparation was performed at CSIC, Spain. Ice nucleation experiments were conducted at the AIDA and mini AIDA (AIDAm) chamber, incorporating

specific modifications tailored to the larger size of our samples, as well as using the INSEKT freezing array technique. Data analysis and the development of new parameterizations were carried out using custom scripts, validated against published studies. Finally, the newly developed parameterizations were implemented in ICON-ART, with modifications to the source code to enable mineral dust source tagging, and the results were evaluated against observations.

More than 300 ice nucleation experiments were performed using the AIDA and AIDAm chambers, as well as the INSEKT technique, for Moroccan and Icelandic samples. The particle size distributions (PSDs) spanned more than three orders of magnitude, from 10^{-1} to 10^{2} µm.

The commonly used ice nucleation active site (INAS) density approach, which relates ice-nucleating activity to temperature by retaining only the linear term in a Taylor expansion of the exponential exponent, was tested. In this study, the calculation of surface area required for INAS was updated from the traditional assumption of spherical particles to a more accurate ellipsoidal shape. The frequent linear simplification assumes that INAS is constant across the size distribution and that the product between INAS and the surface area is much smaller than unity, making higher-order terms negligible. However, because our particles are significantly larger in diameter than those investigated in previous studies, this assumption might not hold.

To address this, we compared different metrics, including the discrete counterpart of the INAS density approach. We found that incorporating higher-order terms in the Taylor expansion and applying discrete or cumulative INAS formulations did not lead to significantly different results. Differences between approaches became more pronounced at lower temperatures, where nucleation activity is higher. Nevertheless, for almost all experiments performed in AIDA, AIDAm, and INSEKT, the discrepancies remained below 50%.

Two new immersion-freezing parameterizations were derived to describe the ice nucleation activity of low-latitude (Morocco) and high-latitude (Iceland) dust sources. In both cases, an exponential relationship between INAS density and temperature was observed, yielding the following parameterizations: $ln(n_s(T)) = 291.41 - 1.0885T$ and $ln(n_s(T)) = 207.85 - 0.7657T$ for Morocco and Iceland, respectively. Where n_s is the INAS density and T is the temperature in Kelvin. Additionally, the high repetition rate of AIDAm experiments with the same sample, drawn from AIDA, allowed us to confirm the residence time of particles in the AIDA chamber and demonstrated no dependence of the ice nucleation activity on time.

The Moroccan parameterization agreed with previous studies on samples of similar origin and mineralogy, whereas the Icelandic parameterization was approximately 1.5 orders of magnitude lower than previous results for dusts of comparable origin.

To investigate this discrepancy, we studied the dependence of INAS density on particle size. For Moroccan samples, no clear size dependence was found. For Icelandic samples, however, we observed a subtle dependence in which PSDs with larger contributions from particles smaller than 4 µm in size to the total surface area exhibited higher ice activity. This effect was attributed to the mineralogical composition

of the Icelandic samples, specifically their pyroxene content, in which it showed an inverse relationship between concentration by volume and particle size in our samples. Past studies have identified Pyroxene as one of the most active mineral groups in volcanic-origin dust.

Based on this finding, we proposed an "effective surface area" modification to the standard INAS approach, in which the sample surface area is scaled by a constant factor representing the proportion of the most active mineral(s) at each size. Applying this correction led to minimal changes (less than one order of magnitude) in the Moroccan parameterization, but increased the Icelandic parameterization by 1.5 orders of magnitude, bringing it into agreement with previous studies that employed narrower size distributions, where biases in the computed surface area have a smaller impact on the derived INAS values due to the inverse square relationship between these variables.

The implementation of the new parameterizations in ICON-ART in addition to the new dust source tagging technique showed that Icelandic dust was generally confined within the PBL and was not transported over long distances during June–August 2021. Consistent with the thermodynamic constraint on immersion freezing, activated INP concentrations (immersion mode) occur mainly above 600 hPa, and the proposed source-aware parameterizations yield a systematic reduction in INPs relative to the default scheme. By contrast, MPC properties showed only modest sensitivity to the parameterization choice, this can be explained because immersion-mode INPs rarely reached high concentrations for all tested cases. Even so, the new parameterizations produce a modest improvement in the CRE comparison with CERES: the model agrees better in SW CRE, while it substantially underestimates LW CRE relative to CERES.

In this work, the size range commonly considered in immersion-freezing nucleation experiments was extended toward larger particles; surface-area estimates were updated to represent more realistic dust shapes (ellipsoids); and the results were interpreted using mineralogical and size-dependence information, yielding a more robust characterization of the tested samples. The analysis of the mineralogical composition of samples from each source and the extended size distribution of our samples allowed us to evaluate a possible dependence of the ice nucleation activity on particle size and mineralogy. Despite the larger content of quartz in our Moroccan samples, the ice nucleation activity was higher and similar to that of feldspar which was present in a lower proportion, agreeing with previous studies on the loss in ice nucleation activity of quartz with time and exposure to air, as well as evidence that nucleation is often driven by the most active mineral present. Additionally, no dependence of ice nucleation activity on particle size was observed. Conversely, we conclude that a size dependence is present for Icelandic samples. Furthermore, the greatest disagreement for n_s with other studies was present at warmer temperatures, especially in the case of Iceland when considering the INSEKT experiments.

The experimental data and the fit presented for Moroccan samples agreed well with previous studies using samples of similar origin or mineralogy, reinforcing the understanding that one of the predominant factors for active sites and nucleation is the presence of ice-active mineralogical components in the samples. On this basis, an important conclusion of this study is that the validity of typical approximations

used in the calculation of $n_s(T)$ needs to be evaluated for samples including particles of a wide size range. When considering a polydisperse aerosol in which each particle acts as a CCN and subsequently nucleates, it is at the heart of the calculation of n_s that $n_s(T)$ can be assumed constant and independent of size. In the past, some studies have checked this condition (Steinke et al., 2011). However, the number size distributions considered were generally very narrow, not extending beyond a couple of µm, so that the particle properties did not vary strongly. However, it is known that particles larger than 10 µm in diameter (as previously discussed, many studies have not considered PSDs larger than that) can travel far from their source and interact with water and water vapor in the atmosphere (Ryder et al., 2019). Therefore, applying existing parameterizations to wider size distributions requires caution.

The difference in the dependence of mineralogy on size for samples of different sources also suggests a need for reconsideration of how ice nucleation on particles occurs. It is generally thought that larger particles will nucleate first, because they have a larger surface area, increasing the probability of finding highly active nucleation sites. However, in the scope of our results and previous ones (Jahn et al., 2019; Reicher et al., 2019), there is evidence that under certain conditions smaller particles nucleate first.

For summer 2021, model simulations indicated that Icelandic dust was generally confined within the planetary boundary layer and was rarely transported over long distances during early summer; only in August was Icelandic dust occasionally observed to reach 750 hPa. Thermodynamic constraints further limited the impact of Icelandic dust on immersion freezing: Icelandic dust rarely reached temperatures colder than about -10° C. Consistent with this, the immersion-mode INP concentration from Iceland was more than two orders of magnitude lower than contributions from other pathways (e.g., deposition nucleation or homogeneous freezing), even when dust columns were appreciable. Additionally, introducing source-aware, mineralogy/size-informed parameterizations (LLD_HLD and LLD_SHLD) had a large effect on INPs, reducing and spatially flattening the INP column burden over Iceland and nearby oceans. Only a modest effect on bulk MPC properties was found between parameterizations. Furthermore, the radiative comparisons improved: CRE agreement with CERES was strengthened, especially for SW CRE, whereas LW CRE remained underestimated by the model. Overall, the study showed that source-aware INP parameterizations improved radiative benchmarks (SW CRE) without substantially altering MPC characteristics (e.g., cloud phase, rain/snow rate) in early summer. To the best of our knowledge, this is one of the few studies to explicitly examine Icelandic dust and its impacts on MPCs via the immersion-freezing pathway.

8. Outlook

The present work provides new insights into the ice nucleation activity (INA) in the immersion freezing mode of mineral dust from both low-latitude dust (LLD) and high-latitude dust (HLD) sources. We investigated particle size distributions (PSDs) spanning three orders of magnitude, which allowed us to explore the dependence of INA on particle size and mineralogy. The results of this research are condensed into new parameterizations, developed with more than 300 ice-nucleating experiments using both wet and dry techniques, covering the temperature range from 242 to 255 K.

Although the developed parameterizations can be readily applied in models, further experiments are required to evaluate their validity outside the temperature range from which they were derived in order to fully establish their applicability in numerical simulations. Moreover, our samples were surface collected, highlighting the need to assess changes in INA during atmospheric transport. For example, our results provided evidence that under certain conditions smaller particles nucleate ice first. However, it remains uncertain whether this behavior persists under atmospheric conditions, where larger particles may interact more strongly with chemical or organic coatings, potentially reducing or enhancing their INA. Alternatively, under a cooling scenario, nucleation may begin with smaller particles that possess a higher density of active sites, followed by the activation of larger, coated particles, while intermediate-sized particles nucleate only at colder temperatures. Although there are ample studies on airborne and transported mineral dust INA for LLD (Atkinson et al., 2013; Harrison et al., 2022; Gao et al., 2024), considerably less is known about HLD sources such as Iceland (Sanchez-Marroquin et al., 2020), or about PSDs from both LLD and HLD sources that extend into the super-coarse and giant size ranges.

Another key aspect that future studies should address is the detailed mineralogical characterization of the tested samples. Certain minerals are known to dominate INA and thus drive the ice nucleation process. When larger particles are included, the probability of a shift in the mineralogical composition of the active sample fraction increases, which in turn may alter the INA. Furthermore, in some regions of the world, the mineralogical composition of emitted dust is highly variable, meaning that dust collected from a specific location may exhibit different INA than dust emitted nearby, as has been observed for Icelandic dust (Meinander et al., 2022).

In this context, the widely used INAS metric should be revised and applied with caution, ensuring that it remains constant across the size distribution.

Additionally, the implementation of source-tagged dust emission and INP parameterizations in ICON-ART provides a basis for more detailed regional studies. However, additional work is required to evaluate their performance against long-term in situ observations and satellite products. In this study, we

distinguished only two broad source categories: dust emitted from Iceland and dust from the rest of the world. This was a deliberate simplification designed to assess the regional relevance of Icelandic dust in comparison to external sources. To improve model capabilities, the source-tagging approach should be extended to include more regions (Shi et al., 2022), and not only to distinguish dust emissions but also to represent their mineralogical composition (Gonçalves Ageitos et al., 2023; Gómez Maqueo Anaya et al., 2024). Furthermore, the simulations presented here covered only a limited time period, focused on months historically associated with high emissions in Iceland (Meinander et al., 2022). Extending the simulated period would provide a broader perspective on dust dynamics, the most relevant INP sources and ice nucleation pathways, and their influence on cloud properties, the Earth's radiation budget, and high-latitude feedback processes.

9. Acknowledgments

I would like to thank my mom, Astrid, a constant inspiration for hard work, integrity, and dedication. I also thank my siblings, Nataly and Julian, who are always with me. I am grateful to Emilia for her companionship through good and difficult times, and for her understanding and support. I am also grateful to my friends Nicolás and David; despite the distance, they were always present during this process. Thanks to Hannah for always being thoughtful, for welcoming me and being the first person I met in Germany, and for her friendship. I thank my colleagues—Mega, Rumeng, Noel, Natalie, Andreas, and Lea—for the many good moments we shared in and out of the office. I thank my co-supervisor, Corinna, for always listening, for her kindness, giving room to new ideas, and guiding and refining them. I am deeply grateful to my supervisor, Martina. Thank you for believing in me; for your extraordinary attention to detail and tireless work; and for continually striving to improve every aspect of the research, the writing, and the presentations. Thank you for your guidance and listening to my ideas, and for creating an environment in which I could improve critical thinking and propose new directions.

A. ICON-ART Modifications for Dust Source Tagging

This section shows the modifications made to the files: `tracers_dustrad.xml` (A.1), `modes_dustrad.xml` (A.2), `aero_emiss_dustrad.xml` (A.3), `diagnostics_dust.xml` (A.4), to add new tracers, termed "dustx_iceland" where x stands for a, b, and c (different dust modes). The unmodified files are available in the ART wiki.

Listing A.1: Modified tracers_dustrad.xml file to include new tracers.

```
<?xml version="1.0" encoding="UTF-8"?>
<!DOCTYPE tracers SYSTEM "tracers.dtd">

<tracers>
 <aerosol id="dust">
    <moment type="int">3</moment>
    <mode type="char">dusta,dustb,dustc</mode>
    <label type="char">dusta,dustb,dustc</label>
    <sol type="real">0.</sol>
    <mol_weight type="real">50.00E-3</mol_weight>
    <rho type="real">2.650E3</rho>
    <unit type="char">mug kg-1</unit>
    <transport type="char">hadv52aero</transport>
    <iconv type="int">1</iconv>
    <iturb type="int">1</iturb>
 </aerosol>
 <aerosol id="dust_iceland">
    <moment type="int">3</moment>
    <mode type="char">dusta_iceland,dustb_iceland,dustc_iceland</mode>
    <label type="char">dusta_iceland,dustb_iceland,dustc_iceland</label>
    <sol type="real">0.</sol>
    <mol_weight type="real">50.00E-3</mol_weight>
    <rho type="real">2.650E3</rho>
    <unit type="char">mug kg-1</unit>
    <transport type="char">hadv52aero</transport>
    <iconv type="int">1</iconv>
    <iturb type="int">1</iturb>
 </aerosol>
<aerosol id="nmb">
```

```
    <moment type="int">0</moment>
    <mode type="char">dusta,dustb,dustc</mode>
    <label type="char">dusta0,dustb0,dustc0</label>
    <sol type="real">1.0</sol>
    <mol_weight type="real">50.00E-3</mol_weight>
    <rho type="real">2.650E3</rho>
    <unit type="char">kg-1</unit>
    <transport type="char">hadv52aero</transport>
    <iconv type="int">1</iconv>
    <iturb type="int">1</iturb>
  </aerosol>
  <aerosol id="nmb_iceland">
    <moment type="int">0</moment>
    <mode type="char">dusta_iceland,dustb_iceland,dustc_iceland</mode>
    <label type="char">dusta0_iceland,dustb0_iceland,dustc0_iceland</label>
    <sol type="real">1.0</sol>
    <mol_weight type="real">50.00E-3</mol_weight>
    <rho type="real">2.650E3</rho>
    <unit type="char">kg-1</unit>
    <transport type="char">hadv52aero</transport>
    <iconv type="int">1</iconv>
    <iturb type="int">1</iturb>
  </aerosol>
</tracers>
```

Listing A.2: Modified modes_dustrad.xml file to include new tracers.

```
<?xml version="1.0" encoding="UTF-8"?>
<!DOCTYPE modes SYSTEM "modes.dtd">

<modes>
  <aerosol id="dusta_iceland">
    <kind   type="char">2mom</kind>
    <d_gn   type="real">6.445E-7</d_gn>
    <d_gm   type="real">1.500E-6</d_gm>
    <sigma_g type="real">1.700E+0</sigma_g>
    <rho    type="real">2.650E+3</rho>
    <condensation type="int">0</condensation>
    <icoag type="int">0</icoag>
    <ikoehler type="int">1</ikoehler>
    <ifreeze type="int">1</ifreeze>
    <lut_optics type="char" cvar_dia="true">dust_a</lut_optics>
```

```
</aerosol>
<aerosol id="dustb_iceland">
  <kind   type="char">2mom</kind>
  <d_gn   type="real">3.454E-6</d_gn>
  <d_gm   type="real">6.700E-6</d_gm>
  <sigma_g type="real">1.600E+0</sigma_g>
  <rho    type="real">2.650E+3</rho>
  <condensation type="int">0</condensation>
  <icoag type="int">0</icoag>
  <ikoehler type="int">1</ikoehler>
  <ifreeze type="int">1</ifreeze>
  <lut_optics type="char" cvar_dia="true">dust_b</lut_optics>
</aerosol>
<aerosol id="dustc_iceland">
  <kind   type="char">2mom</kind>
  <d_gn   type="real">8.672E-6</d_gn>
  <d_gm   type="real">1.420E-5</d_gm>
  <sigma_g type="real">1.500E+0</sigma_g>
  <rho    type="real">2.650E+3</rho>
  <condensation type="int">0</condensation>
  <icoag type="int">0</icoag>
  <ikoehler type="int">1</ikoehler>
  <ifreeze type="int">1</ifreeze>
  <lut_optics type="char" cvar_dia="true">dust_c</lut_optics>
</aerosol>
<aerosol id="dusta">
  <kind   type="char">2mom</kind>
  <d_gn   type="real">6.445E-7</d_gn>
  <d_gm   type="real">1.500E-6</d_gm>
  <sigma_g type="real">1.700E+0</sigma_g>
  <rho    type="real">2.650E+3</rho>
  <condensation type="int">0</condensation>
  <icoag type="int">0</icoag>
  <ikoehler type="int">1</ikoehler>
  <ifreeze type="int">1</ifreeze>
  <lut_optics type="char" cvar_dia="true">dust_a</lut_optics>
</aerosol>
<aerosol id="dustb">
  <kind   type="char">2mom</kind>
  <d_gn   type="real">3.454E-6</d_gn>
  <d_gm   type="real">6.700E-6</d_gm>
  <sigma_g type="real">1.600E+0</sigma_g>
```

```
    <rho     type="real">2.650E+3</rho>
    <condensation type="int">0</condensation>
    <icoag type="int">0</icoag>
    <ikoehler type="int">1</ikoehler>
    <ifreeze type="int">1</ifreeze>
    <lut_optics type="char" cvar_dia="true">dust_b</lut_optics>
  </aerosol>
  <aerosol id="dustc">
    <kind    type="char">2mom</kind>
    <d_gn    type="real">8.672E-6</d_gn>
    <d_gm    type="real">1.420E-5</d_gm>
    <sigma_g type="real">1.500E+0</sigma_g>
    <rho     type="real">2.650E+3</rho>
    <condensation type="int">0</condensation>
    <icoag type="int">0</icoag>
    <ikoehler type="int">1</ikoehler>
    <ifreeze type="int">1</ifreeze>
    <lut_optics type="char" cvar_dia="true">dust_c</lut_optics>
  </aerosol>
</modes>
```

Listing A.3: Modified aero_emiss_dustrad.xml file to include new tracers.

```
<?xml version="1.0" encoding="UTF-8"?>
<!DOCTYPE tracers SYSTEM "aero_emiss.dtd">

<emiss>
 <routine id="dust">
    <nmodes type="int">3</nmodes>
    <d_g0_1 type="real">6.445E-7</d_g0_1>
    <d_g3_1 type="real">1.500E-6</d_g3_1>
    <sigma_g_1 type="real">1.700E+0</sigma_g_1>
    <d_g0_2 type="real">3.454E-6</d_g0_2>
    <d_g3_2 type="real">6.700E-6</d_g3_2>
    <sigma_g_2 type="real">1.600E+0</sigma_g_2>
    <d_g0_3 type="real">8.672E-6</d_g0_3>
    <d_g3_3 type="real">1.420E-5</d_g3_3>
    <sigma_g_3 type="real">1.500E+0</sigma_g_3>
    <rho type="real">2.650E3</rho>
    <substances type="char">dust_iceland</substances>
  </routine>
  <routine id="dust">
```

```
    <nmodes type="int">3</nmodes>
    <d_g0_1 type="real">6.445E-7</d_g0_1>
    <d_g3_1 type="real">1.500E-6</d_g3_1>
    <sigma_g_1 type="real">1.700E+0</sigma_g_1>
    <d_g0_2 type="real">3.454E-6</d_g0_2>
    <d_g3_2 type="real">6.700E-6</d_g3_2>
    <sigma_g_2 type="real">1.600E+0</sigma_g_2>
    <d_g0_3 type="real">8.672E-6</d_g0_3>
    <d_g3_3 type="real">1.420E-5</d_g3_3>
    <sigma_g_3 type="real">1.500E+0</sigma_g_3>
    <rho type="real">2.650E3</rho>
    <substances type="char">dust</substances>
  </routine>
</emiss>
```

Listing A.4: Modified diagnostics_dust.xml file to include new tracers.

```
<?xml version="1.0" encoding="UTF-8"?>
<!DOCTYPE diagnostics SYSTEM "diagnostics.dtd">
<diagnostics>
  <aerosol id="acc_drydepo">
    <tracername_list type="char">dusta,dustb,dustc,dusta_iceland,dustb_iceland,
        dustc_iceland</tracername_list>
    <parameterNumber_list type="char">192,192,192,192,192,192</parameterNumber_list>
    <productDefinitionTemplate_list type="char">67,67,67,67,67,67</
        productDefinitionTemplate_list>
    <typeOfStatisticalProcessing type="int">1</typeOfStatisticalProcessing>
    <bitsPerValue type="int">32</bitsPerValue>
    <typeOfDistributionFunction type="int">8</typeOfDistributionFunction>
    <numberOfModeOfDistribution type="int">3</numberOfModeOfDistribution>
    <numberOfDistributionFunctionParameters type="int">2</
        numberOfDistributionFunctionParameters>
    <scaledValueOfDistributionFunctionParameter_1 type="int">1700</
        scaledValueOfDistributionFunctionParameter_1>
    <scaleFactorOfDistributionFunctionParameter_1 type="int">3</
        scaleFactorOfDistributionFunctionParameter_1>
    <scaledValueOfDistributionFunctionParameter_2 type="int">2650</
        scaledValueOfDistributionFunctionParameter_2>
    <scaleFactorOfDistributionFunctionParameter_2 type="int">0</
        scaleFactorOfDistributionFunctionParameter_2>
  </aerosol>
  <aerosol id="acc_sedim">
```

```
  <tracername_list type="char">dusta,dustb,dustc,dusta0,dustb0,dustc0,dusta_iceland,
      dustb_iceland,dustc_iceland,dusta0_iceland,dustb0_iceland,dustc0_iceland</
      tracername_list>
  <parameterNumber_list type="char">194,194,194,195,195,195,194,194,194,195,195,195</
      parameterNumber_list>
  <productDefinitionTemplate_list type="char">67,67,67,67,67,67,67,67,67,67,67,67</
      productDefinitionTemplate_list>
  <typeOfStatisticalProcessing type="int">1</typeOfStatisticalProcessing>
  <bitsPerValue type="int">32</bitsPerValue>
  <typeOfDistributionFunction type="int">8</typeOfDistributionFunction>
  <numberOfModeOfDistribution type="int">3</numberOfModeOfDistribution>
  <numberOfDistributionFunctionParameters type="int">2</
      numberOfDistributionFunctionParameters>
  <scaledValueOfDistributionFunctionParameter_1 type="int">1700</
      scaledValueOfDistributionFunctionParameter_1>
  <scaleFactorOfDistributionFunctionParameter_1 type="int">3</
      scaleFactorOfDistributionFunctionParameter_1>
  <scaledValueOfDistributionFunctionParameter_2 type="int">2650</
      scaledValueOfDistributionFunctionParameter_2>
  <scaleFactorOfDistributionFunctionParameter_2 type="int">0</
      scaleFactorOfDistributionFunctionParameter_2>
</aerosol>
<aerosol id="acc_wetdepo_rrsfc">
  <tracername_list type="char">dusta,dustb,dustc,dusta0,dustb0,dustc0,dusta_iceland,
      dustb_iceland,dustc_iceland,dusta0_iceland,dustb0_iceland,dustc0_iceland</
      tracername_list>
  <parameterNumber_list type="char">196,196,196,197,197,197,196,196,196,197,197,197</
      parameterNumber_list>
  <productDefinitionTemplate_list type="char">67,67,67,67,67,67,67,67,67,67,67,67</
      productDefinitionTemplate_list>
  <typeOfStatisticalProcessing type="int">1</typeOfStatisticalProcessing>
  <bitsPerValue type="int">32</bitsPerValue>
  <typeOfDistributionFunction type="int">8</typeOfDistributionFunction>
  <numberOfModeOfDistribution type="int">3</numberOfModeOfDistribution>
  <numberOfDistributionFunctionParameters type="int">2</
      numberOfDistributionFunctionParameters>
  <scaledValueOfDistributionFunctionParameter_1 type="int">1700</
      scaledValueOfDistributionFunctionParameter_1>
  <scaleFactorOfDistributionFunctionParameter_1 type="int">3</
      scaleFactorOfDistributionFunctionParameter_1>
  <scaledValueOfDistributionFunctionParameter_2 type="int">2650</
      scaledValueOfDistributionFunctionParameter_2>
```

```
  <scaleFactorOfDistributionFunctionParameter_2 type="int">0</
      scaleFactorOfDistributionFunctionParameter_2>
</aerosol>
<aerosol id="emiss">
  <tracername_list type="char">dusta,dustb,dustc,dusta_iceland,dustb_iceland,
      dustc_iceland</tracername_list>
  <parameterNumber_list type="char">3,3,3,3,3,3</parameterNumber_list>
  <productDefinitionTemplate_list type="char">57,57,57,57,57,57</
      productDefinitionTemplate_list>
  <bitsPerValue type="int">32</bitsPerValue>
  <typeOfDistributionFunction type="int">8</typeOfDistributionFunction>
  <numberOfModeOfDistribution type="int">3</numberOfModeOfDistribution>
  <numberOfDistributionFunctionParameters type="int">2</
      numberOfDistributionFunctionParameters>
  <scaledValueOfDistributionFunctionParameter_1 type="int">1700</
      scaledValueOfDistributionFunctionParameter_1>
  <scaleFactorOfDistributionFunctionParameter_1 type="int">3</
      scaleFactorOfDistributionFunctionParameter_1>
  <scaledValueOfDistributionFunctionParameter_2 type="int">2650</
      scaledValueOfDistributionFunctionParameter_2>
  <scaleFactorOfDistributionFunctionParameter_2 type="int">0</
      scaleFactorOfDistributionFunctionParameter_2>
</aerosol>
<aerosol id="acc_emiss">
  <tracername_list type="char">dusta,dustb,dustc,dusta_iceland,dustb_iceland,
      dustc_iceland</tracername_list>
  <parameterNumber_list type="char">3,3,3,3,3,3</parameterNumber_list>
  <productDefinitionTemplate_list type="char">67,67,67,67,67,67</
      productDefinitionTemplate_list>
  <typeOfStatisticalProcessing type="int">1</typeOfStatisticalProcessing>
  <bitsPerValue type="int">32</bitsPerValue>
  <typeOfDistributionFunction type="int">8</typeOfDistributionFunction>
  <numberOfModeOfDistribution type="int">3</numberOfModeOfDistribution>
  <numberOfDistributionFunctionParameters type="int">2</
      numberOfDistributionFunctionParameters>
  <scaledValueOfDistributionFunctionParameter_1 type="int">1700</
      scaledValueOfDistributionFunctionParameter_1>
  <scaleFactorOfDistributionFunctionParameter_1 type="int">3</
      scaleFactorOfDistributionFunctionParameter_1>
  <scaledValueOfDistributionFunctionParameter_2 type="int">2650</
      scaledValueOfDistributionFunctionParameter_2>
```

```
    <scaleFactorOfDistributionFunctionParameter_2 type="int">0</
        scaleFactorOfDistributionFunctionParameter_2>
  </aerosol>
</diagnostics>
```

The following corresponds to the changes made to the function "art_emission_dust" to allow dust emission only for Iceland and for the rest of the world without Iceland.

Listing A.5: Modification to function "art_emission_dust".

```
pos = INDEX(namesmode, ',')
IF (pos > 0) THEN
  shortname = namesmode(1:pos-1)
ELSE
  shortname = TRIM(namesmode)
ENDIF

masked_value = 1.0_wp

DO i = istart, iend
  clat = p_patch%cells%center(i,jb)%lat ! obtaining lat and lon related with the cell
  clon = p_patch%cells%center(i,jb)%lon

  IF (INDEX(shortname, "iceland") /= 0) THEN ! if the tracer is Iceland
    IF (.NOT.(clat >= 63.0*(3.1415927_wp/180.0_wp) .AND. clat <= 67.0*(3.1415927_wp
        /180.0_wp) .AND. &
             clon >= -25.0*(3.1415927_wp/180.0_wp) .AND. clon <= -15.0*(3.1415927_wp
                /180.0_wp))) THEN
      masked_value = 0.0_wp ! no emission
    ELSE
      masked_value = 1.0_wp
    ENDIF
  ELSE ! tracer corresponds to the world
    IF (.NOT.(clat >= 63.0*(3.1415927_wp/180.0_wp) .AND. clat <= 67.0*(3.1415927_wp
        /180.0_wp) .AND. &
              clon >= -25.0*(3.1415927_wp/180.0_wp) .AND. clon <= -15.0*(3.1415927_wp
                 /180.0_wp))) THEN
      masked_value = 1.0_wp ! emission for rest of world
    ELSE
      masked_value = 0.0_wp ! no emission for Iceland
    ENDIF
  ENDIF ...
```

B. Additional Modifications to ART Subroutines for New Tracers

This appendix documents modifications to the ART ice-nucleation subroutines to include new, source-tagged tracers. It is important to mention that after running the simulations and analyzing the output fields, it was found that the dust tracers exhibited non-numerical values near the surface. Further debugging and feedback from the ICON-ART gatekeeper revealed that the combination of iart_aci_cold > 0 and inwp_gscp = 6 (two-moment scheme) is not fully integrated from ART into the main ICON branch. The main changes to implement the newly developed parameterizations into the ART submodule were required in the subroutine `art_nuc_cold_interface` as well as in the associated subroutines and functions it calls. In general terms, these modifications extend the number of aerosol cases handled by the routines. At present, the standard implementation is restricted to three cases related to each mode, labeled "dusta", "dustb", and "dustc". In addition, a new case is added to the parameterization selection. Currently, ART provides five available options, which are chosen via the namelist variable iart_aci_cold. The new case integrates the parameterizations developed in this study together with their corresponding diagnostic output variables.

C. J-WADI field campaign

The Jordan Wind erosion And Dust Investigation (J-WADI) field measurement campaign was conducted in Wadi Rum, Jordan for 2 months, from September to October 2022. The aim of the J-WADI campaign was to advance our understanding of the particle size and mineralogical composition of the emitted dust and their dependence on the parent soil and meteorological composition. J-WADI was co-organized between the ERC Consolidator Grant FRAGMENT (FRontiers in dust minerAloGical coMposition and its Effects upoN climaTe) at the Barcelona Supercomputing Center (BSC) and the Helmholtz Young Investigator Group "A big unknown in the climate impact of atmospheric aerosol: Mineral soil dust" at KIT's Institute of Meteorology and Climate Research Department Troposphere Research in collaboration with the University of Jordan.

The main measurement site was located at 29° 44'21"N, 35° 22'56"E. The area is characterized by a flat, open landscape surrounded by hills smaller than 100 m in height, forming a wide opening toward the predominant wind direction. The site is also subject to occasional flooding during heavy rainfall periods, and lacks significant surface roughness features. The choice of location and campaign period was guided by a combination of remote sensing data, on-site inspection, and local expertise. Scientific and practical considerations, such as expected dust emissions, accessibility, and logistical constraints, were also taken into account.

The setup of the site is presented in Fig C.1 (reproduced from Meyer et al. (2026)) and was similar to previous FRAGMENT campaigns in Iceland and Morocco (González-Flórez et al., 2022; Dupont et al., 2024a), but with the addition of new instruments to measure super-coarse and giant dust and atmospheric turbulence.

The main tasks I carried out during the campaign included contributing to unloading the instruments from the transport container, installation and setup, regular instrument checks, and finally dismounting and reloading the instruments for transport back. For routine maintenance and data acquisition, I visited the measurement site daily to perform standard checks. Once the instruments were calibrated and fully operational, the work focused on daily inspections and data collection from 3 mobile meteorological towers (MM1, Fig C.1a and MM3,Fig C.1c), exchanging INSEKT filters, and collecting samples from saltation sediment samplers (Fig C.1b).

Furthermore, additional analyses building on these data were included in Dupont et al. (2024a), I am co-author. However, as equipment and samples arrived from Jordan after the MICOS campaign, we could not test samples from Jordan.

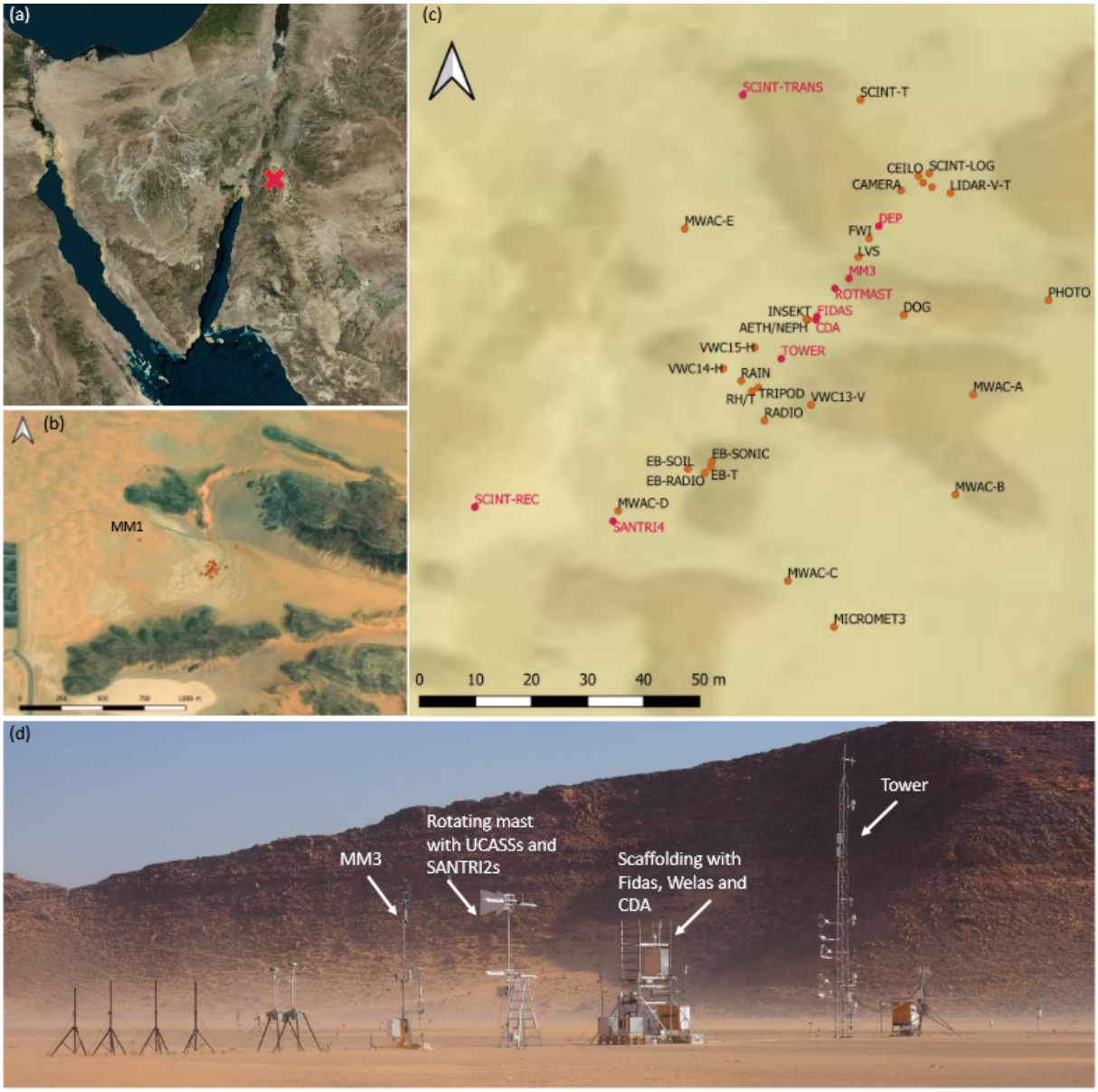


Figure C.1.: Field location and set-up. (a) Background image from Bing maps with the field site marked with a pink cross, (b) topographic map, field set-up, and surrounding of J-WADI, (c) set-up at the measurement site with the instruments used marked in pink (SCINTTRANS/-REC = scintillometer transmitter/receiver, ROTMAST = rotating mast, DEP = deposition sampler), (d) photo of the site center including most instruments used in this study in their field deployment. Background map copyright (a) ©Microsoft, (b) and (c) Esri, Maxar, Earthstar Geographics, and the GIS User Community. Reproduced from Meyer et al. (2026).

Bibliography

Ackerman, S. A. and H. Chung, 1992: Radiative effects of airborne dust on regional energy budgets at the top of the atmosphere. *Journal of Applied Meteorology and Climatology*, **31 (2)**, 223–233.

Adebiyi, A., J. F. Kok, B. J. Murray, C. L. Ryder, J.-B. W. Stuut, R. A. Kahn, P. Knippertz, P. Formenti, N. M. Mahowald, C. P. García-Pando, et al., 2023: A review of coarse mineral dust in the earth system. *Aeolian Research*, **60**, 100 849.

Alfaro, S. C. and L. Gomes, 2001: Modeling mineral aerosol production by wind erosion: Emission intensities and aerosol size distributions in source areas. *Journal of Geophysical Research: Atmospheres*, **106 (D16)**, 18 075–18 084.

Arnalds, O., P. Dagsson-Waldhauserova, and H. Olafsson, 2016: The icelandic volcanic aeolian environment: Processes and impacts—a review. *Aeolian Research*, **20**, 176–195.

Arnalds, O., H. Olafsson, and P. Dagsson-Waldhauserova, 2014: Quantification of iron-rich volcanogenic dust emissions and deposition over the ocean from icelandic dust sources. *Biogeosciences*, **11 (23)**, 6623–6632.

Ashrafi, K., M. S. Motlagh, and S. E. Neyestani, 2017: Dust storms modeling and their impacts on air quality and radiation budget over iran using wrf-chem. *Air Quality, Atmosphere & Health*, **10 (9)**, 1059–1076.

Atkinson, J. D., B. J. Murray, M. T. Woodhouse, T. F. Whale, K. J. Baustian, K. S. Carslaw, S. Dobbie, D. O'Sullivan, and T. L. Malkin, 2013: The importance of feldspar for ice nucleation by mineral dust in mixed-phase clouds. *Nature*, **498 (7454)**, 355–358.

Baldo, C., P. Formenti, C. Di Biagio, G. Lu, C. Song, M. Cazaunau, E. Pangui, J.-F. Doussin, P. Dagsson-Waldhauserova, O. Arnalds, et al., 2023: Complex refractive index and single scattering albedo of icelandic dust in the shortwave spectrum. *EGUsphere*, 1–42.

Barr, S. L., B. Wyld, J. B. McQuaid, R. R. Neely III, and B. J. Murray, 2023: Southern Alaska as a source of atmospheric mineral dust and ice-nucleating particles. *Science Advances*, **9 (33)**, eadg3708.

Bechtold, P., M. Köhler, T. Jung, F. Doblas-Reyes, M. Leutbecher, M. J. Rodwell, F. Vitart, and G. Balsamo, 2008: Advances in simulating atmospheric variability with the ecmwf model: From synoptic to

decadal time-scales. *Quarterly Journal of the Royal Meteorological Society: A journal of the atmospheric sciences, applied meteorology and physical oceanography*, **134 (634)**, 1337–1351.

Beneduce, C., D. E. Pinto, L. Rovigatti, F. Romano, P. Šulc, F. Sciortino, and J. Russo, 2025: Falsifiability test for classical nucleation theory. *Physical Review Letters*, **134 (14)**, 148 201.

Bhattu, D. and S. Tripathi, 2015: Ccn closure study: Effects of aerosol chemical composition and mixing state. *Journal of Geophysical Research: Atmospheres*, **120 (2)**, 766–783.

Bohren, C. F. and D. R. Huffman, 2008: *Absorption and scattering of light by small particles*. John Wiley & Sons.

Boose, Y., A. Welti, J. Atkinson, F. Ramelli, A. Danielczok, H. G. Bingemer, M. Plötze, B. Sierau, Z. A. Kanji, and U. Lohmann, 2016: Heterogeneous ice nucleation on dust particles sourced from nine deserts worldwide–part 1: Immersion freezing. *Atmospheric Chemistry and Physics*, **16 (23)**, 15 075–15 095.

Bristow, C. S., K. A. Hudson-Edwards, and A. Chappell, 2010: Fertilizing the amazon and equatorial atlantic with west african dust. *Geophysical Research Letters*, **37 (14)**.

Broadley, S., B. Murray, R. Herbert, J. Atkinson, S. Dobbie, T. Malkin, E. Condliffe, and L. Neve, 2012: Immersion mode heterogeneous ice nucleation by an illite rich powder representative of atmospheric mineral dust. *Atmospheric Chemistry and Physics*, **12 (1)**, 287–307.

Bullard, J. E., M. Baddock, T. Bradwell, J. Crusius, E. Darlington, D. Gaiero, S. Gassó, G. Gisladottir, R. Hodgkins, R. McCulloch, et al., 2016: High-latitude dust in the earth system. *Reviews of Geophysics*, **54 (2)**, 447–485.

Burrows, S. M., C. S. McCluskey, G. Cornwell, I. Steinke, K. Zhang, B. Zhao, M. Zawadowicz, A. Raman, G. Kulkarni, S. China, et al., 2022: Ice-nucleating particles that impact clouds and climate: Observational and modeling research needs. *Reviews of Geophysics*, **60 (2)**, e2021RG000 745.

Ceppi, P. and P. Nowack, 2021: Observational evidence that cloud feedback amplifies global warming. *Proceedings of the National Academy of Sciences*, **118 (30)**, e2026290 118.

Chen, J.-P., A. Hazra, and Z. Levin, 2008: Parameterizing ice nucleation rates using contact angle and activation energy derived from laboratory data. *Atmospheric Chemistry and Physics*, **8 (24)**, 7431–7449.

Chesler, A., D. Winski, K. Kreutz, B. Koffman, E. Osterberg, D. Ferris, Z. Thundercloud, J. Mohan, J. Cole-Dai, M. Wells, et al., 2022: Non-spherical microparticle shape in antarctica during the last glacial period affects dust volume-related metrics. *Climate of the Past Discussions*, **2022**, 1–24.

Coopman, Q. and I. Tan, 2023: Characterization of the spatial distribution of the thermodynamic phase within mixed-phase clouds using satellite observations. *Geophysical Research Letters*, **50 (24)**, e2023GL104 977.

Cotton, R., S. Benz, P. Field, O. Möhler, and M. Schnaiter, 2007: A numerical test-bed for detailed ice nucleation studies in the aida cloud simulation chamber. *Atmospheric Chemistry and Physics*, **7 (1)**, 243–256.

Cvetkovic, B., P. Dagsson-Waldhauserová, S. Petkovic, Ó. Arnalds, F. Madonna, E. Proestakis, A. Gkikas, A. Vukovic Vimic, G. Pejanovic, M. Rosoldi, et al., 2022: Fully dynamic high–resolution model for dispersion of icelandic airborne mineral dust. *Atmosphere*, **13 (9)**, 1345.

DeMott, P. J., A. J. Prenni, G. R. McMeeking, R. C. Sullivan, M. D. Petters, Y. Tobo, M. Niemand, O. Möhler, J. R. Snider, Z. Wang, et al., 2015: Integrating laboratory and field data to quantify the immersion freezing ice nucleation activity of mineral dust particles. *Atmospheric Chemistry and Physics*, **15 (1)**, 393–409.

Denjean, C., F. Cassola, A. Mazzino, S. Triquet, S. Chevaillier, N. Grand, T. Bourrianne, G. Momboisse, K. Sellegri, A. Schwarzenbock, et al., 2016: Size distribution and optical properties of mineral dust aerosols transported in the western mediterranean. *Atmospheric Chemistry and Physics*, **16 (2)**, 1081–1104.

Derbyshire, E., 2007: Natural minerogenic dust and human health. *AMBIO: A Journal of the Human Environment*, **36 (1)**, 73–77.

Deutscher Wetterdienst (DWD), 2024: Icon tutorial 2024. `https://www.dwd.de/DE/leistungen/nwv_icon_tutorial/pdf_einzelbaende/icon_tutorial2024.html`, accessed: 23 September 2025.

Dipankar, A., B. Stevens, R. Heinze, C. Moseley, G. Zängl, M. Giorgetta, and S. Brdar, 2015: Large eddy simulation using the general circulation model icon. *Journal of Advances in Modeling Earth Systems*, **7 (3)**, 963–986.

Doelling, D. R., N. G. Loeb, D. F. Keyes, M. L. Nordeen, D. Morstad, C. Nguyen, B. A. Wielicki, D. F. Young, and M. Sun, 2013: Geostationary enhanced temporal interpolation for ceres flux products. *Journal of Atmospheric and Oceanic Technology*, **30 (6)**, 1072–1090.

Dupont, S., M. Klose, M. Irvine, C. González-Flórez, A. Alastuey, J.-M. Bonnefond, P. Dagsson-Waldhauserova, A. Gonzalez-Romero, T. Hussein, E. Lamaud, et al., 2024a: Impact of dust source patchiness on the existence of a constant dust flux layer during aeolian erosion events. *Journal of geophysical research: Atmospheres*, **129 (12)**, e2023JD040 657.

Dupont, S., M. Klose, M. R. Irvine, C. González-Florez, A. Alastuey, J.-M. Bonnefond, P. Dagsson-Waldhauserova, A. Gonzalez-Romero, T. Hussein, E. Lamaud, H. Meyer, A. Panta, X. Querol, K. Schepanski, S. Vergara Palacio, A. Wieser, J. Yus-DÃez, K. Kandler, and C. Pérez García-Pando, 2024b: Impact of dust source patchiness on the existence of a constant dust flux layer during aeolian erosion events. *J. Geophys. Res. Atmos*, **129 (12)**, e2023JD040 657, URL `https://agupubs.onlinelibrary.wiley.com/doi/abs/10.1029/2023JD040657`.

Evans, L. and J. Lane, 1973: Line tension and ice nucleation theory. *Journal of Atmospheric Sciences*, **30 (2)**, 326–330.

Fajber, R., A. Donohoe, S. Ragen, K. C. Armour, and P. J. Kushner, 2023: Atmospheric heat transport is governed by meridional gradients in surface evaporation in modern-day earth-like climates. *Proceedings of the National Academy of Sciences*, **120 (25)**, e2217202 120.

Field, P. R., R. P. Lawson, P. R. Brown, G. Lloyd, C. Westbrook, D. Moisseev, A. Miltenberger, A. Nenes, A. Blyth, T. Choularton, et al., 2017: Secondary ice production: Current state of the science and recommendations for the future. *Meteorological Monographs*, **58**, 7–1.

Ford, I., 2004: Statistical mechanics of nucleation: a review. *Proceedings of the Institution of Mechanical Engineers, Part C: Journal of Mechanical Engineering Science*, **218 (8)**, 883–899.

Gao, K., F. Vogel, R. Foskinis, S. Vratolis, M. I. Gini, K. Granakis, A.-C. Billault-Roux, P. Georgakaki, O. Zografou, P. Fetfatzis, et al., 2024: Biological and dust aerosols as sources of ice-nucleating particles in the eastern mediterranean: source apportionment, atmospheric processing and parameterization. *Atmospheric Chemistry and Physics*, **24 (17)**, 9939–9974.

Gassmann, A. and H.-J. Herzog, 2008: Towards a consistent numerical compressible non-hydrostatic model using generalized hamiltonian tools. *Quarterly Journal of the Royal Meteorological Society*, **134 (635)**, 1597–1613.

Georgakopoulou, V. E., C. Taskou, A. Diamanti, D. Beka, P. Papalexis, N. Trakas, and D. A. Spandidos, 2024: Saharan dust and respiratory health: Understanding the link between airborne particulate matter and chronic lung diseases. *Experimental and Therapeutic Medicine*, **28 (6)**, 460.

Giles, D. M., B. N. Holben, T. F. Eck, A. Sinyuk, A. Smirnov, I. Slutsker, R. Dickerson, A. Thompson, and J. Schafer, 2012: An analysis of aeronet aerosol absorption properties and classifications representative of aerosol source regions. *Journal of Geophysical Research: Atmospheres*, **117 (D17)**.

Ginoux, P., J. M. Prospero, T. E. Gill, N. C. Hsu, and M. Zhao, 2012: Global-scale attribution of anthropogenic and natural dust sources and their emission rates based on MODIS Deep Blue aerosol products. *Reviews of Geophysics*, **50 (3)**, RG3005.

Gómez Maqueo Anaya, S., D. Althausen, M. Faust, H. Baars, B. Heinold, J. Hofer, I. Tegen, A. Ansmann, R. Engelmann, A. Skupin, et al., 2024: The implementation of dust mineralogy in cosmo5. 05-muscat. *Geoscientific Model Development*, **17 (3)**, 1271–1295.

Gonçalves Ageitos, M., V. Obiso, R. L. Miller, O. Jorba, M. Klose, M. Dawson, Y. Balkanski, J. Perlwitz, S. Basart, E. Di Tomaso, et al., 2023: Modeling dust mineralogical composition: sensitivity to soil mineralogy atlases and their expected climate impacts. *Atmospheric Chemistry and Physics*, **23 (15)**, 8623–8657.

González-Flórez, C., M. Klose, A. Alastuey, S. Dupont, J. Escribano, V. Etyemezian, A. Gonzalez-Romero, Y. Huang, K. Kandler, G. Nikolich, et al., 2022: Insights into the size-resolved dust emission from field measurements in the moroccan sahara. *Atmospheric Chemistry & Physics Discussions*.

González-Romero, A., C. González-Flórez, A. Panta, J. Yus-Díez, P. Córdoba, A. Alastuey, N. Moreno, K. Kandler, M. Klose, R. N. Clark, et al., 2024: Probing iceland's dust-emitting sediments: Particle size distribution, mineralogy, cohesion, fe mode of occurrence, and reflectance spectra signatures. *EGUsphere*, **2024**, 1–49.

González-Romero, A., C. González-Florez, A. Panta, J. Yus-Díez, C. Reche, P. Córdoba, A. Alastuey, K. Kandler, M. Klose, C. Baldo, et al., 2023: Variability in grain size, mineralogy, and mode of occurrence of fe in surface sediments of preferential dust-source inland drainage basins: The case of the lower drâa valley, s morocco. *EGUsphere*, **2023**, 1–32.

Gránásy, L., 1993: Diffuse interface theory of nucleation. *Journal of non-crystalline solids*, **162 (3)**, 301–303.

Groot Zwaaftink, C., H. Grythe, H. Skov, and A. Stohl, 2016: Substantial contribution of northern high-latitude sources to mineral dust in the arctic. *Journal of Geophysical Research: Atmospheres*, **121 (22)**, 13–678.

Groot Zwaaftink, C. D., Ó. Arnalds, P. Dagsson-Waldhauserova, S. Eckhardt, J. M. Prospero, and A. Stohl, 2017: Temporal and spatial variability of icelandic dust emissions and atmospheric transport. *Atmospheric Chemistry and Physics*, **17 (17)**, 10 865–10 878.

Harrison, A. D., K. Lever, A. Sanchez-Marroquin, M. A. Holden, T. F. Whale, M. D. Tarn, J. B. McQuaid, and B. J. Murray, 2019: The ice-nucleating ability of quartz immersed in water and its atmospheric importance compared to k-feldspar. *Atmospheric Chemistry and Physics*, **19 (17)**, 11 343–11 361.

Harrison, A. D., D. O'Sullivan, M. P. Adams, G. C. Porter, E. Blades, C. Brathwaite, R. Chewitt-Lucas, C. Gaston, R. Hawker, O. O. Krüger, et al., 2022: The ice-nucleating activity of african mineral dust in the caribbean boundary layer. *Atmospheric Chemistry and Physics Discussions*, **2022**, 1–34.

Hersbach, H., B. Bell, P. Berrisford, S. Hirahara, A. Horányi, J. Muñoz-Sabater, J. Nicolas, C. Peubey, R. Radu, D. Schepers, et al., 2020: The era5 global reanalysis. *Quarterly journal of the royal meteorological society*, **146 (730)**, 1999–2049.

Hinds, W. C. and Y. Zhu, 2022: *Aerosol technology: properties, behavior, and measurement of airborne particles*. John Wiley & Sons.

Hiranuma, N., S. Augustin-Bauditz, H. Bingemer, C. Budke, J. Curtius, A. Danielczok, K. Diehl, K. Dreischmeier, M. Ebert, F. Frank, et al., 2015: A comprehensive laboratory study on the immersion freezing behavior of illite nx particles: a comparison of 17 ice nucleation measurement techniques. *Atmospheric Chemistry and Physics*, **15 (5)**, 2489–2518.

Hofer, S., L. C. Hahn, J. K. Shaw, Z. S. McGraw, O. Bruno, F. Hellmuth, M. Pietschnig, I. A. Mostue, R. O. David, T. Carlsen, et al., 2024: Realistic representation of mixed-phase clouds increases projected climate warming. *Communications Earth & Environment*, **5 (1)**, 390.

Hogan, R. J. and A. Bozzo, 2018: A flexible and efficient radiation scheme for the ecmwf model. *Journal of Advances in Modeling Earth Systems*, **10 (8)**, 1990–2008.

Hoose, C. and O. Möhler, 2012: Heterogeneous ice nucleation on atmospheric aerosols: a review of results from laboratory experiments. *Atmospheric Chemistry and Physics*, **12 (20)**, 9817–9854.

Hoshyaripour, G. A., A. Baer, S. Bierbauer, J. Bruckert, D. Brunner, J. Foerstner, A. Hamzehloo, V. Hanft, C. Keller, M. Klose, et al., 2025: The atmospheric composition component of the icon modeling framework: Icon-art version 2025.04. *EGUsphere*, **2025**, 1–54.

Hoyle, C. R., V. Pinti, A. Welti, B. Zobrist, C. Marcolli, B. Luo, Á. Höskuldsson, H. B. Mattsson, O. Stetzer, T. Thorsteinsson, et al., 2011: Ice nucleation properties of volcanic ash from eyjafjallajökull. *Atmospheric Chemistry and Physics*, **11 (18)**, 9911–9926.

Huang, Y., A. A. Adebiyi, P. Formenti, and J. F. Kok, 2021: Linking the different diameter types of aspherical desert dust indicates that models underestimate coarse dust emission. *Geophysical Research Letters*, **48 (6)**, e2020GL092 054.

Huang, Y., J. F. Kok, K. Kandler, H. Lindqvist, T. Nousiainen, T. Sakai, A. Adebiyi, and O. Jokinen, 2020: Climate models and remote sensing retrievals neglect substantial desert dust asphericity. *Geophysical Research Letters*, **47 (6)**, e2019GL086 592.

Huang, Y., J. F. Kok, M. Saito, and O. Muñoz, 2023: Single-scattering properties of ellipsoidal dust aerosols constrained by measured dust shape distributions. *Atmospheric Chemistry and Physics*, **23 (4)**, 2557–2577.

Idso, S. B., 1976: Dust storms. *Scientific American*, **235 (4)**, 108–115.

Jahn, L. G., W. D. Fahy, D. B. Williams, and R. C. Sullivan, 2019: Role of feldspar and pyroxene minerals in the ice nucleating ability of three volcanic ashes. *ACS Earth and Space Chemistry*, **3 (4)**, 626–636.

Jin, J., A. Segers, H. X. Lin, B. Henzing, X. Wang, A. Heemink, and H. Liao, 2021: Position correction in dust storm forecasting using lotos-euros v2. 1: grid-distorted data assimilation v1. 0. *Geoscientific Model Development*, **14 (9)**, 5607–5622.

Jones, A. C., A. Hill, J. Hemmings, P. Lemaitre, A. Quérel, C. L. Ryder, and S. Woodward, 2022: Below-cloud scavenging of aerosol by rain: a review of numerical modelling approaches and sensitivity simulations with mineral dust in the met office's unified model. *Atmospheric Chemistry and Physics*, **22 (17)**, 11 381–11 407.

Kanji, Z. A., L. A. Ladino, H. Wex, Y. Boose, M. Burkert-Kohn, D. J. Cziczo, and M. Krämer, 2017: Overview of ice nucleating particles. *Meteorological monographs*, **58**, 1–1.

Kawai, K. and H. Matsui, 2025: Contributions of dust source regions to ice nucleating particles in mixed-phase clouds simulated with a global climate–aerosol model. *Journal of Climate*, **38 (18)**, 4925–4939.

Kim, D., M. Chin, G. Schuster, H. Yu, T. Takemura, P. Tuccella, P. Ginoux, X. Liu, Y. Shi, H. Matsui, et al., 2024: Where dust comes from: Global assessment of dust source attributions with aerocom models. *Journal of Geophysical Research: Atmospheres*, **129 (16)**, e2024JD041 377.

Klose, M., O. Jorba, M. Gonçalves Ageitos, J. Escribano, M. L. Dawson, V. Obiso, E. Di Tomaso, S. Basart, G. Montané Pinto, F. Macchia, P. Ginoux, J. Guerschman, C. Prigent, Y. Huang, J. F. Kok, R. L. Miller, and C. Pérez García-Pando, 2021: Mineral dust cycle in the multiscale online nonhydrostatic atmosphere chemistry model (monarch) version 2.0. *Geosci. Model Dev.*, **14 (10)**, 6403–6444.

Knippertz, P. and J.-B. W. Stuut, 2014: Mineral dust. *Mineral dust—A key player in the Earth system*, 121–147.

Köhler, H., 1936: The nucleus in and the growth of hygroscopic droplets. *Transactions of the Faraday Society*, **32**, 1152–1161.

Kok, J., S. Albani, N. Mahowald, and D. Ward, 2014: An improved dust emission model–part 2: Evaluation in the community earth system model, with implications for the use of dust source functions. *Atmospheric Chemistry and Physics*, **14 (23)**, 13 043–13 061.

Kok, J. F., T. Storelvmo, V. A. Karydis, A. A. Adebiyi, N. M. Mahowald, A. T. Evan, C. He, and D. M. Leung, 2023: Mineral dust aerosol impacts on global climate and climate change. *Nature Reviews Earth & Environment*, **4 (2)**, 71–86.

Koren, I., Y. J. Kaufman, R. Washington, M. C. Todd, Y. Rudich, J. V. Martins, and D. Rosenfeld, 2006: The bodélé depression: a single spot in the sahara that provides most of the mineral dust to the amazon forest. *Environmental Research Letters*, **1 (1)**, 014 005.

Korolev, A., G. McFarquhar, P. R. Field, C. Franklin, P. Lawson, Z. Wang, E. Williams, S. J. Abel, D. Axisa, S. Borrmann, et al., 2017: Mixed-phase clouds: Progress and challenges. *Meteorological Monographs*, **58**, 5–1.

Krämer, B., T. Peter, and H. R. Pruppacher, 1999: A theoretical determination of the dependence of the homogeneous ice nucleation rate on aerosol particle size. *Journal of the Atmospheric Sciences*, **56 (17)**, 2953–2962.

Kulkarni, P., P. A. Baron, and K. Willeke, 2011: *Aerosol measurement: principles, techniques, and applications*. John Wiley & Sons.

Kumar, A., C. Marcolli, and T. Peter, 2019: Ice nucleation activity of silicates and aluminosilicates in pure water and aqueous solutions–part 2: Quartz and amorphous silica. *Atmospheric Chemistry and Physics*, **19 (9)**, 6035–6058.

Larson, K., D. L. Hartmann, and S. A. Klein, 1999: The role of clouds, water vapor, circulation, and boundary layer structure in the sensitivity of the tropical climate. *Journal of Climate*, **12 (8)**, 2359–2374.

Lauber, A., A. Kiselev, T. Pander, P. Handmann, and T. Leisner, 2018: Secondary ice formation during freezing of levitated droplets. *Journal of the Atmospheric Sciences*, **75 (8)**, 2815–2826.

Li, J., B. E. Carlson, Y. L. Yung, D. Lv, J. Hansen, J. E. Penner, H. Liao, V. Ramaswamy, R. A. Kahn, P. Zhang, et al., 2022: Scattering and absorbing aerosols in the climate system. *Nature Reviews Earth & Environment*, **3 (6)**, 363–379.

Loeb, N. G., D. R. Doelling, H. Wang, W. Su, C. Nguyen, J. G. Corbett, L. Liang, C. Mitrescu, F. G. Rose, and S. Kato, 2018: Clouds and the earth's radiant energy system (ceres) energy balanced and filled (ebaf) top-of-atmosphere (toa) edition-4.0 data product. *Journal of climate*, **31 (2)**, 895–918.

Lohmann, U., F. Lüönd, and F. Mahrt, 2016: *An introduction to clouds: From the microscale to climate*. Cambridge University Press.

Lüttmer, T., P. Spichtinger, and A. Seifert, 2025: Investigating ice formation pathways using a novel two-moment multi-class cloud microphysics scheme. *Atmospheric Chemistry and Physics*, **25 (8)**, 4505–4529.

Mahowald, N., S. Albani, J. F. Kok, S. Engelstaeder, R. Scanza, D. S. Ward, and M. G. Flanner, 2014: The size distribution of desert dust aerosols and its impact on the earth system. *Aeolian Research*, **15**, 53–71.

Marticorena, B. and G. Bergametti, 1995: Modeling the atmospheric dust cycle: 1. design of a soil-derived dust emission scheme. *Journal of Geophysical Research: Atmospheres*, **100 (D8)**, 16 415–16 430, URL http://dx.doi.org/10.1029/95jd00690.

Meinander, O., P. Dagsson-Waldhauserova, P. Amosov, E. Aseyeva, C. Atkins, A. Baklanov, C. Baldo, S. Barr, B. Barzycka, L. Benning, et al., 2022: Newly identified climatically and environmentally significant high latitude dust sources. *Atmospheric Chemistry and Physics*, **22 (17)**, 11 889–11 930.

Mejia, F., J. Kleissl, and J. Bosch, 2014: The effect of dust on solar photovoltaic systems. *Energy Procedia*, **49**, 2370–2376.

Meng, J., Y. Huang, D. M. Leung, L. Li, A. A. Adebiyi, C. L. Ryder, N. M. Mahowald, and J. F. Kok, 2022: Improved parameterization for the size distribution of emitted dust aerosols reduces model underestimation of super coarse dust. *Geophysical Research Letters*, **49 (8)**, e2021GL097 287.

Meskhidze, N., W. Chameides, and A. Nenes, 2005: Dust and pollution: A recipe for enhanced ocean fertilization? *Journal of Geophysical Research: Atmospheres*, **110 (D3)**.

Meyer, H., K. Kandler, S. Dupont, J. Escribano, J. Girdwood, G. Nikolich, A. Alastuey, V. Etyemezian, C. González Flórez, A. González-Romero, et al., 2026: From fine to giant: multi-instrument assessment of the dust particle size distribution at an emission source during the j-wadi field campaign. *Atmospheric Measurement Techniques*, **19**, 21–61.

Middleton, N. and A. Al-Hemoud, 2024: Sand and dust storms: recent developments in impact mitigation. *Sustainability*, **16 (16)**, 7121.

Mossop, S., 1976: Production of secondary ice particles during the growth of graupel by riming. *Quarterly Journal of the Royal Meteorological Society*, **102 (431)**, 45–57.

Murray, B. J., S. Broadley, T. Wilson, J. Atkinson, and R. Wills, 2011: Heterogeneous freezing of water droplets containing kaolinite particles. *Atmospheric Chemistry and Physics*, **11 (9)**, 4191–4207.

Murray, B. J., D. O'sullivan, J. Atkinson, and M. Webb, 2012: Ice nucleation by particles immersed in supercooled cloud droplets. *Chemical Society Reviews*, **41 (19)**, 6519–6554.

Niedermeier, D., R. Shaw, S. Hartmann, H. Wex, T. Clauss, J. Voigtländer, and F. Stratmann, 2011: Heterogeneous ice nucleation: exploring the transition from stochastic to singular freezing behavior. *Atmospheric Chemistry and Physics*, **11 (16)**, 8767–8775.

Niemand, M., O. Möhler, B. Vogel, H. Vogel, C. Hoose, P. Connolly, H. Klein, H. Bingemer, P. DeMott, J. Skrotzki, et al., 2012: A particle-surface-area-based parameterization of immersion freezing on desert dust particles. *Journal of the Atmospheric Sciences*, **69 (10)**, 3077–3092.

Nyquist, R. M., V. Talanquer, and D. W. Oxtoby, 1995: Density functional theory of nucleation: A semiempirical approach. *The Journal of chemical physics*, **103 (3)**, 1175–1179.

Obiso, V., M. Gonçalves Ageitos, C. Pérez García-Pando, J. P. Perlwitz, G. L. Schuster, S. E. Bauer, C. Di Biagio, P. Formenti, K. Tsigaridis, and R. L. Miller, 2024: Observationally constrained regional variations of shortwave absorption by iron oxides emphasize the cooling effect of dust. *Atmospheric Chemistry and Physics*, **24 (9)**, 5337–5367.

Okada, K., J. Heintzenberg, K. Kai, and Y. Qin, 2001: Shape of atmospheric mineral particles collected in three chinese arid-regions. *Geophysical Research Letters*, **28 (16)**, 3123–3126.

Pan, L., P. S. Bhattacharjee, L. Zhang, R. Montuoro, B. Baker, J. McQueen, G. A. Grell, S. A. McKeen, S. Kondragunta, X. Zhang, et al., 2023: Analysis of gefs-aerosols annual budget to better understand the aerosol predictions simulated in the model. *Geoscientific Model Development Discussions*, **2023**, 1–32.

Panta, A., K. Kandler, A. Alastuey, C. González-Flórez, A. González-Romero, M. Klose, X. Querol, C. Reche, J. Yus-Díez, and C. Pérez García-Pando, 2023: Insights into the single-particle composition, size, mixing state, and aspect ratio of freshly emitted mineral dust from field measurements in the moroccan sahara using electron microscopy. *Atmospheric Chemistry and Physics*, **23 (6)**, 3861–3885.

Panta, A., K. Kandler, K. Schepanski, A. Alastuey, P. Dagsson Waldhauserova, S. Dupont, M. Eknayan, C. González-Flórez, A. González-Romero, M. Klose, et al., 2025: Unveiling single-particle composition, size, shape, and mixing state of freshly emitted icelandic dust via electron microscopy analysis. *Atmospheric Chemistry and Physics*, **25 (18)**, 10 457–10 478.

Paramonov, M., R. O. David, R. Kretzschmar, and Z. A. Kanji, 2018: A laboratory investigation of the ice nucleation efficiency of three types of mineral and soil dust. *Atmospheric Chemistry and Physics*, **18 (22)**, 16 515–16 536.

Parra, S., M. A. Bravo, W. Quiroz, T. Moreno, A. Karanasiou, O. Font, V. Vidal, and F. Cereceda, 2014: Distribution of trace elements in particle size fractions for contaminated soils by a copper smelting from different zones of the puchuncaví valley (chile). *Chemosphere*, **111**, 513–521.

Petters, M. and S. Kreidenweis, 2007: A single parameter representation of hygroscopic growth and cloud condensation nucleus activity. *Atmospheric Chemistry and Physics*, **7 (8)**, 1961–1971.

Pham, T. V., C. Steger, B. Rockel, K. Keuler, I. Kirchner, M. Mertens, D. Rieger, G. Zängl, and B. Früh, 2021: Icon in climate limited-area mode (icon release version 2.6. 1): a new regional climate model. *Geoscientific Model Development*, **14 (2)**, 985–1005.

Phillips, V. T., P. J. DeMott, and C. Andronache, 2008: An empirical parameterization of heterogeneous ice nucleation for multiple chemical species of aerosol. *Journal of the atmospheric sciences*, **65 (9)**, 2757–2783.

Prasad, A. A., N. Nishant, and M. Kay, 2022: Dust cycle and soiling issues affecting solar energy reductions in australia using multiple datasets. *Applied Energy*, **310**, 118 626.

Price, H., K. Baustian, J. McQuaid, A. Blyth, K. Bower, T. Choularton, R. Cotton, Z. Cui, P. Field, M. Gallagher, et al., 2018: Atmospheric ice-nucleating particles in the dusty tropical atlantic. *Journal of Geophysical Research: Atmospheres*, **123 (4)**, 2175–2193.

Prill, F., D. Reinert, D. Rieger, and G. Zängl, 2022: Icon tutorial. *ICON*, **1**.

Pruppacher, H. R., J. D. Klett, and P. K. Wang, 1998: Microphysics of clouds and precipitation.

Ramadoss, V., K. Pfannkuch, A. Protat, Y. Huang, S. Siems, and A. Possner, 2024: An evaluation of cloud-precipitation structures in mixed-phase stratocumuli over the southern ocean in kilometer-scale icon simulations during capricorn. *Journal of Geophysical Research: Atmospheres*, **129 (18)**, e2022JD038 251.

Reguera, D. and H. Reiss, 2004: Extended modified liquid drop- dynamical nucleation theory (emld- dnt) approach to nucleation: A new theory. *The Journal of Physical Chemistry B*, **108 (51)**, 19 831–19 842.

Reicher, N., C. Budke, L. Eickhoff, S. Raveh-Rubin, I. Kaplan-Ashiri, T. Koop, and Y. Rudich, 2019: Size-dependent ice nucleation by airborne particles during dust events in the eastern mediterranean. *Atmospheric Chemistry and Physics*, **19 (17)**, 11 143–11 158.

Ren, J., F. Zhang, Y. Wang, D. Collins, X. Fan, X. Jin, W. Xu, Y. Sun, M. Cribb, and Z. Li, 2018: Using different assumptions of aerosol mixing state and chemical composition to predict ccn concentrations based on field measurements in urban beijing. *Atmospheric Chemistry and Physics*, **18 (9)**, 6907–6921.

Rieger, D., M. Bangert, I. Bischoff-Gauss, J. Förstner, K. Lundgren, D. Reinert, J. Schröter, H. Vogel, G. Zängl, R. Ruhnke, et al., 2015: Icon–art 1.0–a new online-coupled model system from the global to regional scale. *Geoscientific Model Development*, **8 (6)**, 1659–1676.

Ryder, C. L., E. J. Highwood, A. Walser, P. Seibert, A. Philipp, and B. Weinzierl, 2019: Coarse and giant particles are ubiquitous in saharan dust export regions and are radiatively significant over the sahara. *Atmospheric Chemistry and Physics*, **19 (24)**, 15 353–15 376.

Ryder, C. L., F. Marenco, J. K. Brooke, V. Estelles, R. Cotton, P. Formenti, J. B. McQuaid, H. C. Price, D. Liu, P. Ausset, et al., 2018: Coarse-mode mineral dust size distributions, composition and optical properties from aer-d aircraft measurements over the tropical eastern atlantic. *Atmospheric Chemistry and Physics*, **18 (23)**, 17 225–17 257.

Sanchez-Marroquin, A., O. Arnalds, K. Baustian-Dorsi, J. Browse, P. Dagsson-Waldhauserova, A. Harrison, E. Maters, K. Pringle, J. Vergara-Temprado, I. Burke, et al., 2020: Iceland is an episodic source of atmospheric ice-nucleating particles relevant for mixed-phase clouds. *Science advances*, **6 (26)**, eaba8137.

Schiebel, T., 2017: Ice nucleation activity of soil dust aerosols. Ph.D. thesis, Dissertation, Karlsruhe, Karlsruher Institut für Technologie (KIT), 2017.

Seifert, A. and K. D. Beheng, 2006: A two-moment cloud microphysics parameterization for mixed-phase clouds. part 1: Model description. *Meteorology and atmospheric physics*, **92 (1)**, 45–66.

Seinfeld, J. H. and S. N. Pandis, 2016: *Atmospheric chemistry and physics: from air pollution to climate change*. John Wiley & Sons.

Shao, Y. and H. Lu, 2000: A simple expression for wind erosion threshold friction velocity. *Journal of Geophysical Research: Atmospheres*, **105 (D17)**, 22 437–22 443.

Shi, Y. and X. Liu, 2019: Dust radiative effects on climate by glaciating mixed-phase clouds. *Geophysical Research Letters*, **46 (11)**, 6128–6137.

Shi, Y., X. Liu, M. Wu, X. Zhao, Z. Ke, and H. Brown, 2022: Relative importance of high-latitude local and long-range-transported dust for arctic ice-nucleating particles and impacts on arctic mixed-phase clouds. *Atmospheric Chemistry and Physics*, **22 (4)**, 2909–2935.

Sofiev, M., J. Vira, R. Kouznetsov, M. Prank, J. Soares, and E. Genikhovich, 2015: Construction of the silam eulerian atmospheric dispersion model based on the advection algorithm of michael galperin. *Geoscientific Model Development*, **8 (11)**, 3497–3522.

Steinke, I., O. Möhler, A. Kiselev, M. Niemand, H. Saathoff, M. Schnaiter, J. Skrotzki, C. Hoose, and T. Leisner, 2011: Ice nucleation properties of fine ash particles from the eyjafjallajökull eruption in april 2010. *Atmospheric Chemistry and Physics*, **11 (24)**, 12 945–12 958.

Stoyanova, V., D. Kashchiev, and T. Kupenova, 1994: Freezing of water droplets seeded with atmospheric aerosols and ice nucleation activity of the aerosols. *Journal of aerosol science*, **25 (5)**, 867–877.

Swart, P., A. Oehlert, G. Mackenzie, G. Eberli, and J. Reijmer, 2014: The fertilization of the bahamas by saharan dust: A trigger for carbonate precipitation? *Geology*, **42 (8)**, 671–674.

Tan, I., T. Storelvmo, and M. D. Zelinka, 2016: Observational constraints on mixed-phase clouds imply higher climate sensitivity. *Science*, **352 (6282)**, 224–227.

Taylor, P. C., 2012: The role of clouds: An introduction and rapporteur report. *Surveys in geophysics*, **33**, 609–617.

Tian, L., L. Chen, P. Zhang, and L. Bi, 2021: Estimating radiative forcing efficiency of dust aerosol based on direct satellite observations: case studies over the sahara and taklimakan desert. *Atmospheric Chemistry and Physics*, **21 (15)**, 11 669–11 687.

Toledano, C., B. Torres, C. Velasco-Merino, D. Althausen, S. Groß, M. Wiegner, B. Weinzierl, J. Gasteiger, A. Ansmann, R. González, et al., 2019: Sun photometer retrievals of saharan dust properties over barbados during saltrace. *Atmospheric Chemistry and Physics*, **19 (23)**, 14 571–14 583.

Toledano, C., M. Wiegner, S. Groß, V. Freudenthaler, J. Gasteiger, D. Müller, D. Müller, A. Schladitz, B. Weinzierl, B. Torres, et al., 2011: Optical properties of aerosol mixtures derived from sun-sky radiometry during samum-2. *Tellus B: Chemical and Physical Meteorology*, **63 (4)**, 635–648.

TU Darmstadt, Department of Geoinformation Science, 2025: Gomera hilda live. `https://gomera.geo.tu-darmstadt.de/live/hilda/`, accessed: 2025-09-29.

Ullrich, R., C. Hoose, O. Möhler, M. Niemand, R. Wagner, K. Höhler, N. Hiranuma, H. Saathoff, and T. Leisner, 2017: A new ice nucleation active site parameterization for desert dust and soot. *Journal of the Atmospheric Sciences*, **74 (3)**, 699–717.

Vali, G., 1971: Quantitative evaluation of experimental results an the heterogeneous freezing nucleation of supercooled liquids. *Journal of Atmospheric Sciences*, **28 (3)**, 402–409.

———, 2014: Interpretation of freezing nucleation experiments: singular and stochastic; sites and surfaces. *Atmospheric Chemistry and Physics*, **14 (11)**, 5271–5294.

Van Der Does, M., P. Knippertz, P. Zschenderlein, R. Giles Harrison, and J.-B. W. Stuut, 2018: The mysterious long-range transport of giant mineral dust particles. *Science advances*, **4 (12)**, eaau2768.

Velasco-Merino, C., D. Mateos, C. Toledano, J. M. Prospero, J. Molinie, L. Euphrasie-Clotilde, R. González, V. E. Cachorro, A. Calle, and A. M. de Frutos, 2018: Impact of long-range transport over the atlantic ocean on saharan dust optical and microphysical properties based on aeronet data. *Atmospheric Chemistry and Physics*, **18 (13)**, 9411–9424.

Vergara-Palacio, S., A. Kiselev, F. Vogel, A. González-Romero, R. Fösig, X. Querol, C. Hoose, N. Silas Umo, O. Möhler, K. Kandler, C. Pérez García-Pando, and M. Klose, 2026: Ice nucleation activity of mineral dust from morocco and iceland in immersion freezing mode and its relationship with mineralogy and particle size. *Atmospheric Chemistry and Physics*, **26 (12)**, 9113–9147, URL `http://dx.doi.org/10.5194/acp-26-9113-2026`.

Vogel, B., C. Hoose, H. Vogel, and C. Kottmeier, 2006: A model of dust transport applied to the dead sea area. *Meteorologische Zeitschrift (Berlin)*, **15**.

Vogel, F., L. Lacher, J. Nadolny, H. Saathoff, T. Leisner, and O. Möhler, 2022: Development and validation of a new cloud simulation experiment for lab-based aerosol-cloud studies. *The Review of scientific instruments*, **93 (9)**, 095 106.

Wang, Y., P. Zhang, J. Li, Y. Liu, Y. Zhang, J. Li, and Z. Han, 2024: An updated aerosol simulation in the community earth system model (v2. 1.3): dust and marine aerosol emissions and secondary organic aerosol formation. *Geoscientific Model Development Discussions*, **2024**, 1–38.

Wielicki, B. A., B. R. Barkstrom, E. F. Harrison, R. B. Lee III, G. L. Smith, and J. E. Cooper, 1996: Clouds and the earth's radiant energy system (ceres): An earth observing system experiment. *Bulletin of the American Meteorological Society*, **77 (5)**, 853–868.

Yang, C. A., M. Diao, A. Gettelman, K. Zhang, J. Sun, G. McFarquhar, and W. Wu, 2021: Ice and supercooled liquid water distributions over the southern ocean based on in situ observations and climate model simulations. *Journal of Geophysical Research: Atmospheres*, **126 (24)**, e2021JD036 045.

Yin, Y., S. Wurzler, Z. Levin, and T. G. Reisin, 2002: Interactions of mineral dust particles and clouds: Effects on precipitation and cloud optical properties. *Journal of Geophysical Research: Atmospheres*, **107 (D23)**, AAC–19.

Zängl, G., D. Reinert, and F. Prill, 2022: Grid refinement in icon v2. 6.4. *Geoscientific Model Development Discussions*, **2022**, 1–32.

Zängl, G., D. Reinert, P. Rípodas, and M. Baldauf, 2015: The icon (icosahedral non-hydrostatic) modelling framework of dwd and mpi-m: Description of the non-hydrostatic dynamical core, qj roy. meteor. soc., 141, 563–579.

Zeng, Q. and S. Xu, 2015: Thermodynamics and characteristics of heterogeneous nucleation on fractal surfaces. *The Journal of Physical Chemistry C*, **119 (49)**, 27 426–27 433.

Zhao, Y., Y. Wang, C. Liang, J. Wang, J. Fang, and M. Zhou, 2022: Study of mixed pollution of haze and dust in jinan based on lidar. *Photonics*, MDPI, Vol. 9, 144.

Zhu, K. and L. Wang, 2024: A comprehensive study on the validation and application of multi-lognormal distribution models for atmospheric particles. *Atmospheric Environment*, **338**, 120 813.

Zimmermann, F., S. Weinbruch, L. Schütz, H. Hofmann, M. Ebert, K. Kandler, and A. Worringen, 2008: Ice nucleation properties of the most abundant mineral dust phases. *Journal of Geophysical Research: Atmospheres*, **113 (D23)**.

Zobrist, B., T. Koop, B. Luo, C. Marcolli, and T. Peter, 2007: Heterogeneous ice nucleation rate coefficient of water droplets coated by a nonadecanol monolayer. *The Journal of Physical Chemistry C*, **111 (5)**, 2149–2155.

List of Figures

1.1 Illustration of the approach used in this thesis: a field campaign provides samples for immersion-freezing experiments; the resulting data are analyzed to derive new source-specific INAS parameterizations, which are then implemented in ICON-ART modeling to assess their effects on mixed-phase clouds. I thank Julian Vergara Palacio for contributing to the creation of the illustration. 5

3.1 Supersaturation with respect to ice (S_i) as a function of temperature. Solid blue line shows S_i for the case of water saturation ($S_w = 1$), above blue line supersaturated environment, below blue line unsaturated environment. Additionally, the deposition nucleation, immersion freezing, contact freezing, and homogeneous freezing nucleation modes are shown. Blue sphere: water droplet, brown shape: aerosol particle, and blue elongated shape: water droplet nucleated to ice. 14

3.2 Free energy required for cluster formation under unsaturated (teal lines) and supersaturated (orange lines) conditions. Dark blue colored circles illustrate the growth of the cluster. 16

3.3 Cluster formation on the surface of an insoluble particle. θ is the angle between the surface of the particle and the cluster (tangent line at the point where the solid particle (S), the liquid cluster (L), and the initial phase (V) meet). 17

3.4 Behavior of $f(m,x)$ for different cases. With $x = 0$ (green solid line), $x = 0.7$ (dashed green line), $x = 2$ (dotted green line), $X \to \infty$ (solid dark green line), and considering the case in which the surface of the particle is flat (dashed orange line). 18

3.5 Schematic representation of the concept of surface active sites in which an aerosol particle is immersed in a water droplet at temperature T' (blue background). Left: an aerosol particle is characterized by having different active sites (shapes inside red circles) which have specific nucleation temperatures (T1, T2, T3, T4, T5). Right: Once the temperature inside the droplet is decreased such that T2<T'<T1, the nucleation of the active site associated with T1 is triggered. 20

3.6 Schematic of different processes that an ice crystal particle undergoes within a cloud. a) Diffusional growth, b) Wegener-Bergeron-Findeisen proces, c) aggregation, d) riming, e) collision, f) rime-splintering process. Small blue dots represent water vapor, medium blue circles represent cloud droplets, large blue shape represents graupel, and gray figure represents ice crystal. 23

4.1 Reproduced from Panta et al. (2023) (a) Northwestern Africa showing the area of operation of the FRAGMENT campaign. The main location of L'Bour is shown by a star and is located close to the Drâa river basin. (b) Schematic representation of different instruments used in the campaign, with green dots highlighting those instruments used for single particle analysis. (c) Flat-plate deposition sampler (FPS). (d) Free-wing impactor (FWI). (e) Cascade impactor (micro-orifice uniform deposit impactor, MOUDI). (f) Sampling schedule of particle collection using different techniques. The horizontal bar represents the start and end of the sampling time. Note that due to very short sampling time for FWI and MOUDI, the two bars (start and end) appear as one. Panel (a) was created using Google Earth (US Dept of State Geographer, Data SIO, NOAA, US Navy, NGA, GEBCO, © 2020 Google, Image Landsat/Copernicus). 26

4.2 Reproduced from González-Romero et al. (2024) Location of Iceland dust hotspots and samples. The green polygon marks the limits of Holuhraun lava field. Dashed black lines mark the area of the different dust hotspots in Iceland, and dots represent samples as top sediments (red), sediments (blue), and aeolian ripples (yellow). Basemap: imagery data from © Google Earth Pro v: 7.3.6.9345. Jökulsá á Fjöllum is marked as (a), and AVIRIS data flight images were used in the zoom-in of Dyngjusandur (b) and Dyngjuvatn (c) for a more updated vision of the lakes. The yellow star represents the experimental site. . . 27

4.3 Schematic representation of AIDA with the main instruments involved in the experiments. 29

4.4 a) Relationship between optical and geometrical diameter for Morocco and Iceland. Optical sensor with wavelength center at 0.44 µm, and 85 to 95° scattering angle, b) Surface area, S_{mean}, as a function of volume-equivalent diameter assuming spherical and ellipsoidal shapes for globally averaged values of mineral dust AR and HWR distributions. . 32

4.5 Normalized surface area distribution measured during a 5-minute interval directly before AIDA (ID) and AIDAm (ID_m) expansion for Morocco for experiment a) ID: 5, 9, 10, ID_m: 9; b) ID: 14, 21, 27, ID_m: 27; c) ID: 13, 20, 26, ID_m: 13, 26; d) ID and ID_m: 16, 23, 24; e) ID: 25, 28, 29, ID_m: 25, 28; and f) for all experiments in AIDA. Additionally, the surface area distribution measured with laser diffraction (LD) technique after sieving the samples presented. The experiments are grouped according to the stage of the cascade impactor they were obtained. 34

4.6 Normalized surface area distribution measured during a 5-minute interval directly before AIDA (ID) and AIDAm (ID_m) expansion for Iceland for experiment a) ID: 12, 34; b) ID: 11, 17, 33, ID_m: 17; c) ID and ID_m: 15, 22, 30; d) ID: 3, 6, 19, 31, ID_m: 3, 19, 31; and e) for all experiments in AIDA. Additionally, the surface area distribution measured with laser diffraction (LD) technique after sieving the samples presented. The experiments are grouped according to the stage of the cascade impactor they were obtained. 46
4.7 Schematic of the coupling of ART into ICON. Blue boxes represent processes implemented in ICON, while orange boxes represent processes implemented in ART. Blue boxes with an orange frame indicate ICON processes in which ART tracers are treated within the ICON framework. Schematic taken from Hoshyaripour et al. (2025). 47
4.8 Normalized lognormal particle size distribution for each dust mode, named dusta, dustb, and dustc, in ICON-ART. The geometric mean radius and geometric standard deviation for dusta, dustb and dustc are 0.6445 μm and 1.7, 3.454 μm and 1.6, and 8.672 μm and 1.5, respectively. 48
4.9 Number of hourly AERONET measurements from June to August 2021 at all stations for (a) AOD at 551 nm, (b) AE values below 0.3, and (c) the overlap where both AOD and AE $<$ 0.3 are available. "Station (filtered)" indicates that only stations with numerical data are included. 49

5.1 Relative error between the different approaches of computing INAS density for Moroccan dust. The box represents the interquartile range (IQR) from the first quartile to the third quartile (Q1 to Q3), the horizontal orange line inside the box represents the median value. The whiskers extend to the smallest and largest values within 1.5 times the IQR, and outliers beyond the whiskers are shown as individual circles. Experiments are sorted by the temperature at which the first ice particle was detected, in order of increasing temperature. For AIDA experiments: (a) for polynomial of degree 5 (Eq. (3.29)) and (b) for summation of differential nucleus concentration (Eq. (3.31)). (c) and (d) as (a) and (b), but for INSEKT experiments. 52
5.2 Relative error for the different approaches of computing inas density for Iceland. The box represents the interquartile range (IQR) from the first quartile to the third quartile (Q1 to Q3), the horizontal orange line inside the box represents the median value. The whiskers extend to the smallest and largest values within 1.5 times the IQR, and outliers beyond the whiskers are shown as individual circles. Experiments are sorted by the temperature at which the first ice particle was detected, in order of increasing temperature. For AIDA experiments: (a) and (b) for polynomial of degree 5 and summation of differential nucleus concentration, respectively. For INSEKT experiments: (c) and (d) for polynomial of degree 5 and summation of differential nucleus concentration, respectively. 53

5.3 Differential (a,c) and cumulative (b,d) nucleus concentrations obtained for samples from Morocco for AIDA experiments (a,b) and INSEKT experiments (c,d). 54
5.4 Differential (a,c) and cumulative (b,d) nucleus concentrations obtained for samples from Iceland for AIDA experiments (a,b) and INSEKT experiments (c,d) 55
5.5 Experimental values of INAS density from AIDA and INSEKT experiments for linear regression (P1) for (a) Morocco and (b) Iceland, Table 5.1 presents the coefficients for the linear regression. Also shown are the parameterizations from Ullrich et al. (2017) denoted as Ullrich, Harrison et al. (2019) denoted as K-feldspar (Harrison), K-feldspar (Harrison) 20%, and K-feldspar (Harrison) 1%, and Sanchez-Marroquin et al. (2020) labeled as Iceland_2020 Sanchez-Marroquin. The blue shaded area represents the 95% confidence interval. 57
5.6 a) INAS density fit computed with all experiments for Morocco (orange line, "Morocco"), not considering experiments IDs 5, 9, 10 (blue line, "Morocco cropped"), and only considering experiment IDs 5, 9, 10 (green line, 'Morocco selected exp'). b) as in a) but for all experiments for Iceland (orange line, "Iceland"), not considering experiment IDs 12, 34 (blue line, "Iceland cropped"), considering only experiment IDs 12, 34 (green line, "Iceland selected exp"). 58
5.7 INAS density for AIDAm experiments. Symbol color refers to the time at which AIDAm experiment is performed relative to the first expansion in AIDAm for each injection in AIDA. a) for Moroccan samples, AIDA is the fit developed with AIDA experiments for Morocco. b) for Icelandic samples, AIDA is the fit obtained with AIDA experiments for our Icelandic samples. In addition, relevant parameterizations from other authors are considered: Harrison et al (Harrison et al., 2019) is the fit for k-feldspar, Ullrich et al (Ullrich et al., 2017) and Iceland_2020 Sanchez-Marroquin (Sanchez-Marroquin et al., 2020). 59
5.8 Normalized surface area distribution for AIDAm experiments for Moroccan samples. The blue line represents the mean value, while the blue shading indicates the standard deviation across all expansions of the same sample, as measured by AIDAm sensors before expansion (SMPS, APS, and OPC). The red line represents measurements obtained using the laser diffraction (LD) technique on the freshly sieved sample. 60
5.9 Normalized surface area distribution for AIDAm experiments for Icelandic samples. The blue line represents the mean value, while the blue shading indicates the standard deviation across all expansions of the same sample, as measured by AIDAm sensors before expansion (SMPS, APS, and OPC). The red line represents measurements obtained using the laser diffraction (LD) technique on the freshly sieved sample. 61

5.10 Observed (AERONET stations, obtained with approach described in Sect. 4.3) and simulated DAOD with correlation coefficient (r): (a) monthly mean at each station (locations shown in panel e) for summer 2021, horizontal error bars represent the interquartile range (IQR), defined as half the distance between the 25th and 75th percentiles, (b) 2-hourly data for all stations (locations shown in panel e) during summer 2021, with symbols colored by date. The dashed red line indicates the 1:1 relationship, and the dashed blue lines indicate a factor of 2 bias. (c) percentage of simulated DAOD values exceeding the observed values by a factor of 2, and (d) percentage of simulated DAOD values more than two times lower than observed, both based on 2-hourly data. Panel (e) shows the mean simulated DAOD for summer and the station locations used in panels (a)–(d). . . . 70

5.11 Simulated and observed PM_{10} dust concentrations at Mýrar, Iceland (63°30′27.4″ N, 18°19′45.2″ W) during summer 2021. Panels (a) and (c) show 2-hourly and weekly mean time series of the measurements, respectively, while panels (b) and (d) present the corresponding simulated and observed values. Blue dashed lines are 10 times bias. . . . 71

5.12 Summer 2021 average simulated Icelandic dust emissions (tonnes day^{-1}). Markers denote emission hotspots identified by Arnalds et al. (2016). 71

5.13 Zonal mean atmospheric dust concentration and planetary boundary layer height (PBL; a, d, g), monthly mean dust column burden (DCB; b, e, h), and DCB frequency distribution (blue bars) with cumulative DCB across bins (red line, right y-axis; c, f, i) for June, July, and August, respectively. All metrics are computed over domain 2. 72

5.14 Ice-nucleating particle (INP) column burden for June, July, and August 2021. Rows correspond to months; columns correspond to the default, LLD_HLD, and LLD_SHLD cases. 72

5.15 Ice-nucleating particle (INP) zonal average for June, July, and August 2021 within the region 54.8° W $<$ lon $<$ 1.9° W and 61° N $<$ lat $<$ 69° N. Rows correspond to months; columns correspond to the default, LLD_HLD, and LLD_SHLD cases. Red line shows the temperature zonal average for -6° C and vertical black dots the relative humidity zonal average above 85%. 73

5.16 Total Icelandic INP fraction (Icelandic INP over total INP; Icelandic plus elsewhere), summed over space and time (first column: a, c, e) and over space and height (second column: b, d, f), for June, July, and August 2021, for the three cases considered-default, LLD_HLD, and LLD_SHLD- within the region 54.8° W $<$ lon $<$ 1.9° W and 61° N $<$ lat $<$ 69° N. Rows correspond to months. 74

5.17 Spatial averages of mixed-phase cloud (MPC) occurrence (top row) and spatiotemporal averages of MPC cover (bottom row) for June (a,d), July (b,e), and August (c,f) of 2021. Curves denote simulation cases: default (blue), LLD_HLD (green), and LLD_SHLD (orange); shaded bands show the corresponding MPC presence (overlapping of all color give a brownish color). Black arrows in panels (a–c) mark the x-axis used for the dashed curves (top axis) and the solid curves (bottom axis). 75
5.18 Spatiotemporal profiles inside MPCs for June, July, and August (rows). Columns show rain rate (a,d,g), effective radius of liquid water (b,e,h), and snow rate (c,f,i). Lines denote simulation cases, default (blue), LLD_HLD (green), and LLD_SHLD (orange), and the shaded bands indicate the corresponding MPC presence. 75
5.19 Monthly cloud radiative effect (CRE) averaged over the study area for June, July, and August 2021 (rows). Columns show total CRE (a,d,g), shortwave (SW) CRE (b,e,h), and longwave (LW) CRE (c,f,i). Pink bars, referenced to the right y-axis, give the absolute percent error (positive value) of each case relative to CERES. 76

6.1 INAS density parameterizations for Morocco with standard (red solid line) and effective (red dashed line) surface area, and Iceland with standard (blue solid) and with effective (blue dashed line) surface area. Comparison with experimental data from Steinke et al. (2011, blue diamonds), Jahn et al. (2019, purple diamonds), Price et al. (2018, orange circles), 1%-K-feldspar scaled Harrison et al. (2019, brown dashed line), Sanchez-Marroquin et al. (2020, light blue dashed line), and Reicher et al. (2019, open black stars, circles, and diagonal crosses) for samples with different cut-off diameter. 79
6.2 Ice active fraction for AIDA experiments carried out with the same initial temperature, but using dust aerosol with different contributions of fine, coarse, and super-coarse particles to the total surface area for Moroccan samples, contribution from each size range are indicated in the label. a) experiments 5 and 16 at 249 K, b) experiments 9 and 20 at 254 K, c) experiment 26 and 27 at 252 K, d) experiment 28 and 29 at 251 K, e) Surface area concentration ratio and, f) number fraction of particles for Moroccan samples divided into fine, coarse, and super-coarse particle contributions for each experiment. 89
6.3 Ice active fraction for experiments with Icelandic samples carried out at the same initial temperatures: a) T $\approx$ 249 K, b) T = 247 K, c) T = 253 K, d) 245, labels indicate the contribution to the total surface area from each bin. A more detailed division is presented in e) Surface area concentration ratio and f) number fraction of particles for samples divided according to the size dependence of the pyroxene relative volume fraction presented in Panta et al. (2025). 90

6.4 Surface area concentration ratio for Iceland experiments in Steinke et al. (2011). Contribution of size ranges divided into (a) fine, coarse, and super-coarse particles, (b) $d \leq 5$ and $5 < d \leq 15$. Metrics computed according to information presented in Fig. 3 in Steinke et al. (2011). Exp 100 with a cut-off of 15 µm, and exp 103 with a cut-off of 5 µm. 91

C.1 Field location and set-up. (a) Background image from Bing maps with the field site marked with a pink cross, (b) topographic map, field set-up, and surrounding of J-WADI, (c) set-up at the measurement site with the instruments used marked in pink (SCINTTRANS/-REC = scintillometer transmitter/receiver, ROTMAST = rotating mast, DEP = deposition sampler), (d) photo of the site center including most instruments used in this study in their field deployment. Background map copyright (a) ©Microsoft, (b) and (c) Esri, Maxar, Earthstar Geographics, and the GIS User Community. Reproduced from Meyer et al. (2026). 112

List of Tables

3.1 Summary of aerosol effective/equivalent diameters using different particle properties. V_p is particle volume, D_V is the volume-equivalent diameter, ρ_p is the particle density, ρ_0=1000 kg m^{-3} is the reference density, χ is the dynamic shape factor, a dimensionless parameter that quantifies the increased drag on a non-spherical particle relative to a volume-equivalent sphere, and A_p is the projected area of the particle. 10

3.2 Approaches used to describe ice nucleation. 19

4.1 Conditions during the AIDA experiments conducted with Moroccan samples. ID: experiment identifier, $C_{n,ae}$: initial (before chamber expansion) total number concentration, d_n: mean diameter for the number concentration size distribution, S_{ae}: initial total surface area concentration, $d_{1,s}$ and $d_{2,s}$ mean diameter of the bimodal surface area size distribution, T_{start}: temperature at which the first ice formation was observed. 30

4.2 Conditions during the AIDA experiments conducted with Icelandic samples. ID: experiment identifier, $C_{n,ae}$: initial (before chamber expansion) total number concentration, d_n: mean diameter for the number concentration size distribution, S_{ae}: initial total surface area concentration, $d_{1,s}$ and $d_{2,s}$ mean diameter of the bimodal surface area size distribution, T_{start}: temperature at which the first ice formation was observed. 31

4.3 Total number of horizontal cells for a global domain and effective grid resolution for a set of ICON grid resolutions. From coarser (R2B04) to finer (R2B09) resolutions. 35

4.4 Different experiments considered in this study. Parameterizations are used for immersion freezing mode. The Default case uses Ullrich et al. (2017); LLD_HLD and LLD_SHLD use Vergara-Palacio et al. (2026). 45

5.1 Coefficients from lower to higher power and Bayesian information criterion (BIC) for linear regression (P1; $ln(n_s(T)) = a + bT$ where T is temperature in K) for Morocco and Iceland, for the combined results from AIDA and INSEKT (Figure 5.5) measurements. . 56

6.1 Derived statistics for the pairwise logarithmic ratio of ice active frozen fraction between experiment number a ($\exp_a$) and experiment number b ($\exp_b$), defined as $\log_{10}(FF_a(T)) - \log_{10}(FF_b(T))$, computed at matched temperatures (temperature difference smaller than 0.7 K) for the Morocco experiments shown in Fig. 6.2. n is the number of matched ice active frozen fraction pairs used in the calculations, $\tilde{r}$ is the median logarithmic ratio, $\mathrm{IQR}_{\log}$ is the interquartile range of the log ratio ($Q_{75} - Q_{25}$), $G = 10^{\tilde{r}}$ is the geometric mean ratio, and W_p is the two-sided Wilcoxon signed-rank test p-value. 84

6.2 Derived statistics for the pairwise logarithmic ratio of ice active frozen fraction between experiment number a ($\exp_a$) and experiment number b ($\exp_b$), defined as $\log_{10}(FF_a(T)) - \log_{10}(FF_b(T))$, computed at matched temperatures (temperature difference smaller than 0.7 K) for the Iceland experiments shown in Fig. 6.3. n is the number of matched ice active frozen fraction pairs used in the calculations, $\tilde{r}$ is the median logarithmic ratio, $\mathrm{IQR}_{\log}$ is the interquartile range of the log ratio ($Q_{75} - Q_{25}$), $G = 10^{\tilde{r}}$ is the geometric mean ratio, and W_p is the two-sided Wilcoxon signed-rank test p-value. 85